ANKARA UNIVERSITY

GRADUATE SCHOOL OF NATURAL AND APPLIED SCIENCES

PhD THESIS

Design and Optimization of the CLIC Positron Source from the Target to Damping Ring

CAFER BAYAR

DEPARTMENT OF PHYSICS

ANKARA

2018

ABSTRACT

Ph.D. Thesis

DESIGN AND OPTIMIZATION OF THE CLIC POSITRON SOURCE FROM THE TARGET TO DAMPING RING

Cafer BAYAR

Ankara University
Graduate School of Natural and Applied Sciences
Department of Physics

Supervisor: Prof. Dr. Abbas Kenan ÇİFTÇİ
Co-supervisor: Dr. Steffen DOEBERT

The CLIC Positron source has been designed to produce non-polarized positron beams using a hybrid target composed of a crystal followed by an amorphous target. After production, positrons are captured and accelerated to 200 MeV in the pre-injector linac and subsequently accelerated further up to 2.86 GeV in the injector linac. At this point they enter the pre-damping ring and afterwards the main damping ring to obtain the necessary beam quality for a linear collider. In this thesis, we have designed and optimized the beam transport and acceleration from the target to the pre-damping ring which has a limiting transverse and longitudinal acceptance. The goal of the thesis is to maximize the positron yield accepted by the pre-damping ring.

April 2018, 107 pages

Key Words: Positron source, linac, tracking, optimization, design, decelerating mode

ÖZET

Doktora Tezi

CLIC POZİTRON KAYNAĞININ HEDEFTEN SÖNÜMLEME HALKASINA TASARIMI VE OPTİMİZASYONU

Cafer BAYAR

Ankara Üniversitesi
Fen Bilimleri Enstitüsü
Fizik Anabilim Dalı

Danışman: Prof. Dr. Abbas Kenan ÇİFTÇİ
Eş Danışman: Dr. Steffen DOEBERT

CLIC Pozitron kaynağı, bir kristal hedefi ve ardından amorf bir hedefi içeren bir hibrid hedefi kullanarak polarize edilmemiş pozitron demetleri üretmek üzere tasarlanmıştır. Üretimden sonra, pozitronlar ön-enjektör linakta yakalanır, 200 MeV'e hızlandırılır ve daha sonra enjektör linakta pozitronlar 2,86 GeV'e kadar hızlandırılır. Bu noktada, pozitronlar ön sönümleme halkasına girerler ve daha sonra, doğrusal bir çarpıştırıcı için gerekli olan demet parametrelerini elde etmek için ana sönümleme halkasına girerler. Bu tezde, hedeften enine ve boyuna kabul sınırına sahip ön sönümleme halkasına kadar ki demet aktarımı ve hızlandırması tasarlandı ve optimize edildi. Tezin amacı, ön sönümleme halkası tarafından kabul edilen pozitronların verimini maksimum seviyeye çıkarmaktır.

Nisan 2018, 107 sayfa

Anahtar Kelimeler: Pozitron kaynağı, parçacık izleme, linak, optimizasyon, tasarım, yavaşlatma modu

TABLE OF CONTANTS

ACKNOWLEDGMENT

First and foremost, I would like to express my deepest gratitude to my supervisor at CERN Dr. Steffen DOEBERT for his excellent and continuous support during the entire thesis work since I arrived at CERN in 2014. I also would like to acknowledge him as the first reader of this thesis, and I am gratefully indebted to his for his very valuable comments on this thesis. His guidance helped me in all the time of research and writing of this thesis.

Besides my advisor, I would like to special thanks to Dr. Andrea LATINA who always encouraged and helped me during my research. I will always miss our scientific discussions with Andrea, his scientific excitement has always been a driving force for me during my research and my work. Also, I cannot ignore his help and contribution to me about PLACET particle tracking code.

I am grateful to Dr. Daniel SCHULTE for providing me the opportunity to be at CERN during my PhD thesis. He provided me the opportunity to attend 'International Accelerator Schools for Linear Colliders' in 2012 which is the first step that carry away me to CERN journey. This school was also meaningful for me since we met with him for the first time, we discussed about my thesis subject in this way and, the CLIC project adventure of myself started there thanks to him.

I would like to present my special thankfulness to my university supervisor Prof. Dr. Abbas Kenan ÇİFTÇİ, who created me an excellent opportunity at CERN by providing a collaboration between Ankara University and CLIC. I have been working with him since the years of my master studies. He has always supported and encouraged me during my master and PhD process. I took some courses from him in Ankara University about accelerator physics and this courses has been a milestone for me to take a decision to work on accelerator physics area.

I would like to appreciate my gratitude also to my colleagues and friends: Görkem TÜREMEN, Dr. Eduardo Marin LACOMA, Dr. Veli YILDIZ, Dr. Robert APSIMON, Dr. Mohsen Dayyani KELISANI, Dr. Shahin Sanaye HAJARI, Dr. Avni AKSOY, Özgür ETİŞKEN and Francesco Di LORENZO for their useful discussions and helps.

Görkem TÜREMEN deserves special thanks in this point. When I have arrived at CERN for the first time, Görkem did not refrain to support. We had useful brainstorming with him about beam physics. He has a big contribution in my progress. Especially, He helped to me about CST when I was in learning process.

Eduardo Marin LACOMA always helped to me about PLACET particle tracking code whenever I come across with a problem. I was not alone with the help of him whenever I present something about my work and he has always followed my developments during my research with his very useful feedback.

I cannot forget Veli YILDIZ’s helps about MATLAB. We always made useful discussion in coffee breaks at CERN and he always shared his acknowledge about beam dynamics calculations and simulation technics with me.

Mohsen Dayyani KELISANI and Shahin Sanaye HAJARI have been always helpful about PARMELA particle tracking code. I am grateful as they have developed my perspective in beam dynamics simulations and calculations.

Avni AKSOY gave a starting point and some useful advices to me in the Injector linac design. I made use of his experience about linac design.

Here, I would like to express our relation with Özgür ETİŞKEN. Our friendship date backs long times ago, to 2005, with Özgür ETİŞKEN. We shared same class in bachelor stage, started our journey in accelerator physics area together in master years in the same classes again and fortunately life directed us to the same university in PhD as well, we even shared same office at CERN when he is at CERN and interestingly with the effort for a different project for this time. I will never forget our brainstorming and discussion. He witnesses my all progress and development during my life. He always encouraged me and I always feel him supports and I believe that our relation will never end.

Francesco Di LORENZO has always been helpful and has supported me during I have been at CERN. I cannot forget relaxing chats with him. He always runs to my help whenever I run into in a trouble.

My sincere thanks also goes to Olivier DADOUN for providing the positron distribution at the exit of amorphous target for this study.

Finally, I would like to special thanks to my mother, my father and my sister, they have always patient and supported me during my staying at CERN. During my life, I have always felt their supports.

I am grateful to be always received endless support and guidance from this valuable people. I owe my sincere thanks to all of my colleagues, friends and my family members for their understanding, support and discussions during my research. In addition, I would like to special thanks The CLIC beam physics team for useful feedbacks and contributions.

This thesis is supported by CERN as a consequence of collaboration agreement between my home institute, Ankara University, and CLIC.

Cafer BAYAR

April, 2018

LIST OF FIGURES

LIST OF TABLES

LIST OF SYMBOLS

β	Betatron function
$\emptyset$	Phase
σ	Beam Size
σ_z	Bunch length
ε	Emittance
B_z	Longitudinal magnetic field
E_z	Longitudinal electric field
H_θ	Azimuthal magnetic field

Abbreviations

ACC	Accelerating Structure
AMD	Adiabatic Matching Device
ASTRA	A Space Charge Tracking Algorithm
ATLAS	A Toroidal LHC ApparatuS
BPM	Beam Position Monitor
CLIC	The Compact Linear Collider
CDR	Conceptual Design Report
CERN	the European Organization for Nuclear Research
CMS	The Compact Muon Solenoid
CST	Computer Simulation Technology
GeV	Giga-electron-volts
RF	Radio frequency
ILC	International Linear Collider
TW	Traveling wave
LAL	Le Laboratoire de l’Accélérateur Linéaire
LEP	Large Electron–Positron Collider
LHC	Large Hadron Collider
MeV	Mega-electron-volts
MAD	Methodical Accelerator Design
PARMELA	Phase And Radial Motion in Electron Linear Accelerators
PEDD	Peak Energy Deposition Density
PLACET	Program for Linear Accelerator Correction and Efficiency Tests
PS	Proton Synchrotron
SC	Synchrocyclotron
SLC	The Stanford Linear Collider
SPS	The Super Proton Synchrotron
PDR	Pre-Damping Ring
QD	Defocusing Quadrupole
QF	Focusing Quadrupole
TeV	Tera-electron-volts

1. INTRODUCTION

This thesis studies the positron production and acceleration within the positron source of CLIC. The positron transport from the production target to the entrance of the pre-damping ring has been optimized and redesigned with the goal to increase the positron yield.

In the chapter 1, a brief history of CERN, electron-positron colliders and possible particle physics research at CLIC has been described.

In the chapter 2, the Compact Linear Collider (CLIC) study is described and the updated baseline of the CLIC is presented for the different stages of CLIC. The CLIC injector complex updated by this thesis will be described as well as the CLIC positron source together with the positron production methods.

In chapter 3, the previous studies of the CLIC positron source being the starting point of this thesis are explained in detail.

In chapter 4, the general concepts of the new optimization are described for the CLIC positron source.

In chapter 5, the simulation results concerning the pre-injector linac for the CLIC positron source are presented.

In chapter 6, the optimization results of the injector linac are described.

In chapter 7, possible further improvements has been developed about the CLIC injector complex and the CLIC positron source.

Chapter 8 summarizes the results of this thesis.

1.1. Historical Development of CERN

Particle accelerators are used to understand deeply the fundamental structure of the universe. CERN, the European Organization for Nuclear Research, which is the world's largest and most complex particle physics laboratory, has a unique role in the world-wide high energy physics research. CERN consist of various particle accelerators and detectors. While the particle accelerators increase the energy for the charged particles like electrons, positrons and protons etc., the particle detectors allow to observe and analyze the collisions of charged particles at high energy. The CERN laboratory was founded in 1954 by 12 founding member states on the Swiss-France border near Geneva. At the present, CERN has 22 member states and 4 associate members. CERN’s first accelerator which is the 600 MeV Synchrocyclotron (SC) was built in 1957. The Proton Synchrotron (PS) accelerated protons for the first time in 1959. In the following, the construction of the Super Proton Synchrotron (SPS), which is the first of CERN’s underground rings with a circumference of seven kilometers, was approved by CERN’s member states in 1971 and the tunnel of SPS was completed in 1974. The first proton-antiproton collision at SPS were made by scientists in 1981 and in the following years W and Z bosons were discovered in the SPS at CERN. Carlo Rubbia and Simon Van der Meer received the Nobel Prize in physics after discovery of W and Z particles in 1983. The tunnel of the Large Electron-Positron (LEP) Collider being the 27 kilometers ring was completed in 1988 in order to produce and investigate in detail the Z bosons. The LEP Collider consisting of 5176 magnets and 128 accelerating cavities was the largest electron-positron collider and it was shut down at the end of the year 2000 to construct the Large Hadron Collider (LHC). The observation of the Higgs boson, has been achieved using the LHC. Peter Higgs and François Englert were awarded with the Nobel Prize in Physics for their work and prediction which was confirmed by ATLAS and CMS experiments at CERN in 2012 [1, 2, 3].

1.2. A General Outlook of Electron-Positron Colliders

In the year of 2000, an energy of 209 GeV which is the highest energy at electron-positron colliders so far was achieved in LEP at CERN. From the beginning it was known that the beam energy was limited in circular electron-positron colliders due to the synchrotron radiation loss. Two options were explored for a TeV lepton collider to overcome the synchrotron radiation loss. The first is a muon collider and the second is to build a linear electron-positron collider. In this regard, after the construction process which was five years, the Stanford Linear Collider (SLC) was completed in 1987. The SLC was the first liner collider in the world. The success of the SLC has triggered designs of new generation electron-positron colliders with a collision energy of 500 GeV and next stage Tera-scale [4]. As a result, two projects International Linear Collider (ILC) and Compact Linear Collider (CLIC) have been developed [5, 6]. The CLIC studies are still ongoing at CERN.

1.3. The Particle Physics Research at CLIC

The advantage of an electron positron colliders is to provide more clean collisions compared to a proton-proton collision, because electron and positron are fundamental particles which are not composed out of other particles like protons consisting of quarks. With the observation of the Higgs boson in LHC, the further Higgs and top-quark studies have become an important goal. Electron positron colliders would be very suitable for studying the Higgs physics in detail. In this regards, the first stage of CLIC has been updated and proposed to be at 380 GeV. CLIC would make possible high precision measurements of the Higgs and top-quark properties such as the top-Yukawa coupling, the Higgs self-coupling and rare Higgs branching ratios. Possible Higgs boson measurements through the Higgsstrahlung and WW-fusion production processes are described in [7, 8]. The expected numbers of $Z\mathrm{H}, \mathrm{H}\upsilon_e\overline{\upsilon}_e$ and $\mathrm{H}e^+e^-$ events for the three main CLIC stages are summarized in table1.1. Feynman diagrams about Higgs production at CLIC are shown in Fig.1.1 and Fig.1.2.

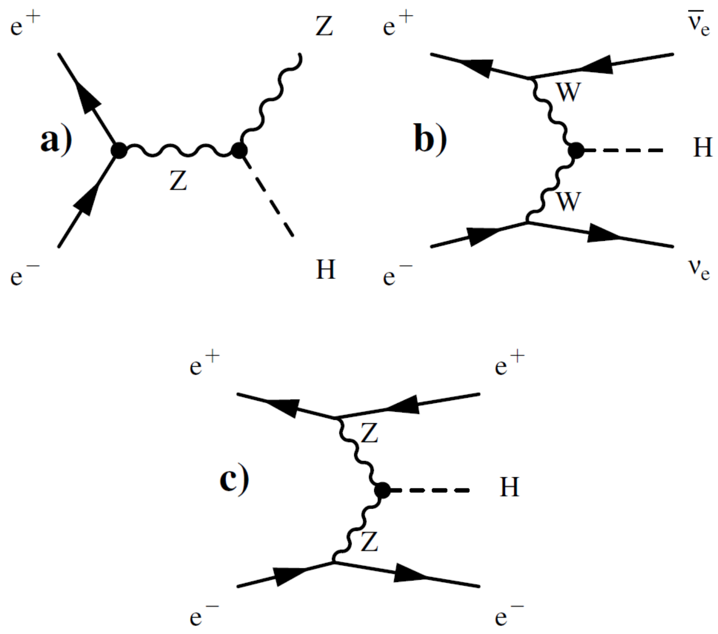

Figure 1.1: Leading-order Feynman diagrams of the highest cross section Higgs production processes at CLIC [8]
a. Higgsstrahlung, b. WW-fusion, c. ZZ-fusion

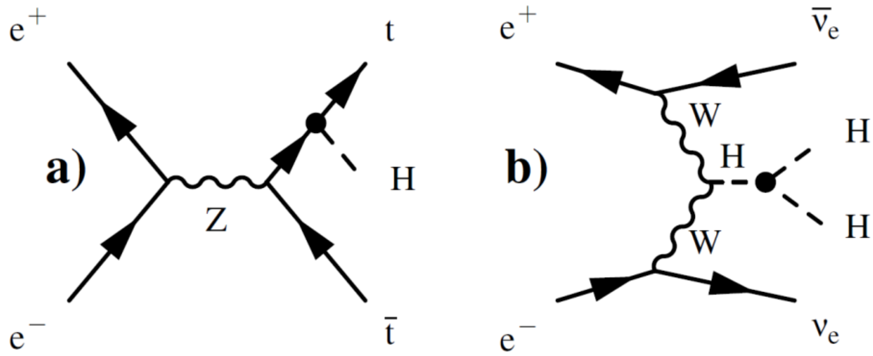

Figure 1.2: Feynman diagrams of the leading-order processes at CLIC [8]
Involving (a) the top Yukawa coupling gHtt , and (b) the Higgs boson trilinear self-coupling λ.

Table 1.1 Leading order, unpolarised cross sections for Higgsstrahlung, WW-fusion, and ZZ-fusion processes for $m_{\mathrm{H}} = 126$ GeV at the three center-of-mass energy [8].

$\sqrt{s} =$	**350 GeV**	**1.4 TeV**	**3 TeV**
$\int \frac{d\mathcal{L}}{ds'} ds'$	500 fb^{-1}	1.5 ab^{-1}	2 ab^{-1}
$\sigma(e^+e^- \rightarrow \mathrm{ZH})$	133 fb	8 fb	2 fb
$\sigma(e^+e^- \rightarrow \mathrm{H}\upsilon_e\overline{\upsilon}_e)$	34 fb	276 fb	477 fb
$\sigma(e^+e^- \rightarrow \mathrm{H}e^+e^-)$	7 fb	28 fb	48 fb
No. ZH events	68,000	20,000	11,000
No. $\mathrm{H}\upsilon_e\overline{\upsilon}_e$ events	17,000	370,000	830,000
No. $\mathrm{H}e^+e^-$ events	3700	37,000	84,000

$\sqrt{s'}$ is the effective center-of-mass energy of the e^+e^- collision. The presented cross section include the effects of initial state radiation (ISR) but exclude the effects of the beamstrahlung. Also given are numbers of expected events, including the effects of ISR and the CLIC beamstrahlung spectrum. The presented cross sections and event numbers do not include possible enhancements from polarized beams [8].

2. THE COMPACT LINEAR COLLIDER (CLIC)

The Compact Linear Collider (CLIC) is a study of a world-wide collaboration with the aim to achieve a high-energy and high-luminosity electron-positron collider. CLIC is based on a novel two-beam technology consisting of a drive beam and a main beam. While the drive beam is used as the power source, the main beam provides acceleration for electrons and positrons. The CLIC Conceptual Design Report (CDR) including two beam accelerating concepts for 3 TeV and 500 GeV options has been published in 2012 [5], just before the discovery of the Higgs Boson at the Large Hadron Collider (LHC) [1, 2]. In 2016, the first stage of CLIC has been proposed and updated at 380 GeV considering the Higgs and top quark physics studies [7, 8]. CLIC includes three implementation stages with center-of-mass energy of 380 GeV, 1.5 TeV and 3 TeV as indicated in Fig.2.1 [7].

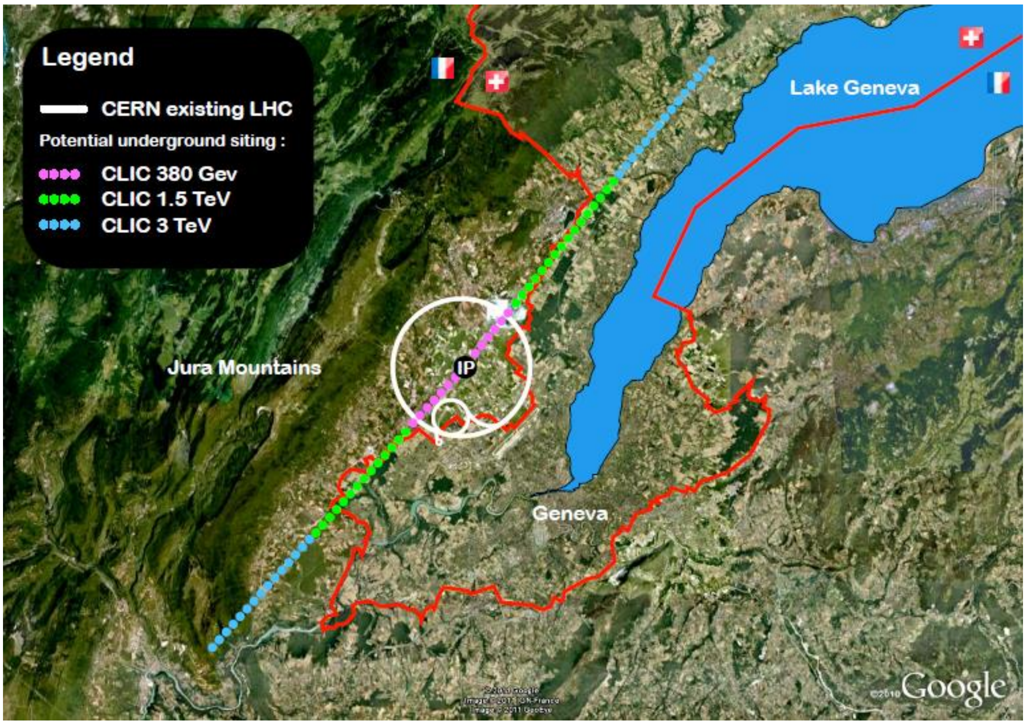

Figure 2.1 CLIC footprints near CERN, showing three stages with different energy [7].

2.1. The CLIC Drive Beam and Main Beam Complexes

CLIC is based on the two beam acceleration scheme, drive beam and main beam. The CLIC drive beam complex consists of the drive beam accelerators, drive beam recombination complex, beam transport and finally, the CLIC main beam complex includes an injector complex, ring to main linac transport (RTML), main linacs, beam delivery system, detectors and post-collision line. In the first stage of CLIC has a luminosity of L = $1.5 \times 10^{34} cm^{-2} s^{-1}$ at a center-of-mass energy of 380 GeV and the gradient of the accelerating structures is 72 MV/m. Parameters for the CLIC energy stages are summarized in table 2.1. It can be seen in Fig.2.2 and Fig.2.3 that for the full energy of 3 TeV, two drive beam complexes are needed, in the first and second stages a single drive beam generation complex is sufficient to power the main beam [7].

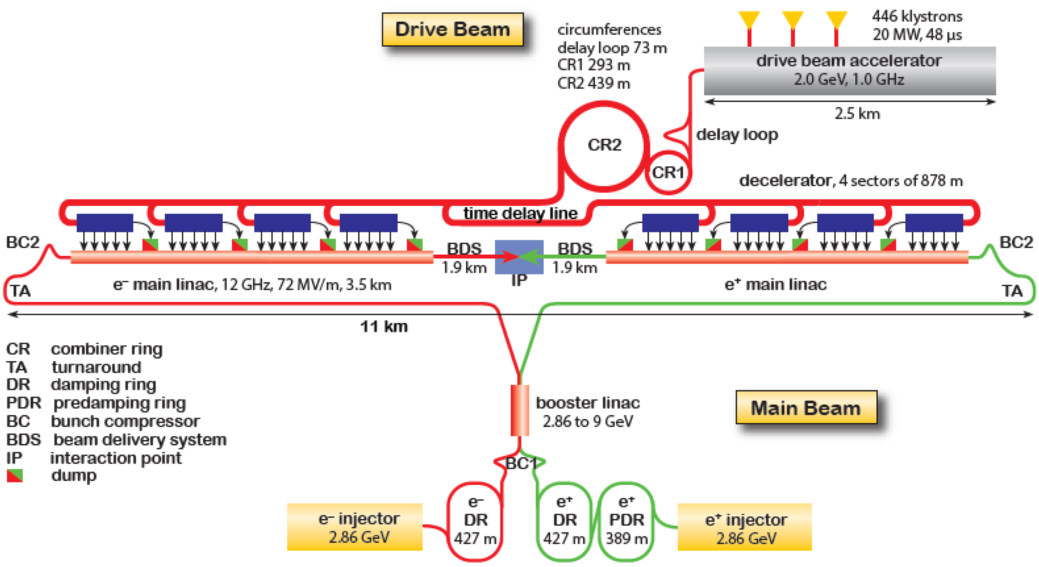

Figure 2.2 Overview of the CLIC layout at $\sqrt{s} = 380\ GeV$. Only one drive beam complex is needed for the first (and second) stage of CLIC [7].

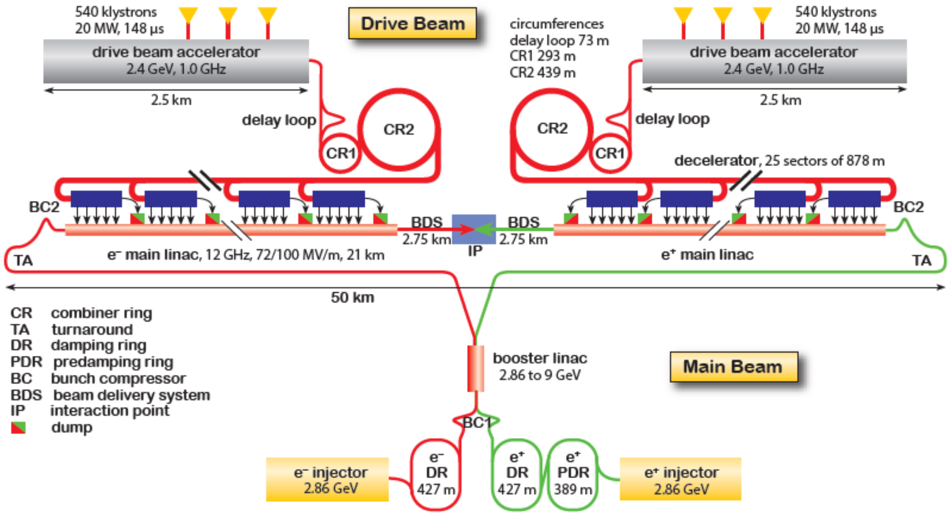

Figure 2.3: Overview of the CLIC layout at $\sqrt{s} = 3\ TeV$ [7].

Table 2.1 Parameters for the CLIC stages. [7].

Parameter	**Unit**	**Stage 1**	**Stage 2**	**Stage 3**
Center-of-mass-energy	GeV	380	1500	3000
Repetition frequency	Hz	50	50	50
Number of bunches per train		352	312	312
Bunch separation	ns	0.5	0.5	0.5
Pulse length	ns	244	244	244
Accelerating gradient	MV/m	72	72/100	72/100
Total luminosity	$10^{34}cm^{-2}s^{-1}$	1.5	3.7	5.9
Luminosity above 99% of $\sqrt{s}$	$10^{34}cm^{-2}s^{-1}$	0.9	1.4	2
Main tunnel length	km	11.4	29.0	50.1
Number of particles per bunch	10^9	5.2	3.7	3.7
Bunch length	µm	70	44	44
IP beam size	nm	149/2.9	$\sim 60/1.5$	$\sim 40/1$
Normalized emittance (end of linac)	nm	920/20	660/20	660/20
Normalized emittance (at IP)	nm	950/30	-	-
Estimated power consumption	MW	252	364	589

The power consumptions for the 1.5 and 3 TeV stages are from the CDR; depending on the details of the upgrade they can change

2.2. The CLIC injector Complex

The CLIC injector complex consists of a polarized electron source with an e^- pre-injector linac, a 5 GeV driver electron linac, non-polarized positron source, damping ring complex and a 9 GeV booster linac as seen in Fig.2.4.

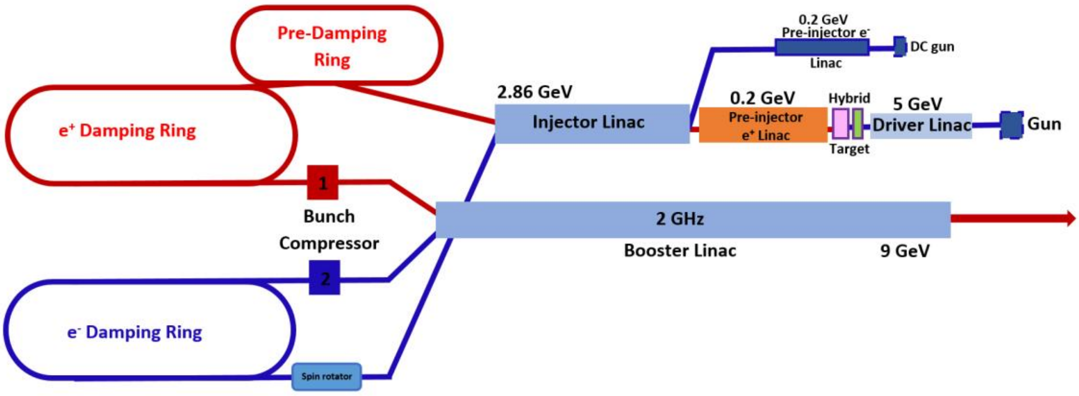

Figure 2.4 Schematic layout of the updated CLIC injector complex

In this thesis, the new studies of the CLIC positron source show that the CLIC injector complex can be improved for the first stage of the CLIC at 380 GeV. In the CLIC CDR, the injector complex was assumed with two target stations in parallel consisting of two pre-injector linacs and two hybrid targets due to the higher beam current at this stage. The new simulation result show that a single target station can be used for the first stage of CLIC at 380 GeV [9]. In the new baseline of the injector complex, a single target station has been considered and the bunch compressor between the pre-injector and the injector linac has been removed. The optimization of the pre-injector linac has been done and a factor 2.5 factor increase of the positron yield within the acceptance window of the pre-damping ring has been obtained. This increase in positron yield allows to lower the primary beam current and therefore it was possible to operate with a single target station [9].

In addition the following changes have been proposed for the new baseline of the 380 GeV injector complex: The delay loop ring is removed for electrons and positrons after the damping rings because a 2 GHz bunch spacing was chosen in the entire injector complex. Furthermore, a pre-damping ring is not needed for the electron beam because it is believed that the emittance of the electron beam after the injector linac will be small enough (CLIC community decision).

2.3. The CLIC Positron Source

There are three main methods to produce positrons. The first method is to impinge electrons on an amorphous target (conventional method) to produce non-polarized positron beams via photons from bremsstrahlung. The second method is to use a hybrid target consisting of a crystal target followed by an amorphous target (channeling process). Here the crystal target is used to enhance the photon yield due to the channeling process. The gap between the targets allows to remove charged particles which would otherwise increase the energy deposition on the amorphous target. The CLIC is based on the second method to produce non-polarized positron beams. The third method is to send polarized gamma rays on an amorphous target which would then produce polarized positrons.

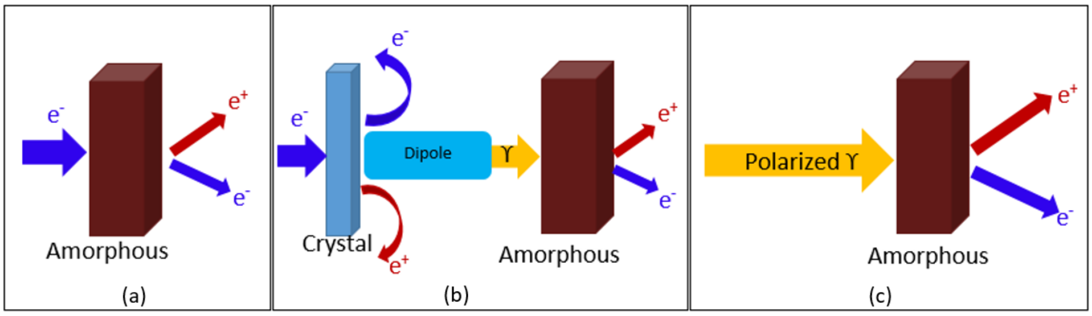

Figure 2.5 Sketch of positron production methods
(a) Conventional, (b) Channeling Process and (c) Polarized Gamma Rays

As seen on the left plot in Fig.2.5 (a), the electron beam creates electron-positron pairs after impinging onto an amorphous target in the conventional method. For the channeling process (see the middle plot in Fig.2.5 (b)), the electron beam is used to generate the photons and then they are used to generate un-polarized positrons at the amorphous target. The advantages of the hybrid target containing a crystal target and an amorphous target, has been shown in the CLIC CDR and the hybrid target has been chosen to generate un-polarized positrons for CLIC positron source. At SLC, it was shown experimentally that the Peak Energy Deposition Density (PEDD) should not exceed 35 J/g [10]. The CLIC positron source respects this limit and the PEDD is around ~30 J/g in the CLIC hybrid target [5]. The polarized gamma rays are used to create the polarized positrons (see the right plot in Fig.2.5 (c)). The option of the polarized positron generation has been investigated for CLIC but is not part of the baseline design [5].

The positron source for CLIC needs to deliver intense high quality positron beams for the linear collider. Depending on the construction stage of the collider the source needs to deliver trains of up to 352 bunches with a bunch repetition rate of 2 GHz and up to 5.6×10^9 positrons per bunch to the main linac of the collider at 50 Hz repetition rate [5]. A conventional positron source uses only a single amorphous target. The CLIC source takes advantage of a novel hybrid target design consisting of a thin crystal target to enhance photon production via channelling and an amorphous target to convert the photons into positrons. As seen in Fig.2.6, a 5 GeV electron beam impinges onto a crystal target and electron-positron pair production is created via the channeling process. In between targets, a magnet is used to sweep out charged particles to reduce the peak power deposition on the production target [11]. The CLIC positron target was optimized for a 5 GeV electron driver obtaining a yield of 8 e+/e- [12]. The positron yield is defined as the number of positrons produced per electron impinging onto the target.

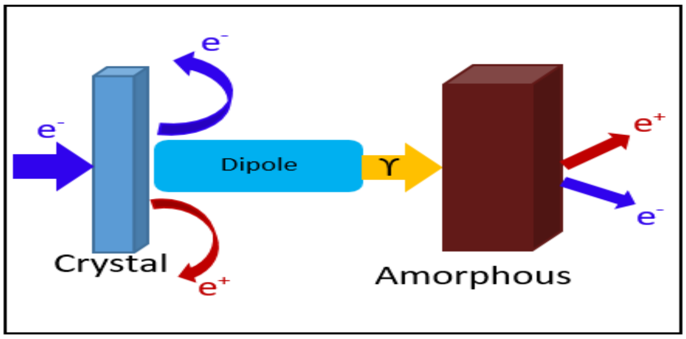

Figure 2.6 the CLIC positron source based on a hybrid target

A conceptual description of the CLIC positron source can be found in the CLIC CDR based on simulations in collaboration with LAL [5, 11, 12, 13, 14 and 15]. The hybrid target has been optimized for the maximum positron yield. The parameters of the hybrid target are given for CLIC positron source in the table 2.2.

Table 2.2 The CLIC Hybrid target parameters [5]

Parameter	Value
Incoming electron beam energy [GeV]	5
Crystal target thickness [mm]	1.4
Distance between crystal and amorphous target [m]	2
Amorphous target thickness [mm]	10

After the amorphous target, the conical magnetic field of the AMD focuses the positrons in order to efficiently capture in the downstream accelerating structures. The longitudinal magnetic field of the AMD changes from 6 T to 0.5 T in 20 cm. The CLIC positron source consists of a hybrid target, an Adiabatic Matching Device (AMD), the pre-injector linac and the injector linac as seen in Fig.2.7.

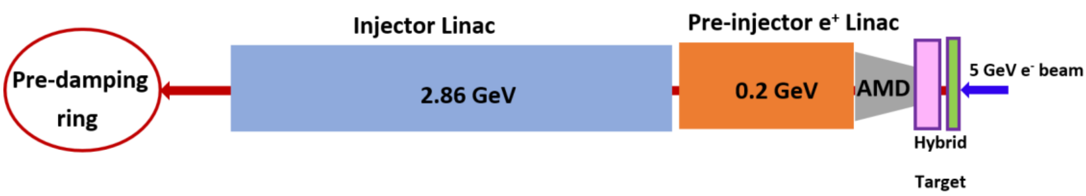

Figure 2.7 Schematic layout of the CLIC positron source

In the next chapter, the results of the previous studies will be presented by the system description.

3. STARTING POINT OF THE PREVIOUS RESULTS

The CLIC positron source was optimized for the highest positron yield at the exit of the target in the previous studies and the conceptual design of the CLIC positron source was described in the CDR. The CLIC positron source included a hybrid target, a 200 MeV capture linac, a bunch compressor and a 2.86 GeV injector linac in the CDR. In this chapter, we will mention about the previous studies which is the starting point of this thesis.

3.1. The Previous Studies about the CLIC Pre-Injector Linac

The CLIC pre-injector linac includes the Adiabatic Matching Device (AMD) and accelerating sections. After the target the positrons are accelerated up to 200 MeV. With a longitudinal magnetic field changing from 6 T down to 0.5 T, the length of the adiabatic matching device (AMD), whose parameters are summarized in table 3.1, is 20 cm and the following accelerating structures are embedded inside a constant solenoidal magnetic field of 0.5 T. A shorter AMD of 20 cm helps to capture more positrons compared to long one (50 cm were studied in CLIC-Note-808) [12]. A constant radius of 20 mm was used in the simulation of the AMD. At the exit of the AMD the positron yield is around 2.1 e^+/e^- [5].

Table 3.1 AMD parameters

Parameter	Value
Length [cm]	20
Initial longitudinal magnetic field [T]	6
Final longitudinal magnetic field [T]	0.5
Vacuum chamber radius [mm]	20

The accelerating structure of the CLIC pre-injector linac was chosen with a length of 4.36 m Travelling wave (TW), a constant gradient of 15 MV/m and $2\pi/3$ mode at 2

GHz as given in table 3.2. In the design of the pre-injector linac, two operational modes, accelerating and decelerating were investigated and the advantage of the decelerating mode has been shown in CLIC CDR. In this thesis, accelerating structures with a length of 1.5 m are chosen, the pre-injector linac has been redesigned and simulated. It turned out that longer structures are unrealistic due to the power requirements taking into account the heavy beam loading.

Table 3.2 Parameters of the accelerating structures in the pre-injector linac

Parameter	Value
Length [m]	4.36
Maximum accelerating gradient [MV/m]	15
Maximum decelerating gradient [MV/m]	6
Phase advance per cell	2π/3
Cell length [cm]	4.99

The decelerating mode was proposed firstly in 1979 by B. Aune and H. R. Miller [16]. The advantages of the deceleration have been tested experimentally and it has been shown that it provides a better positron yield. While in the accelerator mode the positron beam with a long tail is obtained, it is shown that the decelerating mode gives a compact positron distribution in the phase space with a higher yield as can be seen in Fig.3.1 and Fig.3.2 [15].

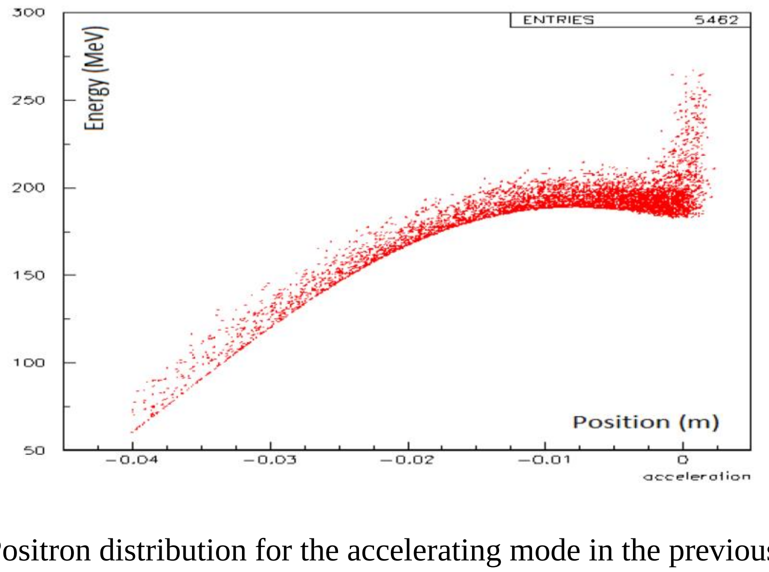

Figure 3.1 Positron distribution for the accelerating mode in the previous studies [5]

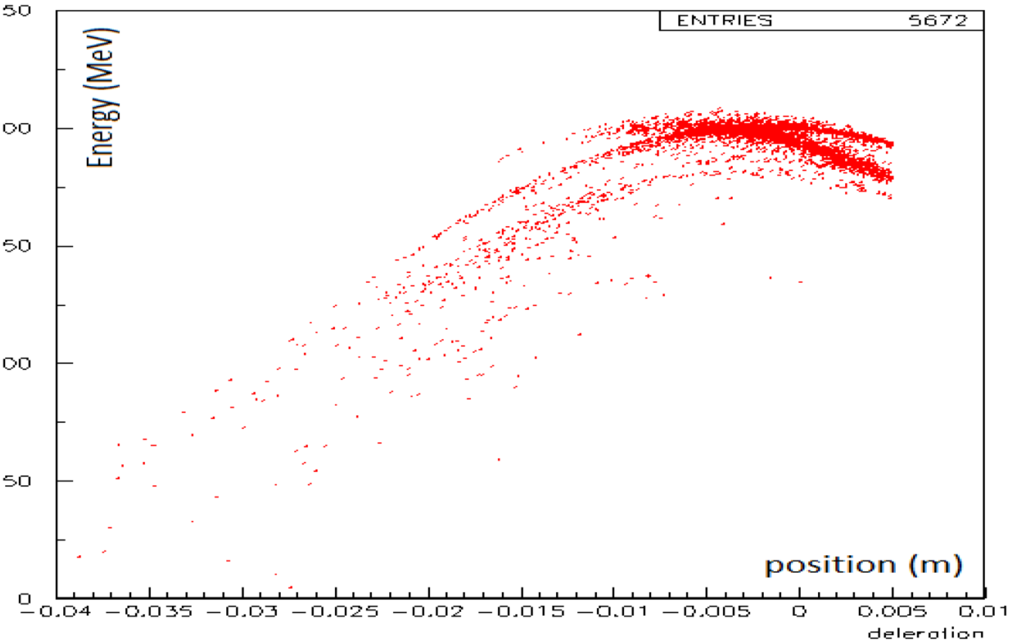

Figure 3.2 Positron distribution for the decelerating mode in the previous studies [5]

In the accelerating mode, a phase close to the maximum acceleration on crest was chosen for the accelerating structures along the pre-injector linac. The positrons were accelerated up to 200 MeV and tracked using ASTRA tracking program [17]. In the decelerating mode, a gradient of 6 MV/m was chosen for the first accelerating structure. As a result of this studies, it was shown that the decelerating mode gives a slightly higher yield with a compact positron distribution in the phase space. Although the total yield is around 0.9 e^+/e^- in the accelerating mode, it is 0.95 e^+/e^- in the decelerating mode. In the previous studies, the simulation results showed that when a higher gradient was used for the deceleration, it results in a higher energy dispersion at the end of the structure.

3.1. The Previous Studies about the CLIC Injector Linac

The CLIC injector linac accelerates the positrons from 200 MeV up to 2.86 GeV to inject within the acceptance window of the pre-damping ring. The acceptance window of the CLIC Pre-Damping Ring (PDR) is described for momentum deviation $\delta p/p$ varying from -1.2% to $+1.2\%$ for the 2 GHz bunch spacing as seen in Fig.3.3.

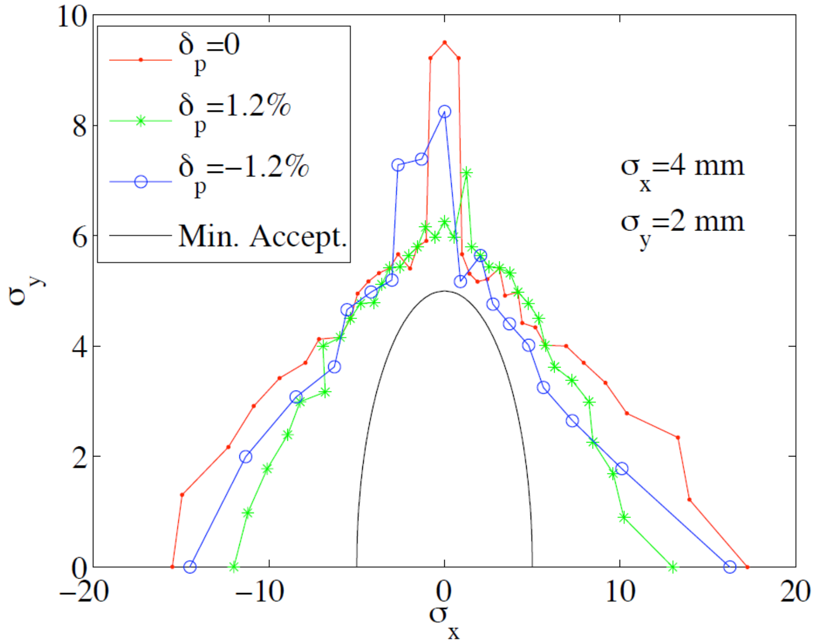

Figure 3.3 Dynamic Aperture of the Pre-Damping Ring (PDR), for particles with momentum deviations of zero (red), +1:2% (green) and -1:2% (blue), as compared to the physical ring acceptance (black) [5]

In the previous studies, a bunch compressor was used at the exit of the pre-injector linac to rotate the positrons in the phase space as seen in Fig.3.4. In our studies, we have removed this bunch compressor in the CLIC injector complex [9]. Because, the simulation results show that the rms energy spread around 4 % at the exit of the pre-injector linac, it is already very small due to the optimization of the pre-injector linac. The detail information will be presented in the next chapters.

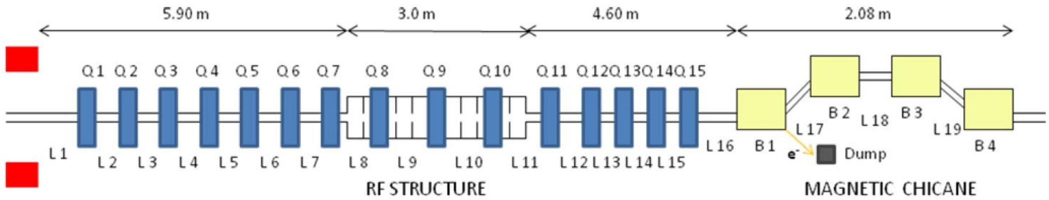

Figure 3.4 The layout of the bunch compressor [14]

Table 3.3 Parameters of the accelerating structures in the injector linac [14]

Parameter	**Parameter Unit Value**
Length [m]	3.9
Aperture radius [mm]	30
Electric Field [MV/m]	14.6
Frequency [GHz]	1.9992
Energy gain [MeV]	56.95

In the design of the CLIC injector linac, the triplet lattice was chosen and the injector linac consisted of three sections [14].

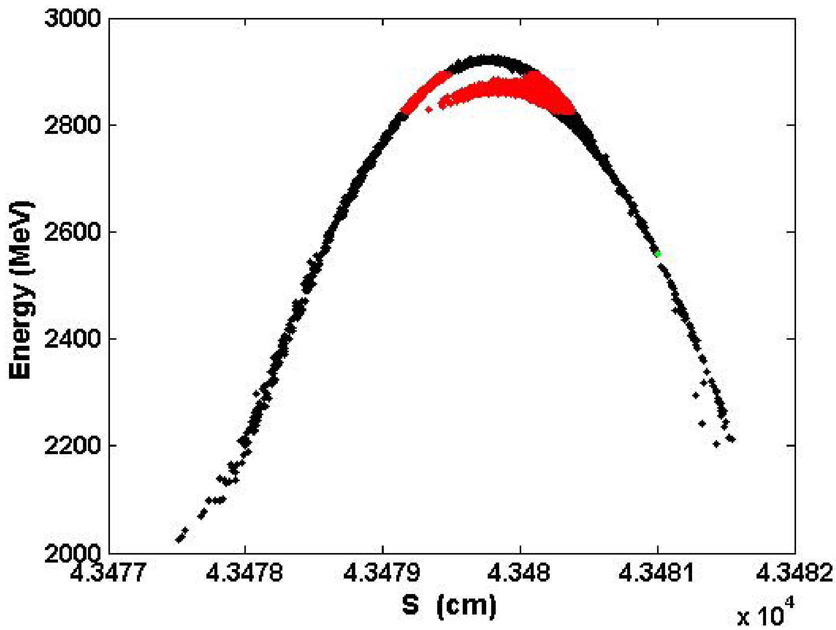

Figure 3.5 Longitudinal phase space of the beam at the end of the Injector Linac [14]. Points in red line inside the energy acceptance of the PDR.

The theoretical acceptance of the CLIC pre-damping ring was found to be up to 1.2 %. Figure 3.5 shows the positron distribution in the phase space and the positron yield is around 0.45 e^+/e^- in the red region. The total yield is 0.70 e^+/e^- at the exit of the injector linac. The positron yield has been estimated to 0.39 e^+/e^- for 1 % energy acceptance of the pre-damping ring in CDR taking a safety margin on possible damping ring acceptance. The positron yield for different energy acceptances is shown in table 3.4.

Table 3.4 Parameters of the accelerating structures in the injector linac [5, 14]

Energy Acceptance %	**(e+/e-)**
1.0	0.390
1.2	0.453
2	0.561
3	0.619

The detailed studies shows that the CLIC positron source must be optimized for the positrons at the entrance of the pre-damping ring with respect to the acceptance window. A detailed technical design of the beam line from the target to the end of the injector linac was needed. Therefore tracking simulations had to be done to optimize the working point of the capture linac and the beam optics of the whole beam line in order to verify the yield of the positron production for CLIC. Some work has been done in collaboration with LAL Orsay as mentioned in this chapter but in this thesis a complete integrated study using a realistic accelerating structure has been done to verify the concept. In the following chapters, the studies carried out within the scope of this thesis will be described in detail.

4. NEW OPTIMISATION OF THE CLIC POSITRON SOURCE

In the Conceptual Design Report (CDR), a prove of principle approach was used to describe the design of the positron production chain for CLIC, estimating a positron yield of 0.39 e^+/e^- from the target to the entrance of the pre-damping ring [14, 15]. The positron yield is defined as the number of positrons within the acceptance of the pre-damping per electron impinging onto the target. A study was launched to substantially improve the positron yield in this area to increase the margin of the positron target in terms of peak energy deposition and to reduce the cost and energy consumption of the required electron driver linac. The CLIC positron source includes a hybrid target, an Adiabatic Matching Device (AMD), the pre-injector linac and the injector linac.

The aim of the study described in the following, is to preserve as many as possible of these precious positrons during acceleration and transport them up to the pre-damping ring. Intuitively, the positron capture linac should increase the positron energy as fast as possible to reduce the divergence and the energy spread. However, it has been shown in the past that initial deceleration can lead to a more efficient capturing [16].

The CLIC positron source divides the acceleration into a pre-injector linac, which accelerates the positrons up to 200 MeV and a final injector linac which boosts the energy up to 2.86 GeV, which is the injection energy of the damping rings. This separation comes from the fact that the injector linac is used both for electrons and positrons in the CLIC injector complex. The positrons are then injected into a pre-damping ring and a damping ring to reduce their emittance and finally accelerated to 9 GeV for transport into the main linac. The pre-damping ring has a limited transverse and longitudinal acceptance. Most critical for the positron beam is the energy acceptance window of ±1.2 %. The CLIC injector complex is shown schematically in Fig. 4.1.

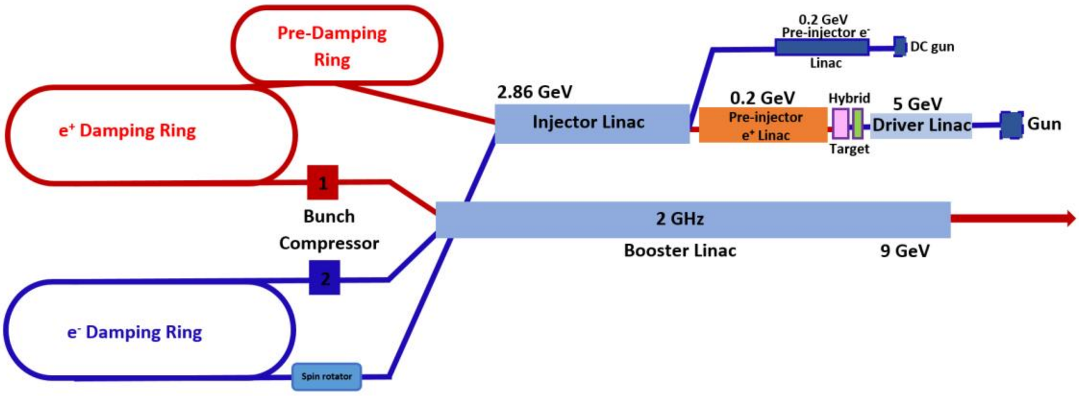

Figure 4.1 Schematic layout of the CLIC injector complex

The design and optimization of the pre-injector linac and the injector linac carried out with the objective to maximize the positron yield into the pre-damping ring acceptance will be described in the following chapters.

5. OPTIMIZATION OF THE CLIC PRE-INJECTOR LINAC

In the CLIC positron source, the optimization of the pre-injector linac has a very important role to increase the positron yield within the acceptance window of the pre-damping ring. Two operation modes has been considered in the pre-injector linac to maximize the positron yield; the accelerating mode and the decelerating mode.

The CLIC pre-injector linac has been optimized from the exit of the target up to an energy of the captured positrons of roughly 200 MeV. Starting point was the simulated positron distribution at the exit of the target from the previous study [13]. After the target, the Adiabatic Matching Device (AMD) reduces the beam divergence and concentrates a maximum of particles into the aperture of the first structure. The 6 T maximum field is believed to be feasible for such an aperture in a pulsed normal-conducting device. The length of the beam pulse is 176 ns. In the design of the pre-injector linac, an aperture of 20 mm radius has been chosen for the design of the 2 GHz accelerating structure as a compromise between obtainable gradient and power consumption. The model was based on a 1.5 m long $2\pi/3$ traveling wave structure with a gradient of up to 15 MV/m. For the simulations it is presumed that the whole pre-injector linac is embedded into a solenoidal magnetic field of 0.5 T.

Considering this chapter, both operation modes, accelerating and decelerating in the first rf structure, have been studied. In addition, the optimization of the decelerating mode has been also investigated in the pre-injector linac. The tracking simulation of the pre-injector linac has been done by using PARMELA tracking code [18, 19]. In this section, we would like to explain the design and optimization of the pre-injector linac.

5.1. The Definition of the Parameters for the Initial Positron Beam

The capture section of CLIC positron source consist of the Adiabatic Matching Device (AMD) and the pre-injector linac. After production on the target with 5 GeV electrons, positrons have naturally large energy spread and emittance. The resulting positron distribution after the target is shown in Fig.5.1 and Fig.5.2. The average energy of the positrons is about 50 MeV at this stage. The initial design of the pre-injector linac, documented in the CDR, focused on capturing the positrons with energies up to roughly 100 MeV. The other natural cut on this enormous distribution was the transverse acceptance of the AMD and the accelerating structures given mainly by their physical aperture.

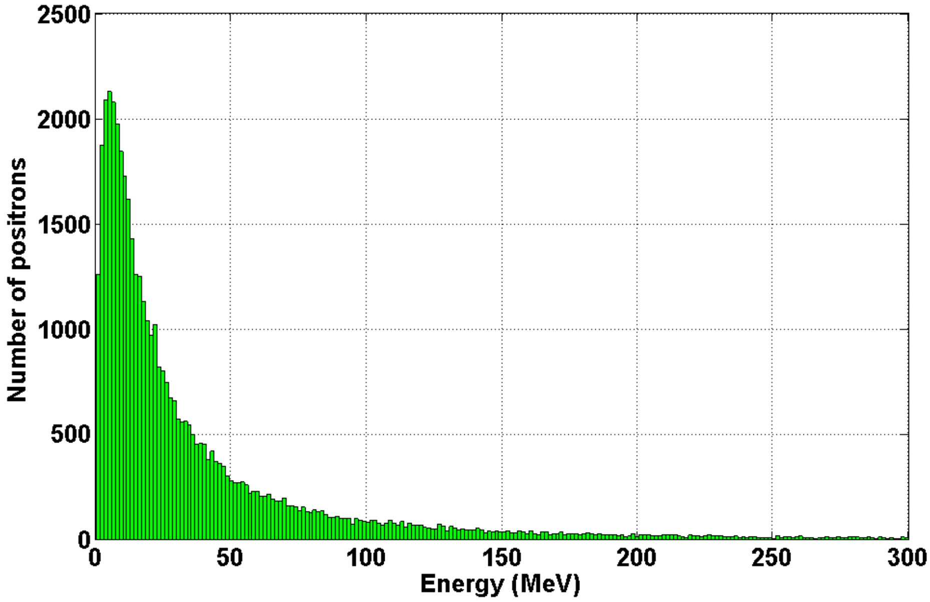

Figure 5.1 Energy distribution for positrons after the target
This figure shows the energy spectrum of positrons applying a cut at 300 MeV.

The rms bunch length, σ_z , should be around 0.3 mm for the realistic positron distribution [14]. The corresponding rms phase spread, ϕ_{rms} can be calculated from equation (5.1).

$$\phi_{rms} = \frac{2\pi f_0 \, \sigma_z}{c} \tag{5.1}$$

Where, c is the velocity of the light in a vacuum and the rf frequency of the linac, f_0, is 2 GHz. As a result of the calculation, it is obtained that the rms phase spread should be around 1.44 degrees. A random Gaussian distribution with a sigma of 1.44 degrees was generated and used with the initial distribution of positrons. The longitudinal position of positron distribution at the exit of the target can be seen in Fig.5.3. The detail information about the definition of beam parameters in PARMALE can be found in Appendix 1.

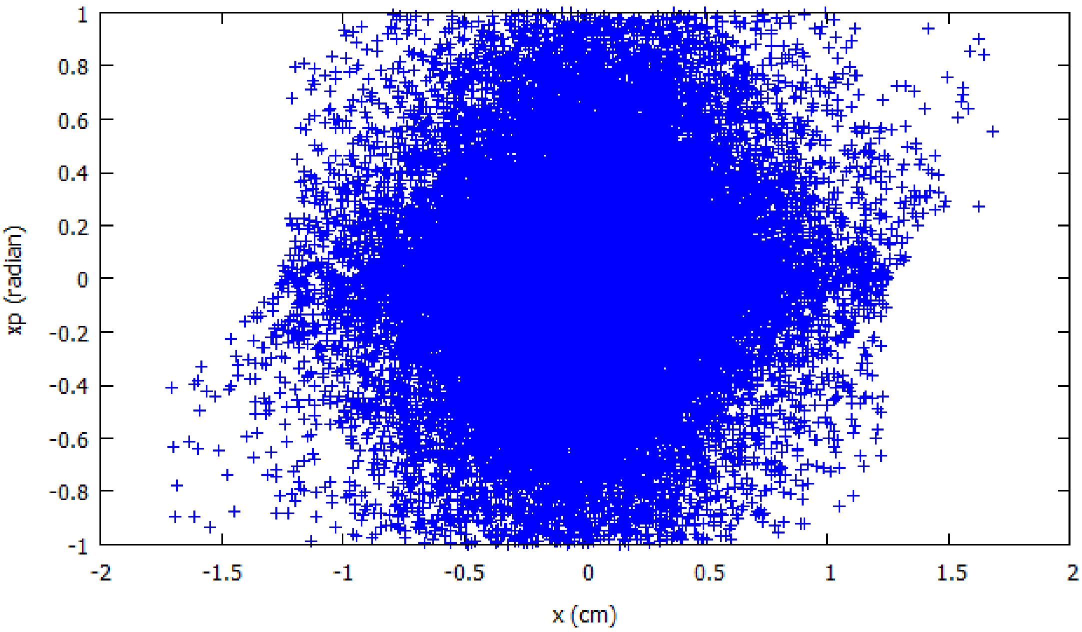

Figure 5.2 Transverse phase space distribution for positrons after the target

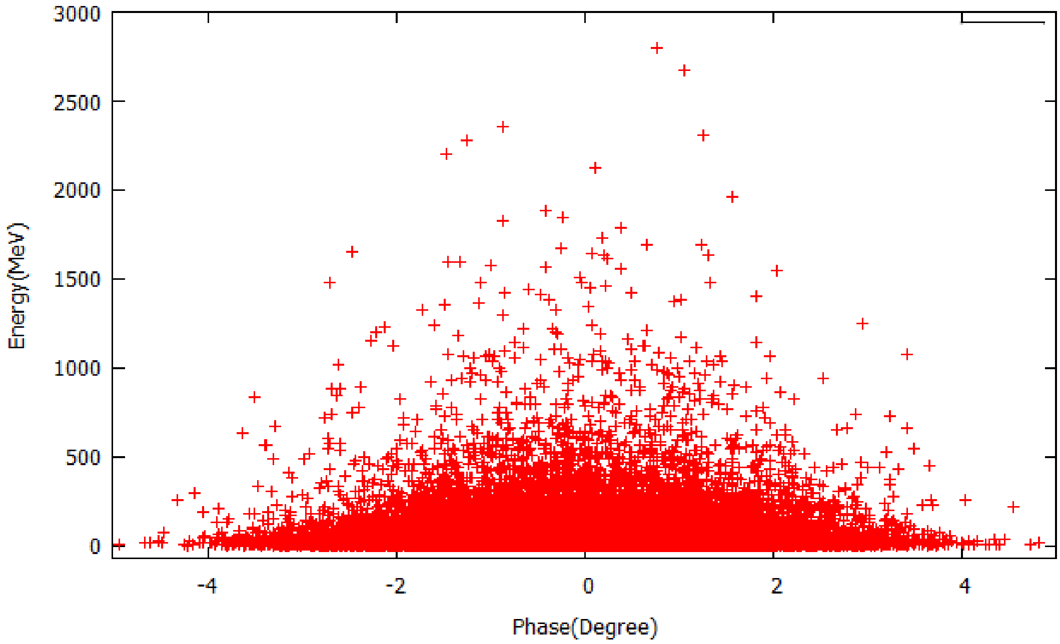

Figure 5.3 Energy and phase distribution for positrons after the target

5.2. Design and Simulation of the Adiabatic Matching Device (AMD)

The simulations of the pre-injector linac launches after the target and the adiabatic matching device (AMD) is the first element of the capture section for the CLIC positron source. The longitudinal magnetic field of AMD is decreasing exponentially from 6 T to 0.5 T on a distance of 20 cm. The longitudinal magnetic field of an ideal AMD is determined by equation (5.2).

$$B_z(z) = \frac{B_0}{1+\alpha z} \tag{5.2}$$

The maximum value of magnetic field B_0 is 6 T at the entrance, z is the longitudinal coordinate changing along the AMD and $\alpha = 55\, m^{-1}$ which is a coefficient specifying the slope of the magnetic field.

$$\alpha = \frac{\varepsilon B_0}{P_0} \tag{5.3}$$

In equation (5.3), P_0 is a central momentum value for the emitted positron and ε is smallness parameter [20].

$$\varepsilon = \left(\frac{P}{eB^2}\right)\frac{dB}{dz} \ll 1 \tag{5.4}$$

Here, P is the scalar momentum and the variation ratio of the magnetic field is determined by dB/dz in equation (5.4).

In the design of the AMD, the longitudinal magnetic field is created by using discrete coils in PARMELA. The detail information about the definition of parameters in PARMELA can be found in Appendix 2.

The longitudinal magnetic field can be seen for ideal AMD and modelled AMD in Fig.5.4. The magnetic field of the ideal AMD is generated by using equation (5.2). The longitudinal magnetic field reconstructed in PARMELA out of single coil elements is compatible with ideal AMD field.

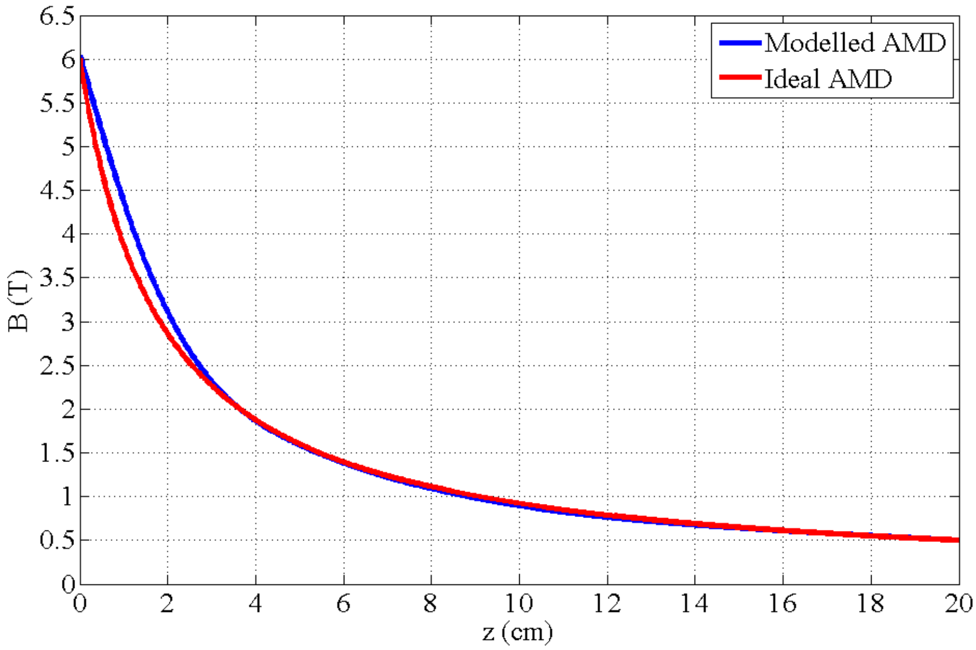

Figure 5.4 Longitudinal magnetic field of (red) ideal AMD and (blue) modelled AMD

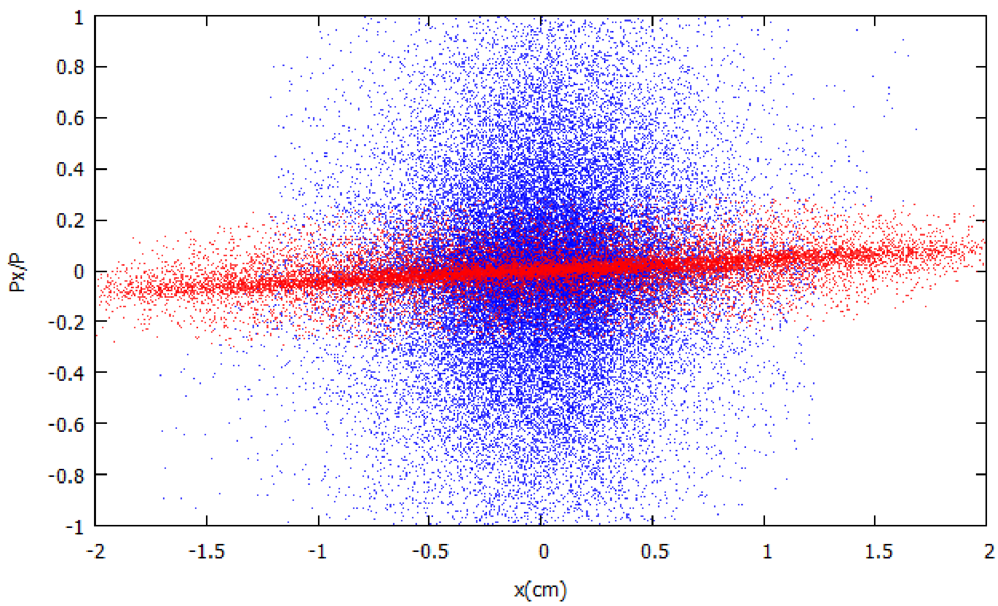

Figure 5.5 Transverse phase space of the positrons after target (blue) and AMD (red)

As seen from Fig.5.5, the AMD rotates and compresses the positron beam in the transverse phase space. The positron yield should be around 2.1 e^+/e^- at AMD exit [5], the new simulations indicate a slightly higher yield 2.8 e^+/e^- [21].

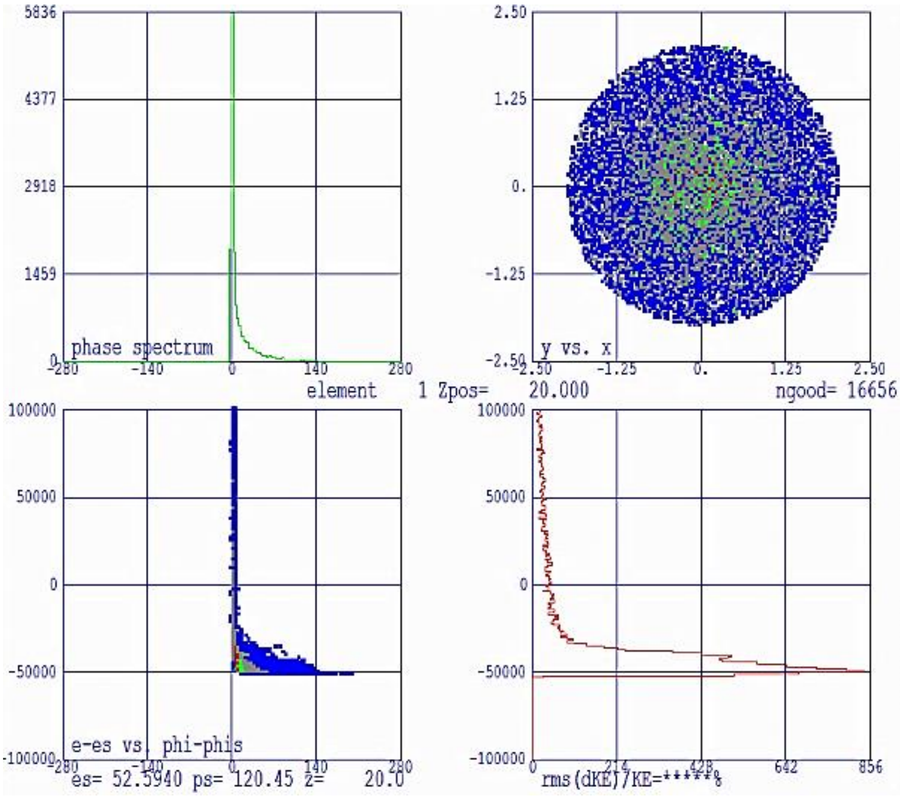

Figure 5.6 Positron distribution at the exit of AMD

Where the upper right plot is the transverse beam size in cm, the bottom left graph is the longitudinal phase space with its projection into phase in degrees (upper left) and energy in eV (bottom right). All the plots are with respect to a reference particle defined in PARMELA.

Figure.5.6 shows phase space distribution and the transverse beam size of positrons at the entrance of the pre-injector linac: AMD could capture about 35 % of positrons generated on target. In the following subsections, the design and optimization strategy of the pre-injector linac will be presented how to obtain a compact positron beam in the phase space and a good fraction of the positrons along the pre-injector linac.

5.3. The CLIC Pre-Injector Linac

A structure with the length of 1.5 m, an aperture of 20 mm and $2\pi/3$ phase advance has been chosen in the design of the CLIC pre-injector linac. The positrons need a strong focusing along the linac during the acceleration due to a large energy spread. Therefore, a long solenoid which provides a constant longitudinal magnetic field at 0.5 T is used surround accelerator structures along the CLIC pre-injector linac for the e^+

beam. Travelling Wave (TW) structures are used with a frequency of 2 GHz corresponding to the bunch repetition rate of CLIC. The distance between each TW structure is assumed to be 20 cm for the simulations to allow space for vacuum equipment and diagnostics. In the design of the pre-injector and injector linac, similar accelerating structures are used with a length of 1.5 m (TW). First, a design of RF cavity is needed to create a field map for the TW structures which can be used in PARMELA. The accelerating structure used in the whole CLIC injector complex was designed to the CDR taking into account, availability of rf power for typical klystron and the beam loading [5, 22].

In this study, the Poisson Superfish program and CST Microwave Studio are used for the design of the RF structure [23, 24]. Superfish is used for calculating electromagnetic field distribution in 2D Cartesian coordinates and axial symmetric cylindrical coordinate [23]. The Superfish input file and the detail about designing rf cavity can be found in appendix 3 and Appendix 4. The electromagnetic simulation software CST STUDIO SUITE contains various modules. One of them, CST Microwave Studio (MWS), is used for the 3D electromagnetic design of the high frequency components. It provides fast and accurate analyses of the high frequency tools such as antennas, filters, couplers and RF cavity etc. [24].

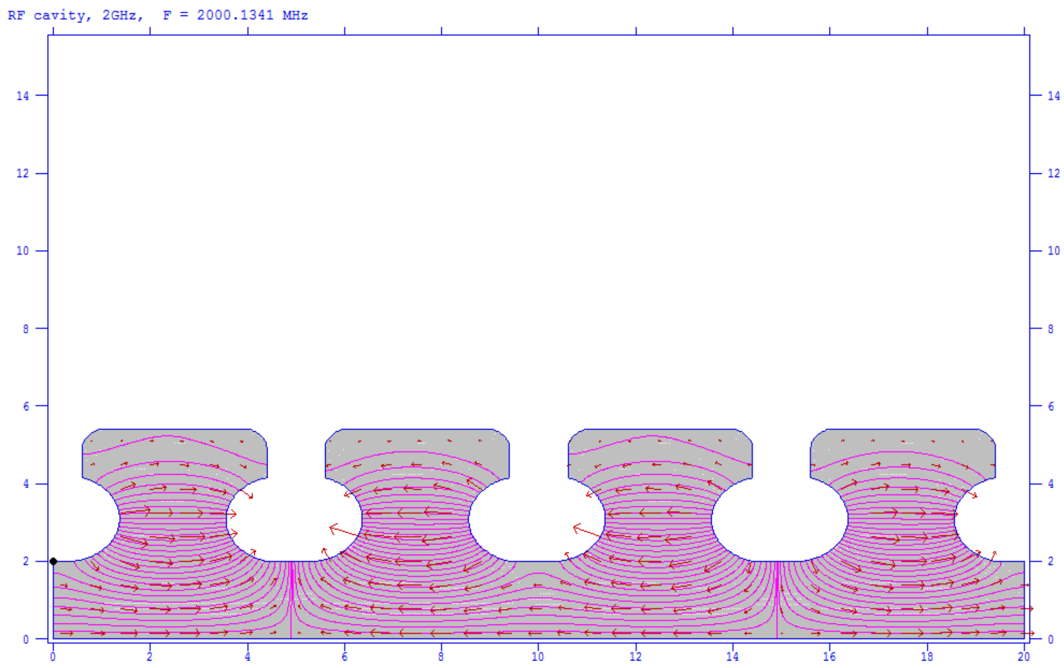

Figure 5.7 Illustrate of the electric field lines for $2\pi/3$ mode in the 2 GHz RF structure

In Fig.5.7, the electric field lines are shown for four cells of the rf cavity designed by Superfish. The mode can be seen from the direction of the electric field line at the longitudinal position. The $2\pi/3$ mode is chosen for TW structures in the simulation of the pre-injector linac. The resonance frequency of 2000.1341 MHz at $2\pi/3$ mode has been obtained in the designed rf structure and used in the simulation of the CLIC pre-injector linac.

A four cells of the rf cavity has been also designed by CST in 3D geometry to correctly model the structure compare by the Superfish design. The extracted field map from CST is converted to Superfish field format in order to use in PARMELA for the tracking simulation. The 3D geometry of the rf structure designed by CST is shown in Fig.5.8.

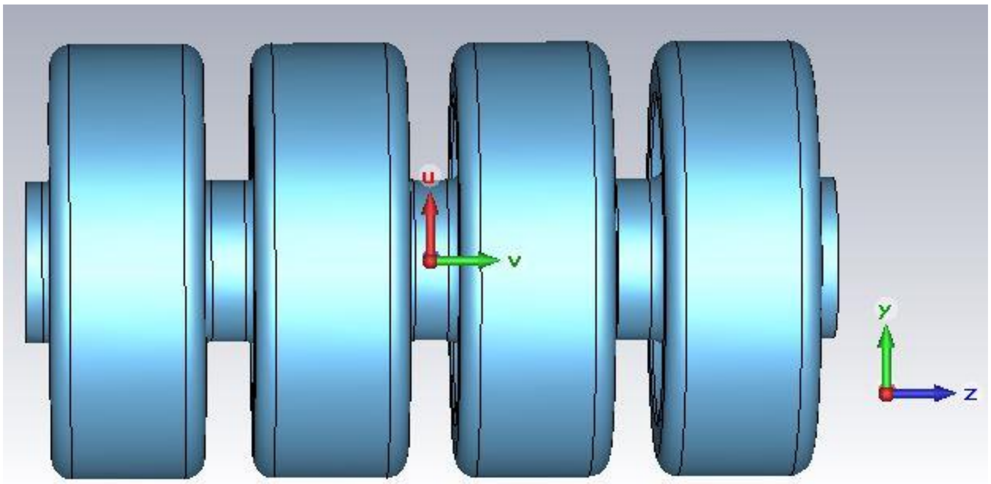

Figure 5.8 Illustrate of the 3D geometry of the 4 cells RF structure

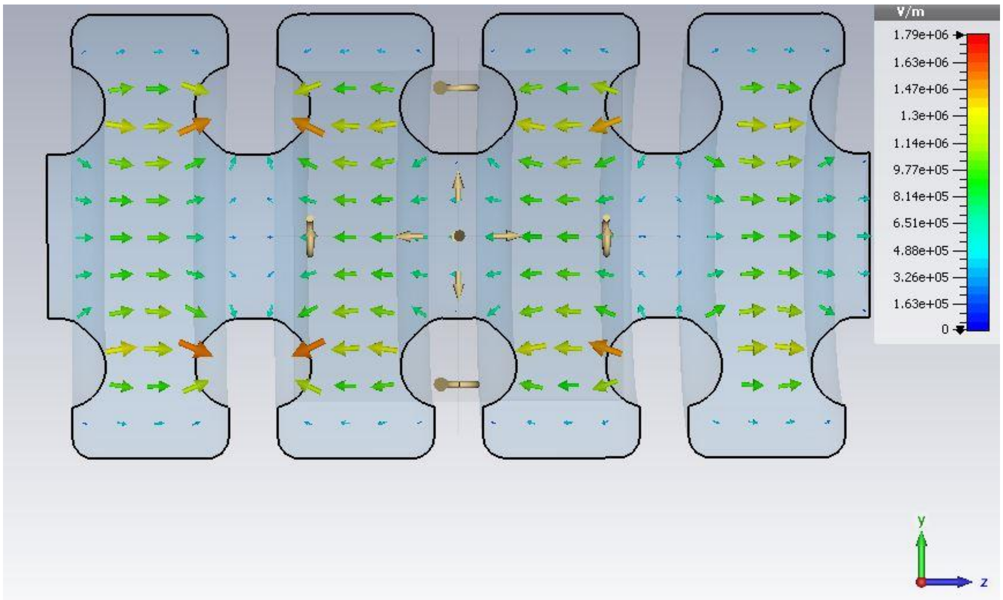

Figure 5.9 Illustrate of the electric field lines for RF structure with $2\pi/3$ mode at 2.0 GHz

The frequency scan has been done in CST, a phase advance of $2\pi/3$ is found at 2 GHz for the CLIC pre-injector linac. Figure 5.9 shows the direction of the electric field line along the structure at y-z planes. The resonant frequency of structure is 2.018852 GHz at $2\pi/3$ mode.

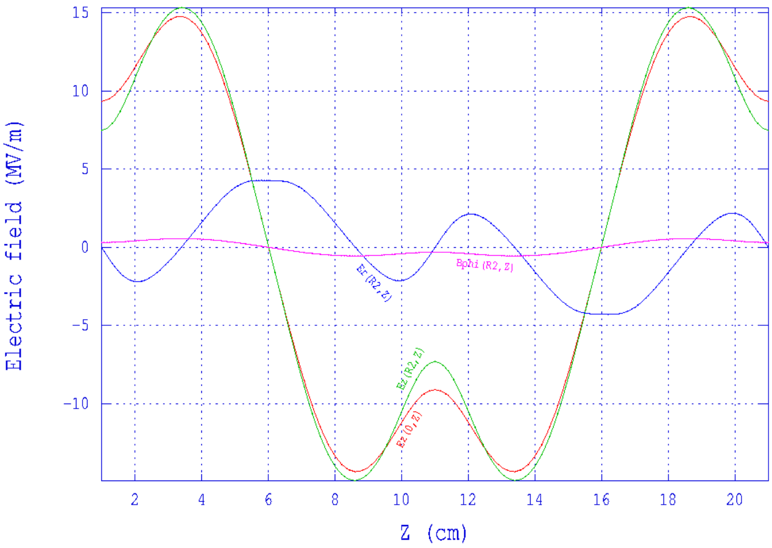

Figure 5.10 Electric field components extracted by PARMELA for rf structure designed by CST

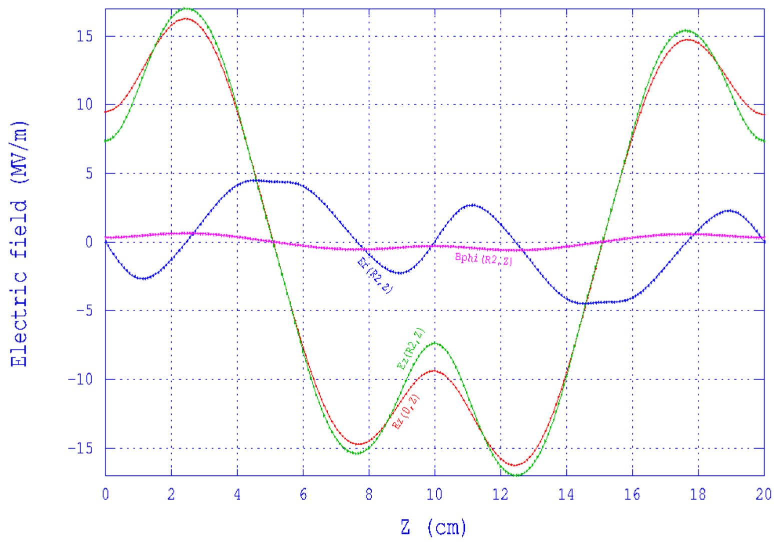

Figure 5.11 Electric field components extracted by PARMELA for rf structure designed by Superfish

The field map extracted from CST is converted to Superfish format in order to use in PARMELA, the detail information can be found in Appendix 5. In PARMELA the .T7 field map file is used and the field components are checked on z-axis. Figure 5.10 and 5.11 show that in Parmela the converted field map from CST is working very well compared to Superfish field. As a result, it is shown that there is not big difference between field maps. The converted field map from CST has been used in PARMELA for the tracking simulation of the pre-injector linac.

5.7. Longitudinal Beam Dynamics in Positron Capture

The longitudinal dynamics of the positrons is important to obtain a reasonable energy distribution at the end of the linear accelerator. In the CLIC, the pre-damping ring has an energy acceptance of ±1.2 %. Collecting the positrons within the energy acceptance window is an important issue in the design and optimization of the pre-injector linac. To accelerate or decelerate positrons a longitudinal electric field is necessary and the high frequency rf-field accelerates (or decelerates) the particles in a vacuum. The phase of rf structure has very important role for capturing positrons. To capture and accelerate the positrons, a correct phase in rf structure must be determined.

Considering cylindrical coordinates (r, θ, z) for eigenmode with cylindrical symmetry, the longitudinal electric field and the azimuthal magnetic field of the rf cavity for time-dependent t with respect to Bessel functions J_0 and J_1 in the fundamental TM_{010} mode are defined for positrons as seen in equations 5.5 and 5.6:

$$E_z(r,t) = E_0 J_0\left(\frac{\omega r}{c}\right) \sin\left(\omega t + \emptyset_0\right) \tag{5.5}$$

$$H_\theta(r,t) = -\frac{E_0}{\mu_0 c} J_1\left(\frac{\omega r}{c}\right) \cos(\omega t + \emptyset_0) \tag{5.6}$$

Here, c is the velocity of light in a vacuum, E_0 is the amplitude of electric field, ω is the resonant-frequency of rf structure, $\emptyset_0$ is phase difference, and μ_0 is permeability of vacuum.

For the particle trajectory the azimuthal magnetic field result in a deflection, but it does not affect to particle momentum. While positrons are accelerated in negative voltage, they are decelerated in positive voltage.

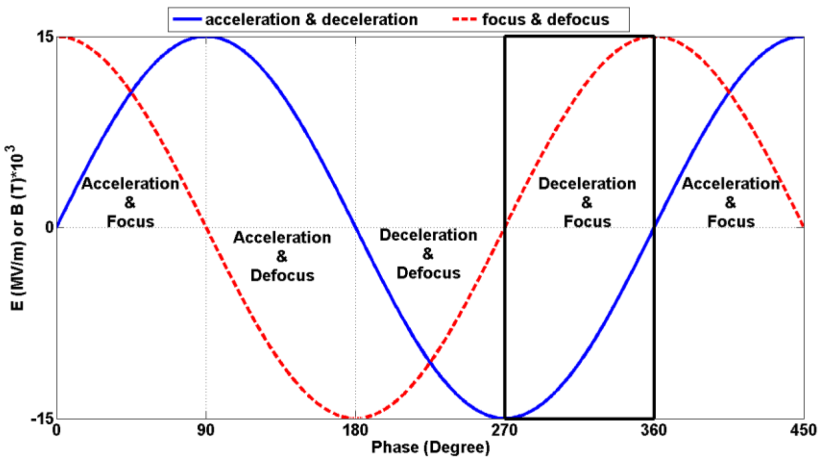

Fig. 5.12 A sketch of the electric and magnetic fields over the phase of 450 degrees

In the studies of the CLIC pre-injector linac, the accelerating and the decelerating mode have been investigated. The accelerating mode is applied on crest of the accelerating phase in the first region between 0-90 degrees and it gives the acceleration and focusing effects for positrons as seen in Fig.5.12. The decelerating mode in the CDR was used in a phase close to the maximum deceleration corresponding the third region between 180-270 degrees. In our optimization of the decelerating mode, the fourth region including deceleration and focusing effects between 270-360 degrees has been chosen with a phase of 310 degrees due to give a more compact positron beam and capture more particles at the exit of the pre-injector linac.

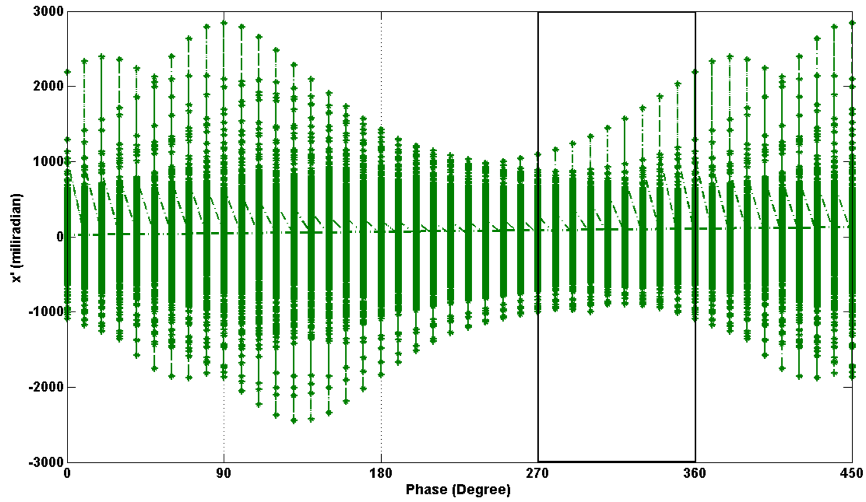

Fig. 5.13 rf focusing effect by a single cell in the divergence coordinate versus rf phase over the phase of 450 degrees for positrons

Figure 5.13 show the rf focusing effect by a single cell for positrons over the phase of 450 degrees in the divergence coordinate. The positrons are significantly affected from the rf phase in capturing process due to a large transverse phase space distribution. Choosing the optimized phase has an important role to increase the positron yield. As considering this context, the accelerating mode, the decelerating mode and the optimized decelerating mode will be presented in the following subchapters.

5.8. The Accelerating Mode in the CLIC Pre-Injector Linac

In the linac design, the traditional approach is to accelerate and transport charged particles as quickly as possible with little loses. The accelerating mode based on this approach has been used for positrons straight after AMD. In the accelerating mode, we placed the center of the positron distribution on the crest of the accelerating field, and accelerated with a 15 MV/m gradient in each structure. The drift space between structures was chosen to be 20 cm. In this configuration the total length of the pre-injector linac is about 14 m, using 8 accelerating structures whose parameters are summarized in table 5.1. All the simulations of the CLIC pre-injector linac were performed using the particle tracking code PARMELA [19].

Table 5.1 General parameters of the CLIC pre-injector linac in the accelerating mode

Parameter	Value
Total length [m]	~14
Maximum accelerating gradient [MV/m]	15
Number of accelerating structure	8
Length of accelerating structure (30 cells) [m]	1.5
Energy gain [MeV]	22.5

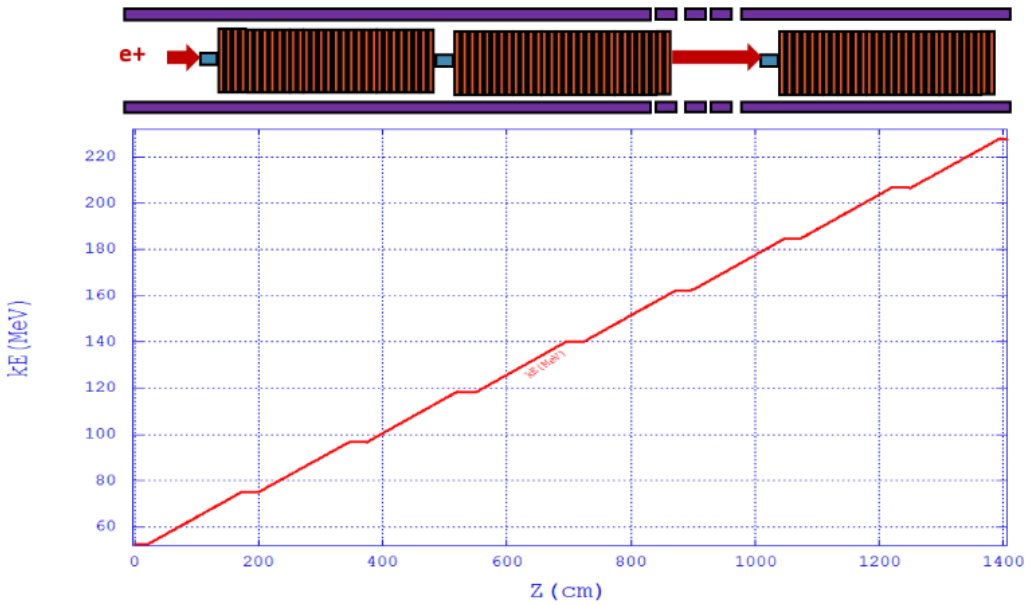

Fig. 5.14 Energy profile along the pre-injector linac in the accelerating mode.

Figure 5.14 shows the energy profile for the reference particle along the pre-injector linac in the accelerating mode. Although the energy of reference particle exceeds the target energy in Fig.5.14, the mean energy is around 200 MeV for all positrons in the exit of the pre-injector linac due to large energy spread as seen in Fig.5.15. The longitudinal phase space obtained at the exit of the pre-injector linac can be seen in Fig.5.16.

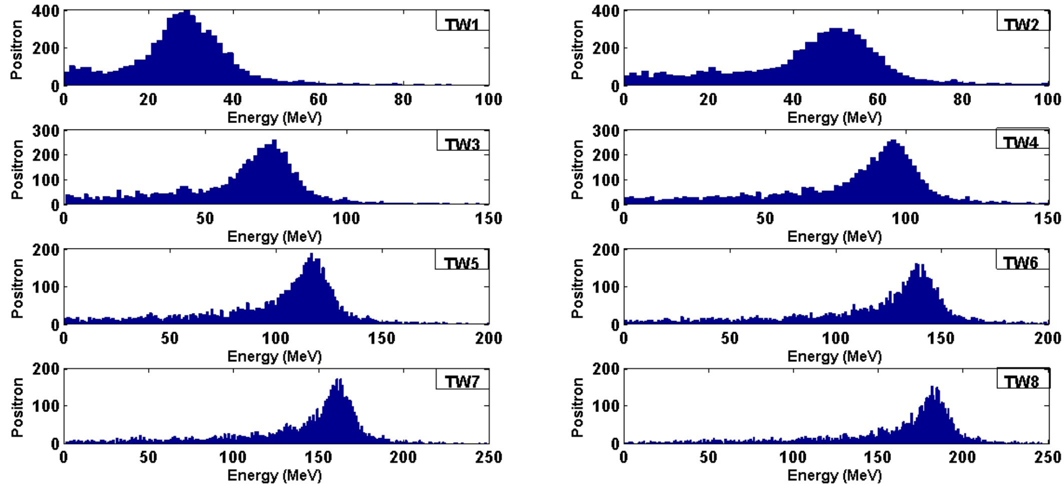

Figure 5.15 Energy spectrum of positrons for the accelerating mode at the exit of each TW (Traveling Wave) structure along the pre-injector linac.

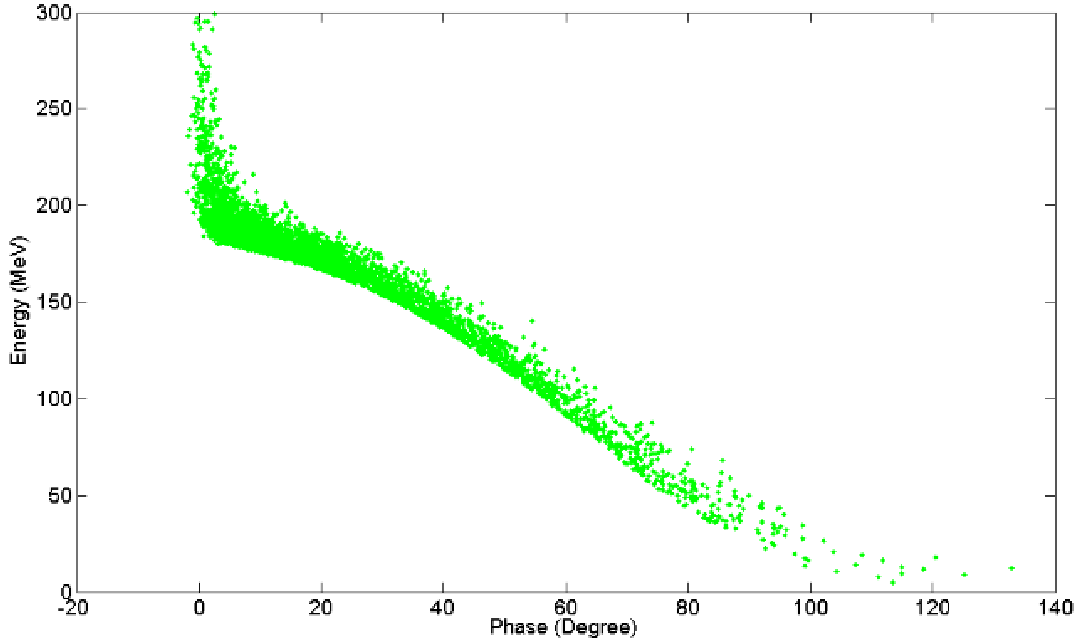

Figure 5.16 Energy and phase distribution for the accelerating mode in the end of pre-injector linac

In the end of the pre-injector linac, the simulation results showed that the total positron yield including all particles, is 0.89 e^+/e^-, meaning that only about 10% of the produced positrons are captured. Since one is interested in optimizing the yield of positrons, which likely will end up within the acceptance of the pre-damping ring, we defined for the optimization as a figure of merit an effective yield describing the particles which are in ±20 degrees and ±50 MeV energy window. After simulations, the corresponding effective yield has been found around 0.5 e^+/e^- in the acceleration mode. These results are comparable with earlier studies on CLIC CDR [5, 15 and 25].

5.9. The Decelerating Mode in the CLIC Pre-Injector Linac

The decelerating mode was applied in the pre-injector linac using a phase close to maximum deceleration in the first structure [5, 15]. A modest gradient of 6 MV/m for the deceleration in the first structure was applied. As a beginning, we have verified the results of the CDR studies.

Table 5.2 General parameters of the CLIC pre-injector linac in the decelerating mode

Parameter	Value
Total length [m]	~17
Maximum accelerating gradient [MV/m]	15
Maximum decelerating gradient [MV/m]	6
Number of accelerating structure	10
Length of accelerating structure (30 cells) [m]	1.5
Energy gain [MeV]	22.5

Figure 5.17 shows the energy change of the reference particle along the beam line in the decelerating mode. In the first structure, the deceleration is applied and therefore a longer beam line about 17 m in total is needed to get an energy of roughly 200 MeV as seen in table 5.2.

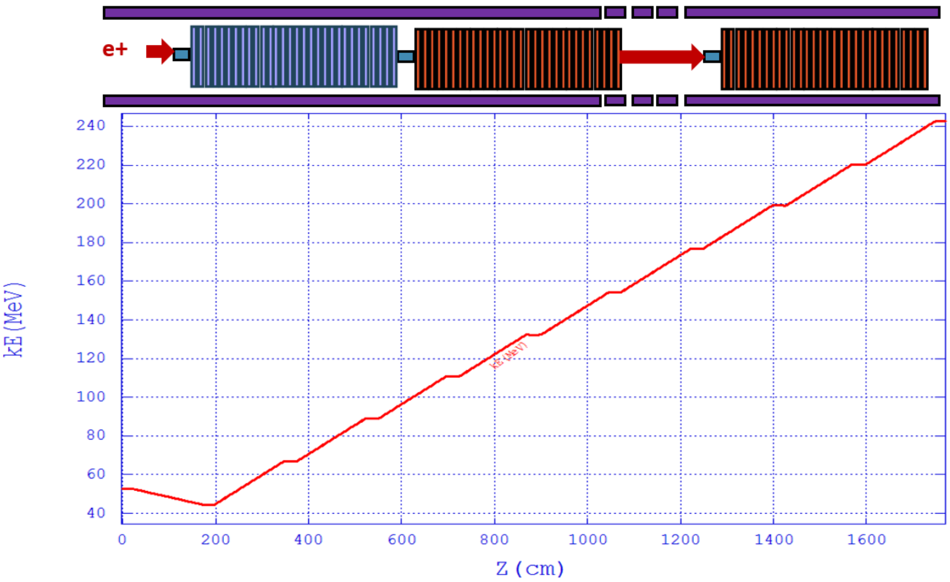

Fig. 5.17 Energy profile along the pre-injector linac in the decelerating mode

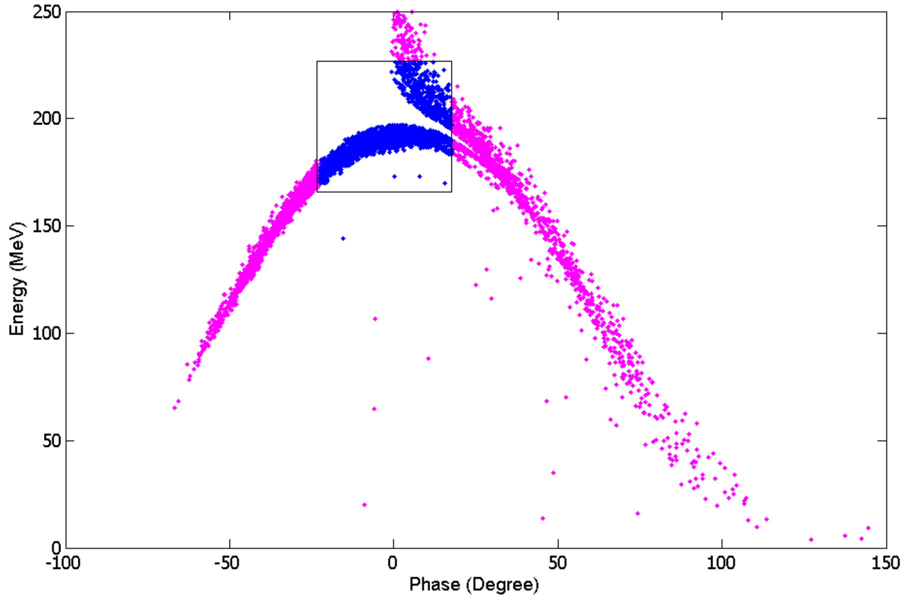

Fig. 5.18 Energy and phase distribution in the end of pre-injector linac in the decelerating mode

In figure 5.18, the longitudinal distribution of positrons in the decelerating mode is shown. Compared to the accelerating mode, more positrons are captured in total. The total yield is 0.93 e^+/e^- and the effective yield defined in ±20 degrees and ±50 MeV energy window is around 0.48 e^+/e^- agreeing well with previous results documented in the CDR.

5.10. Optimization of the CLIC Pre-Injector Linac in the Decelerating Mode

For a better understanding the trapping of the positrons during deceleration and acceleration, the process was simulated in detail varying the phase of the accelerating fields over the full range of 360 degrees. The result was that the phase range between maximum deceleration and the following zero-crossing is optimal for capturing the positrons with such an initial distribution. Here the fields provide eventually both focusing and acceleration. For our case a phase of 40 degrees after maximum deceleration turned out to be optimum. The different phases used in the simulations are illustrated in figure 5.19. The positrons are first decelerated but split over into the accelerating phases already in the first structure.

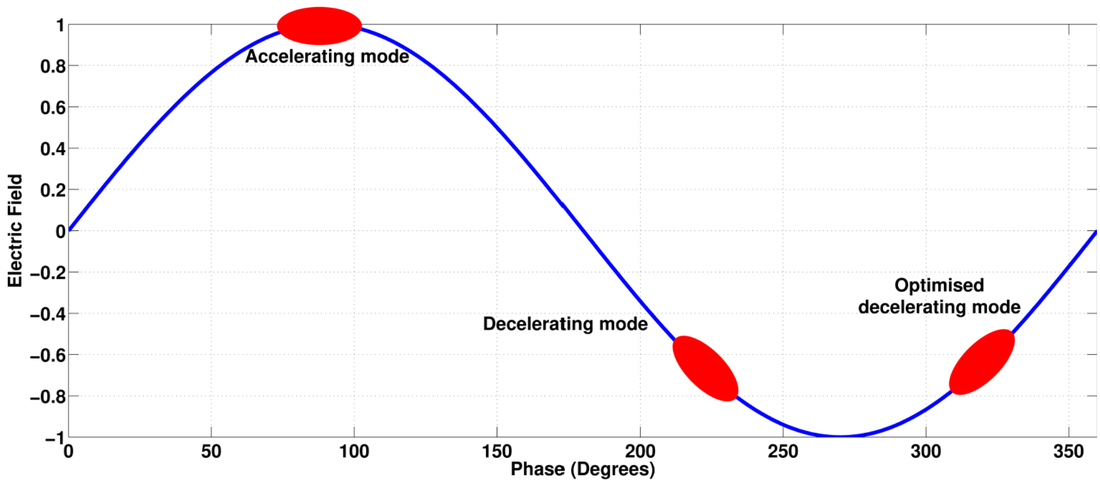

Fig. 5.19 A sketch of the electric filed with ‘bunches’ placed on the different phases for acceleration, deceleration (CDR) and optimized deceleration

Looking at the phase spectrum during this process independent of the phase initially chosen one can notice that particles get trapped into at least two adjacent rf buckets due to the large energy spread. By choosing the phase one can control the amount of particles trapped in either bucket. The accelerating mode collects most of its particles in the first rf bucket keeping them on crest whereas the decelerating mode shuffles more particles in the following rf bucket. The optimum yield was found maximizing the second peak of the phase distribution in the first structure and then accelerating this peak on crest in the rest of the linac, see Fig.5.20, Fig.5.21 and Fig.5.22. The results have a better yield and, even more importantly, a better phase space distribution. A nice compact peak is obtained in the phase and energy distribution.

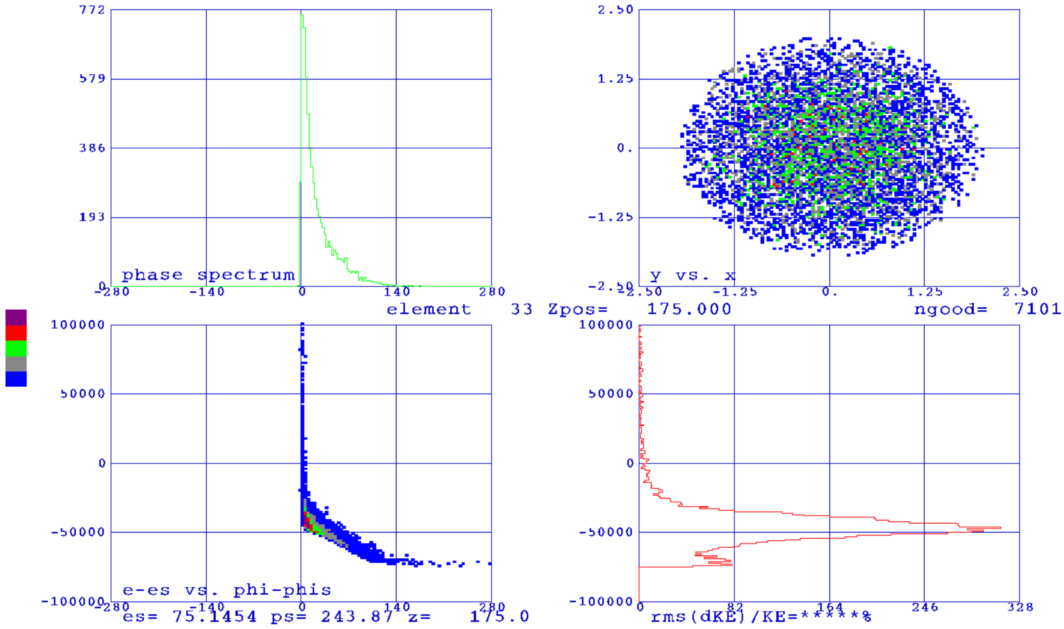

Fig. 5.20 Positron distribution in a phase of accelerating on crest for the accelerating mode at the exit of the first structure.
The explanations of graph axes are same as Fig.5.6.

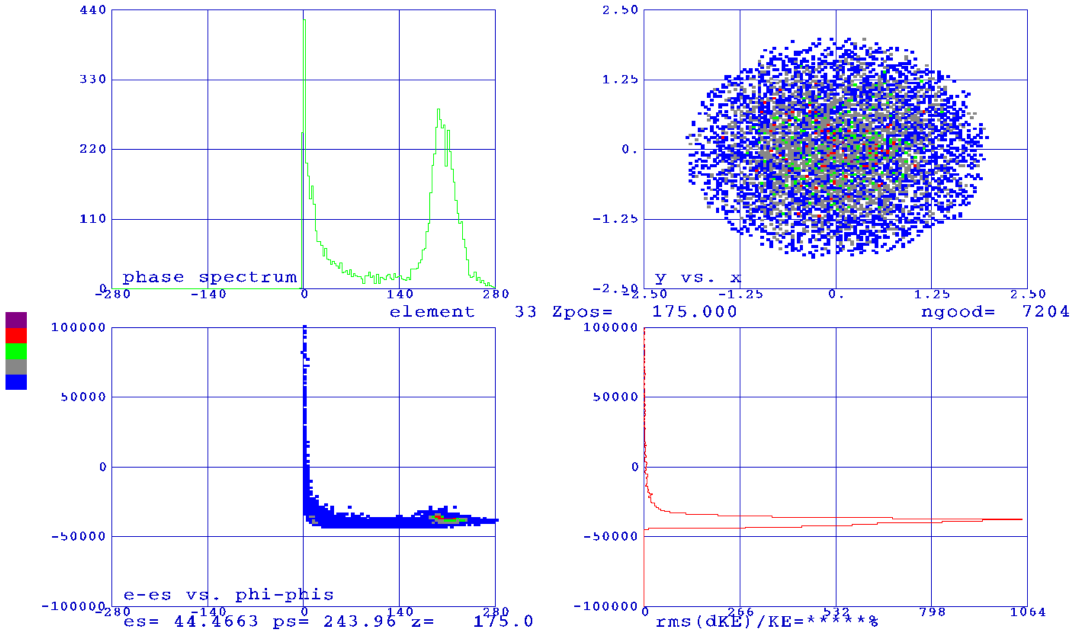

Fig. 5.21 Positron distribution in a phase of decelerating closed to maximum deceleration for the decelerating mode at the exit of the first structure.
The explanations of graph axes are same as Fig.5.6.

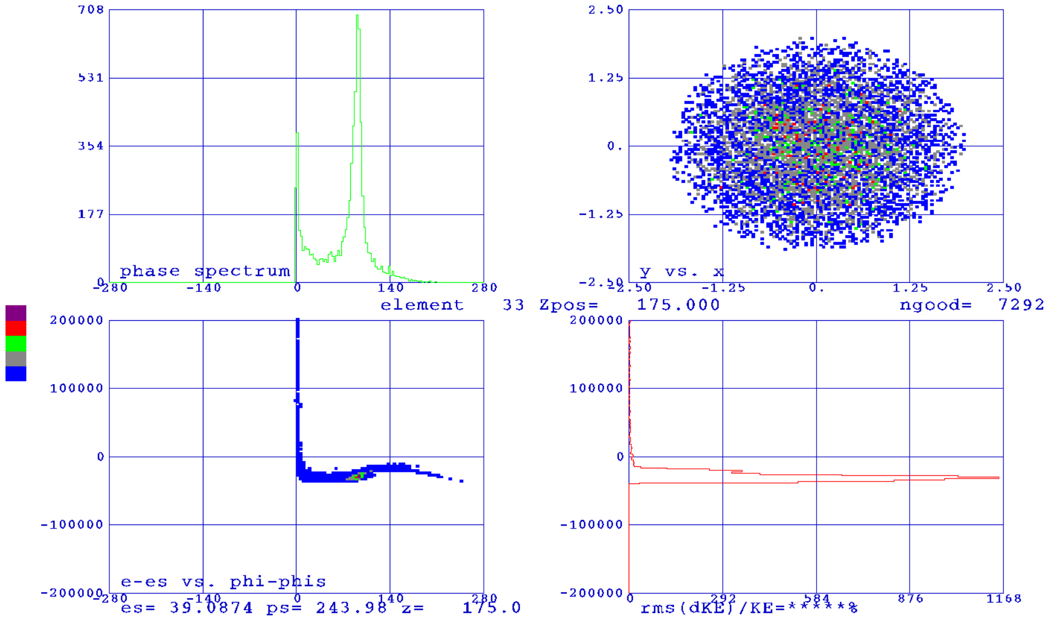

Fig. 5.22 Positron distribution in a phase of 40 degrees after maximum deceleration for the optimized decelerating mode at the exit of the first structure.

The explanations of graph axes are same as Fig.5.6.

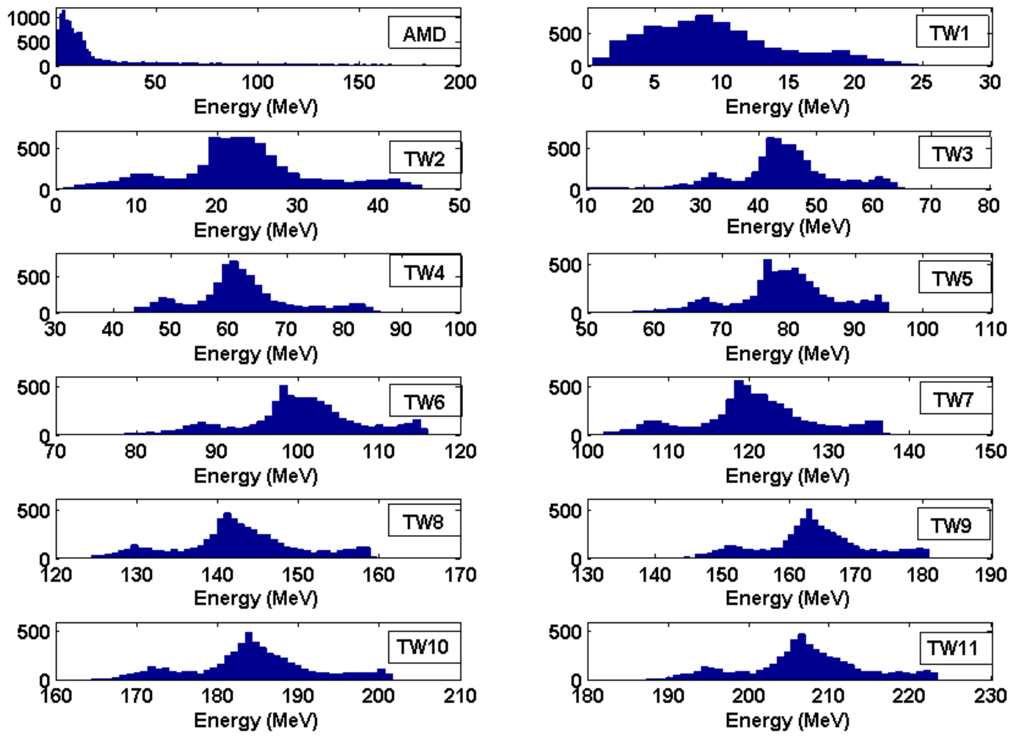

Figure 5.23 Energy spectrum of positrons for the optimized decelerating mode at the exit of each structure along the pre-injector linac.

TW: Traveling wave Structure

Figure 5.23 shows energy spectrum of positrons for each structure along the pre-injector linac. This figure describes the energy changing versus positron population at the exit of each structure. It is seen that after applying deceleration on the optimized phase in the first accelerating structure positrons have a low mean energy around 10 MeV at the exit of the first structure.

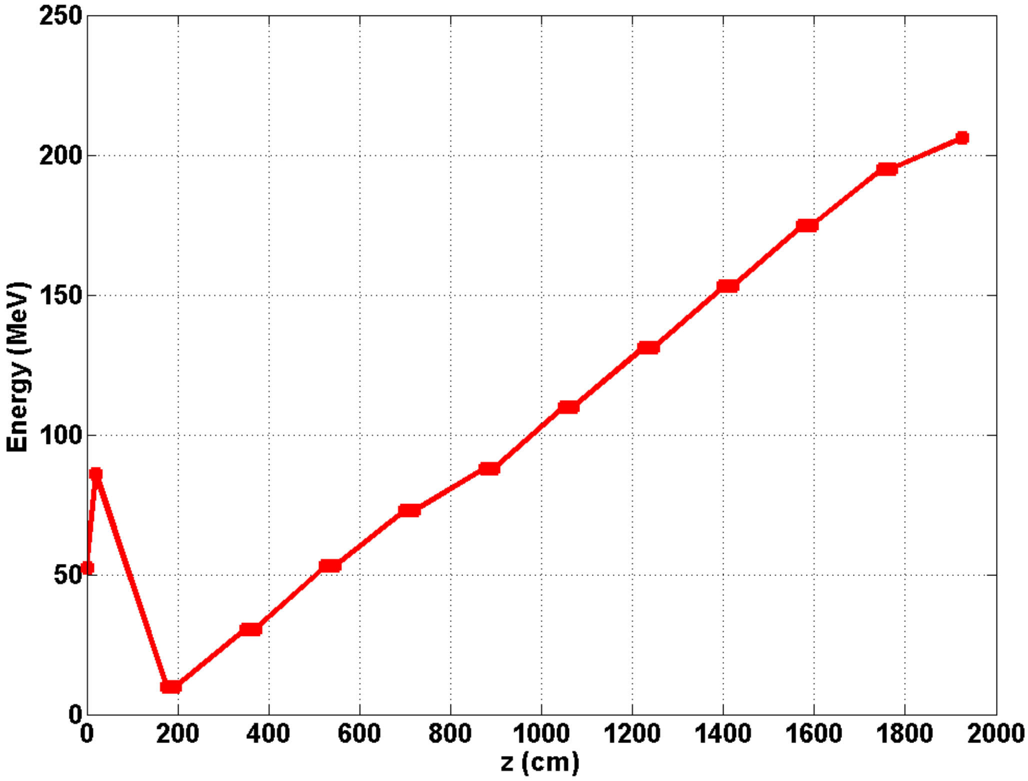

Figure 5.24 Mean energy profile along the CLIC pre-injector linac in the optimized decelerating mode.
The decelerating mode requires 3 additional accelerating structures to bring the energy up to 200 MeV.

Figure 5.24 shows the mean energy of positrons along the beam line in the optimized decelerating mode. The mean energy of positrons is about 50 MeV at the exit of the target and it is around 80 MeV after the AMD as seen in Fig.5.24, because low energy positrons are lost very quickly. In the first structure, the deceleration is applied in the optimum phase and therefore a longer beam line about 19 m in total is needed to get to 200 MeV as seen in table 5.3.

Table 5.3 General parameters of the CLIC pre-injector linac in the optimized decelerating mode

Parameter	Value
Total length [m]	~19
Maximum accelerating gradient [MV/m]	15
Maximum decelerating gradient [MV/m]	12
Number of accelerating structure	11
Length of accelerating structure (30 cells) [m]	1.5
Energy gain [MeV]	22.5

Besides the phase in the first structure, another important parameter is the deceleration gradient. The deceleration gradient is scanned for different values in terms of positron yield. A high gradient of at least 12 MV/m is favored for the decelerating mode (see Fig.5.25). While the total yield is not affected dramatically, the higher gradient results in a narrower phase and energy spectrum.

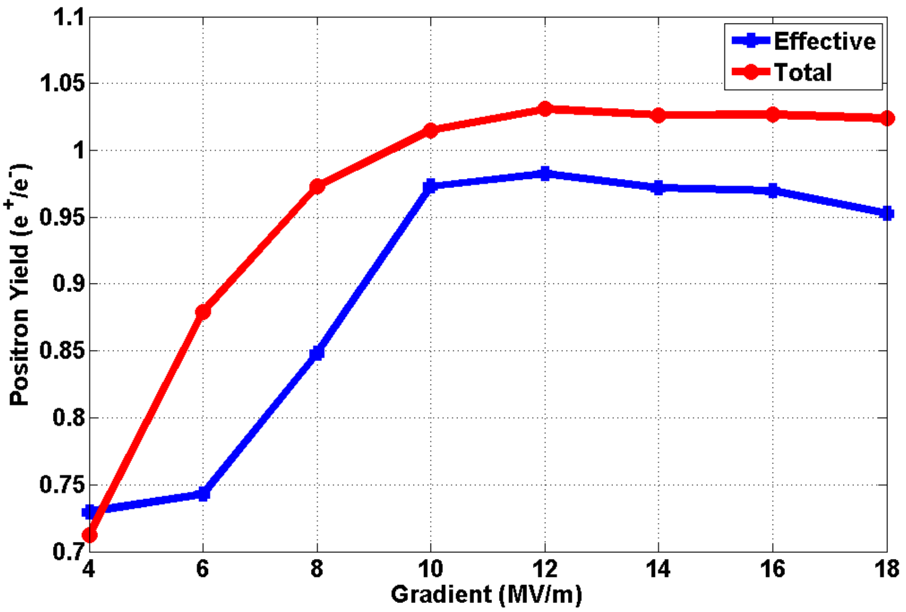

Figure 5.25 Positron yield at the end of pre-injector linac versus the gradient of the first structure

Figures 5.26 and 5.27 compare the longitudinal phase space at the end of the pre-injector linac for the accelerating mode and the optimized decelerating mode. It is clearly visible that accelerating on crest right away results in a large tail in the distribution while in the deceleration case it is possible to fold in a good fraction of the particles otherwise ending up in the tail. In this case the total yield is 1.09 e+/e- and the effective yield defined in ±20 degrees and ±50 MeV energy window is around 0.98 e+/e- at the exit of the pre-injector linac showing that the main benefit is a better suited longitudinal phase space for acceptance into the damping ring. Therefore the optimized decelerating mode result in almost a factor two higher yield compared to the accelerating mode which has a yield of 0.5 e+/e-.

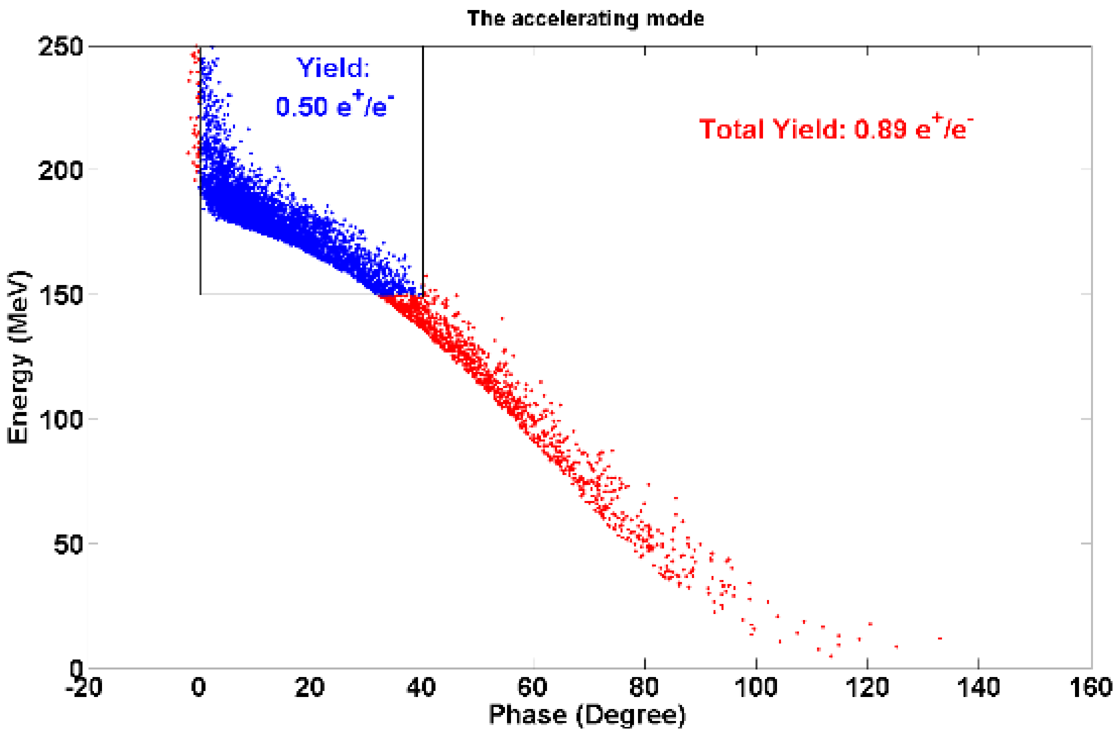

Figure 5.26 Longitudinal phase space for the accelerating mode

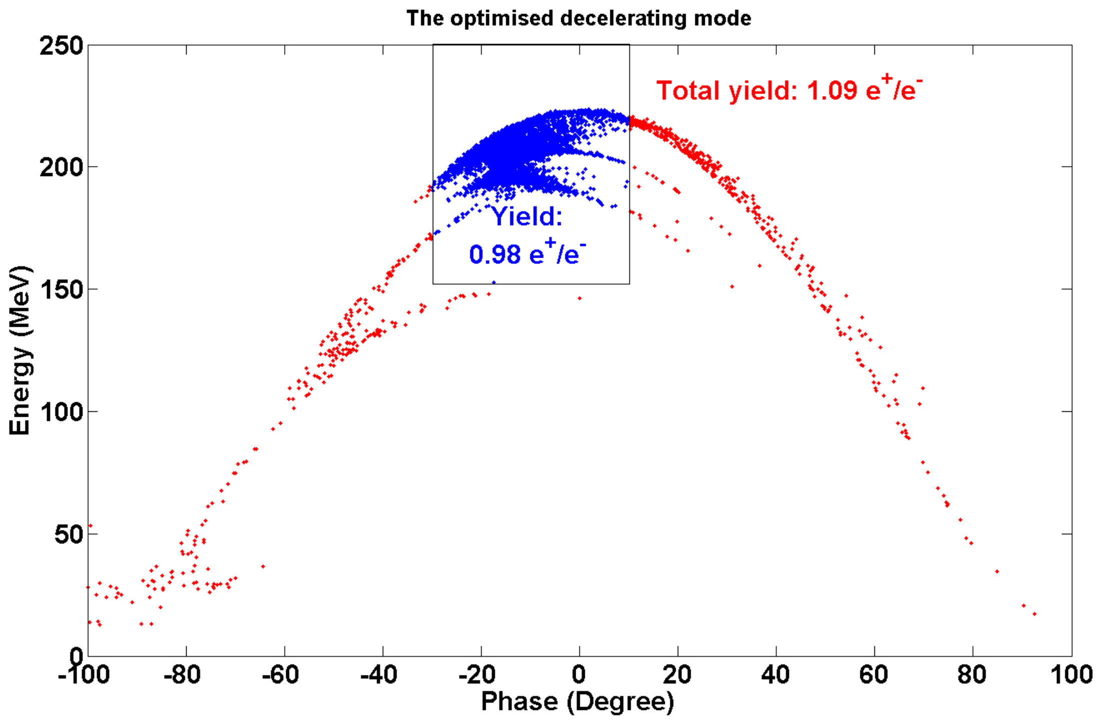

Figure 5.27 Longitudinal phase space for the optimized decelerating mode

5.11. Additional Studies in AMD and the Capture Linac

In the optimization of the CLIC positron source, the main idea is to increase positron yield efficiently before injection into acceptance window of pre-damping ring. Positrons need a strong focusing after the target due to a large energy spread and divergence phase. There are various possibilities to increase the positron yield. One of them is to increase the magnetic field in AMD and solenoid which is surrounded rf structures. For the previous studies in this chapter, the magnetic field of AMD was used from 6T down to 0.5 T and the solenoidal field which is surrounded rf structures was fixed at 0.5T. In the alternative scenario, two options are considered for the magnetic field of AMD. First is to use AMD which the magnetic field is decreased from 6 T to 1.0 T. Second option is to use the one which magnetic field changes from 6 T to 1.5 T.

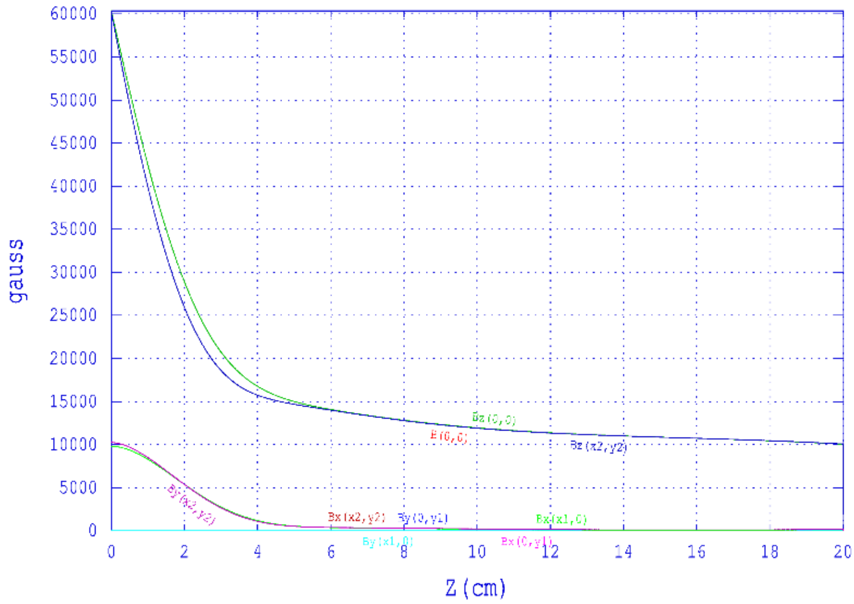

Figure 5.28 A stronger longitudinal magnetic field of AMD from 6 T to 1T

Figure 5.28 shows the longitudinal magnetic field of AMD for a stronger magnetic field which is from 6 T down to 1.0 T at 20 cm. At the exit of the AMD, the positron yield has been obtained around 4.18 e^+/e^- and it was around 2.8 e^+/e^- for 0.5 T option in our previous study.

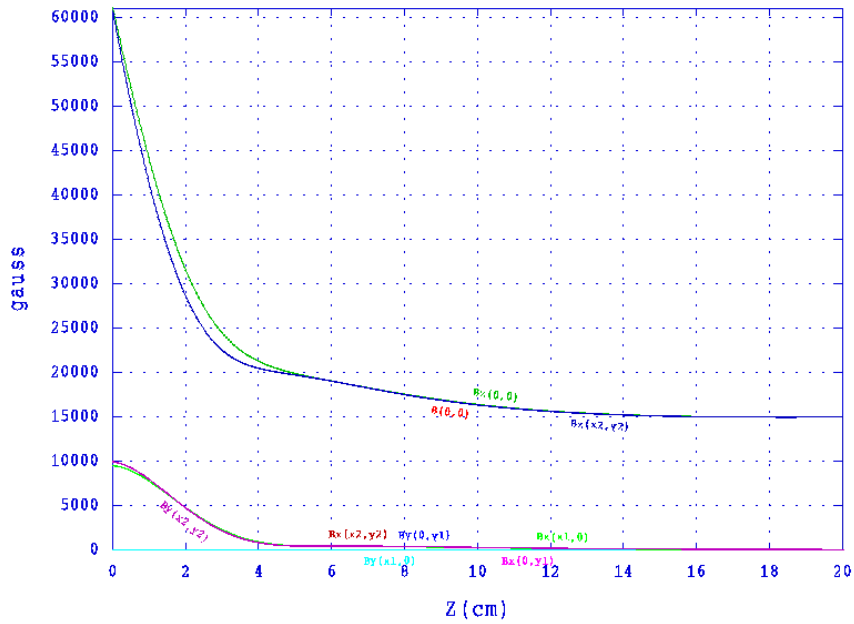

Figure 5.29 A stronger longitudinal magnetic field of AMD from 6 T to 1.5T

Figure 5.29 shows the longitudinal magnetic field of AMD decreased from 6 T down to 1.5 T. At the exit of the AMD, the positron yield is around 3.77 e^+/e^-.

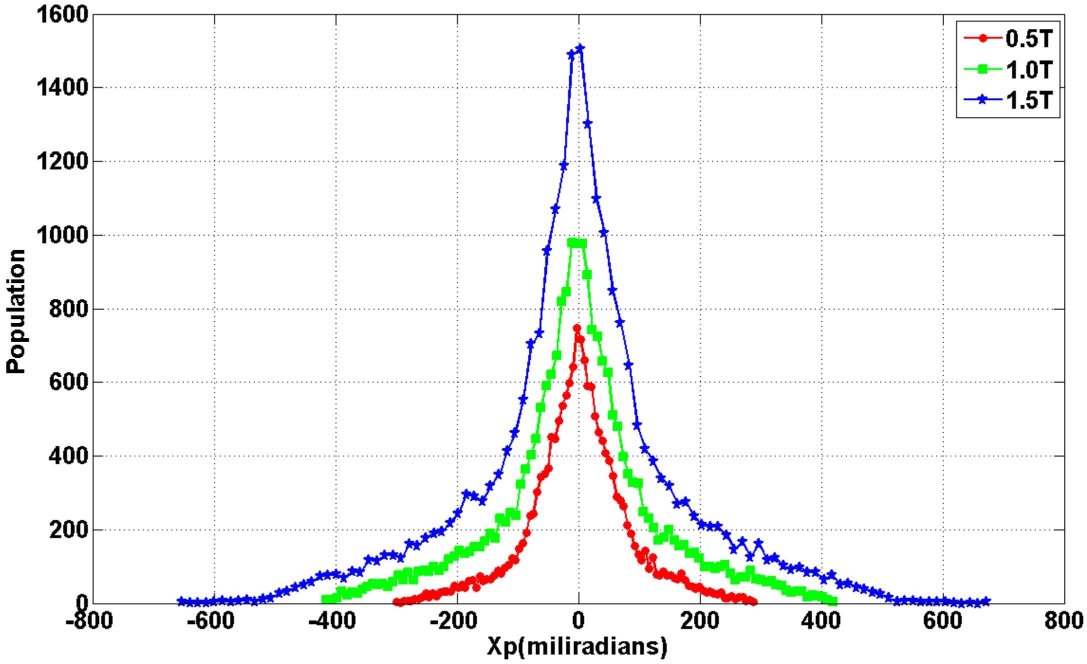

5.30 Divergence spectrum of positrons at the exit of the AMD

The divergence plot (see Fig.5.30) shows that we can dramatically increase the positron yield after the AMD but unfortunately the final yield at the end of the injector linac increases less due to the limited aperture of the linac. In this cases, accelerator structures after AMD are embedded into a solenoidal magnetic field of 0.5 T, 1.0 T and 1.5 T respectively for three options along the pre-injector linac.

Figure 5.31 shows positron distribution at the longitudinal phase space for the optimized decelerating mode at 1.0 T option. At the exit of the pre-injector linac, the total yield is around 1.53 e^+/e^- and the effective yield is 1.20 e^+/e^- in a ±20 degrees and ±50 MeV energy window.

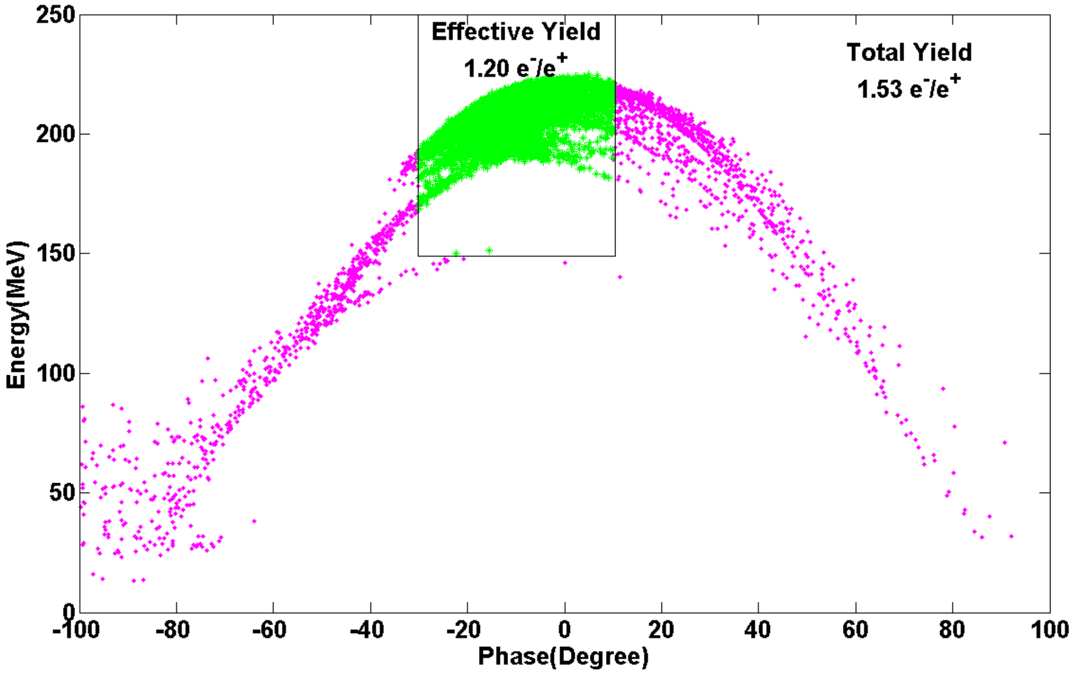

Figure 5.31 Longitudinal phase space with a stronger longitudinal magnetic field at 1.0 T at the exit of the pre-injector linac

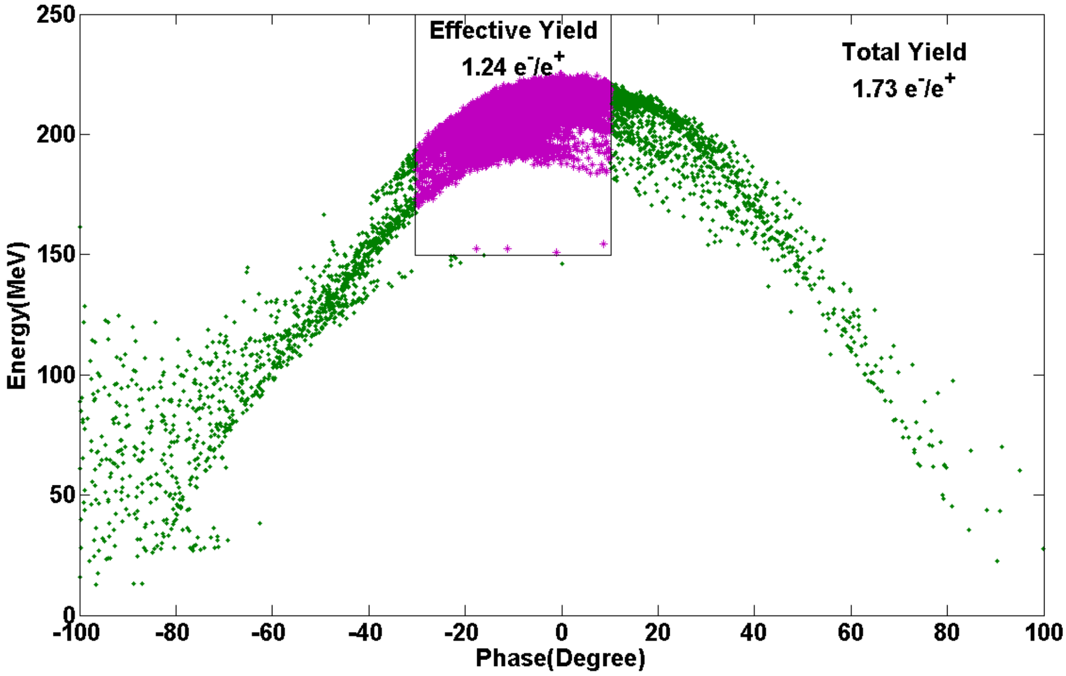

Figure 5.32 Longitudinal phase space with a stronger longitudinal magnetic field at 1.5 T at the exit of the pre-injector linac

Figure 5.32 shows positron distribution at the longitudinal phase space for the optimized decelerating mode at 1.5T option. At the exit of the pre-injector linac, the total yield is around 1.73 e^+/e^- and the effective yield is 1.24 e^+/e^- in a ±20 degrees and ±50 MeV energy window as seen in table 5.4.

Table 5.4: Positron Yield at the exit of the CLIC pre-injector linac in the optimized decelerating mode

AMD field [T]	Total Yield after AMD (e^-/e^+)	Solenoid field [T]	Total yield at 200 MeV (e^-/e^+)	Effective Yield at 200 MeV (e^-/e^+)
From 6 down to 0.5	2.8	0.5	1.09	0.98
From 6 down to 1.0	3.7	1.0	1.53	1.20
From 6 down to 1.5	4.1	1.5	1.24	1.73

Besides the stronger magnetic field, phase, decelerating gradient and length in the first accelerating structure are determinative parameters for positron yield. In the optimization of the pre-injector linac embedded into a solenoidal magnetic field of 0.5 T, the optimum phase and decelerating gradient have been already obtained in our previous study. Another important parameter is the length of the first accelerating structure for positron yield. In Fig.5.33, the length of the first structure, L, has been scanned for different values by using the optimized decelerating gradient to 12 MV/m and the optimized rf phase in the pre-injector linac.

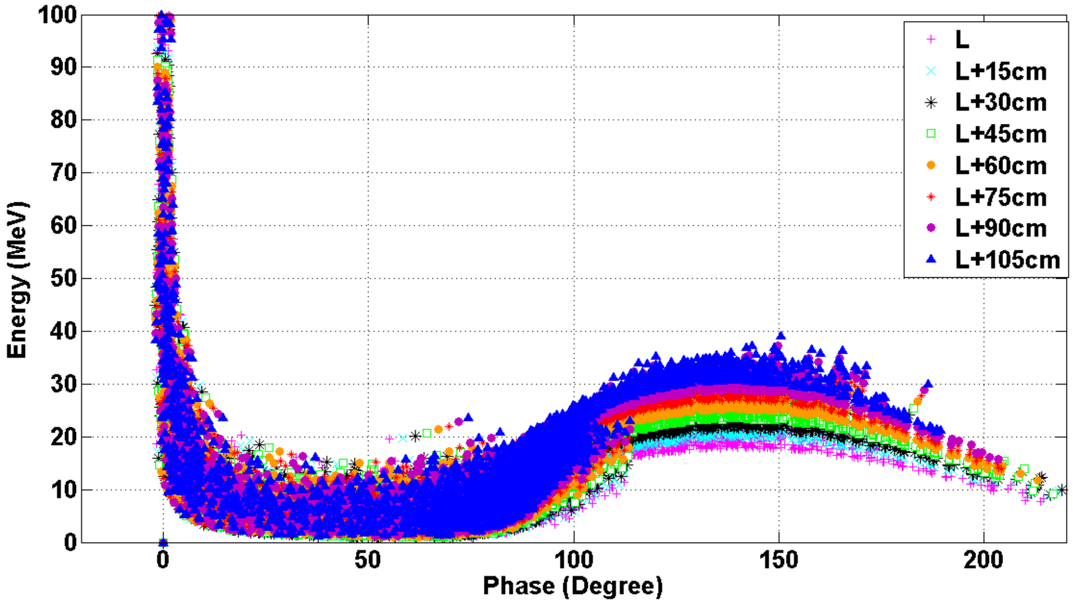

Figure 5.33 Longitudinal phase space at the exit of the first accelerating structure for different length values. L: nominal value of the accelerating structure in the simulation

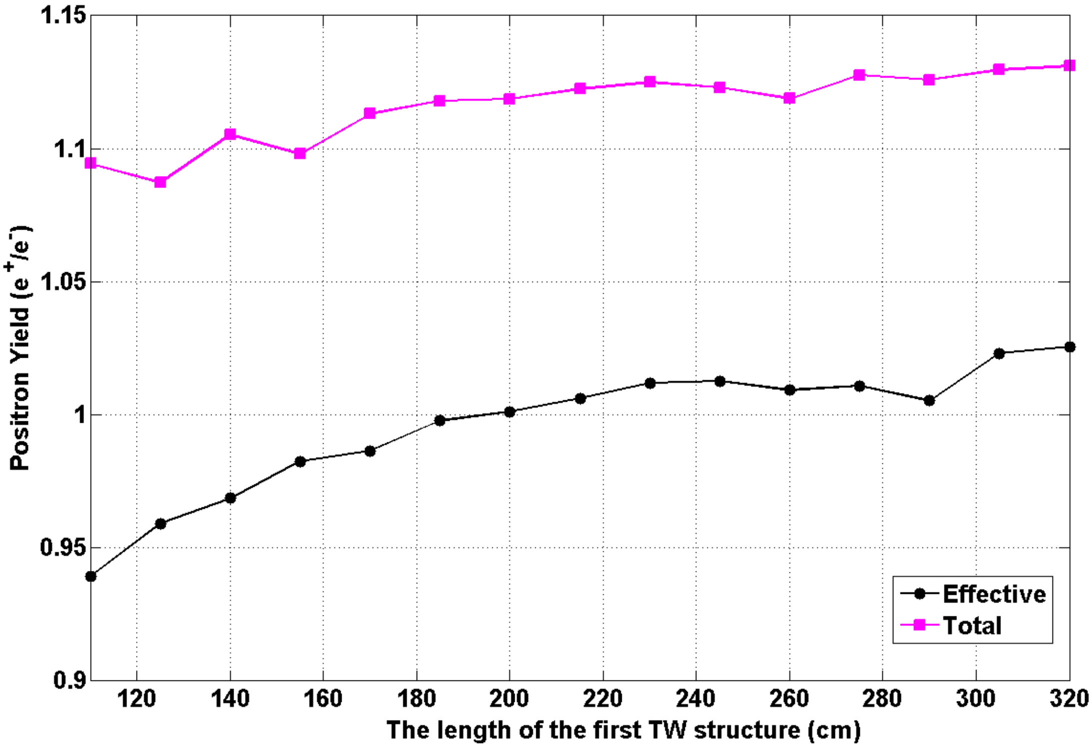

Figure 5.34 Positron yield at the exit of the pre-injector linac for the different length values of the first structure

In the optimized decelerating mode, the center of the positron distribution was placed with a phase of 40 degrees after maximum deceleration. Applying deceleration with a longer length in the first structure was shown that more deceleration result in capturing more positrons at the exit of the first accelerating structure in the second peak corresponding to tail of the beam as seen in Fig.5.33.

In Fig.5.34, it is shown that applying deceleration in the first structure with a longer length could be increased the positron yield at the exit of the pre-injector linac. It means the positron yield could be increased by optimizing the second accelerating structure due to desire using a length of 1.5 m TW.

Another issue is minimum radius of AMD. It is known that an ideal AMD has a tapered radius along z axis. Although a constant radius of 20 mm was used for AMD in all simulations, we have obtained a limit for the minimum radius of AMD. The AMD is modelled for different values of minimum radius and it is scanned from 6 mm to 15 mm as seen in Fig.5.35. Here, the maximum aperture of AMD is accepted similar with beam pipe radius of 20 mm.

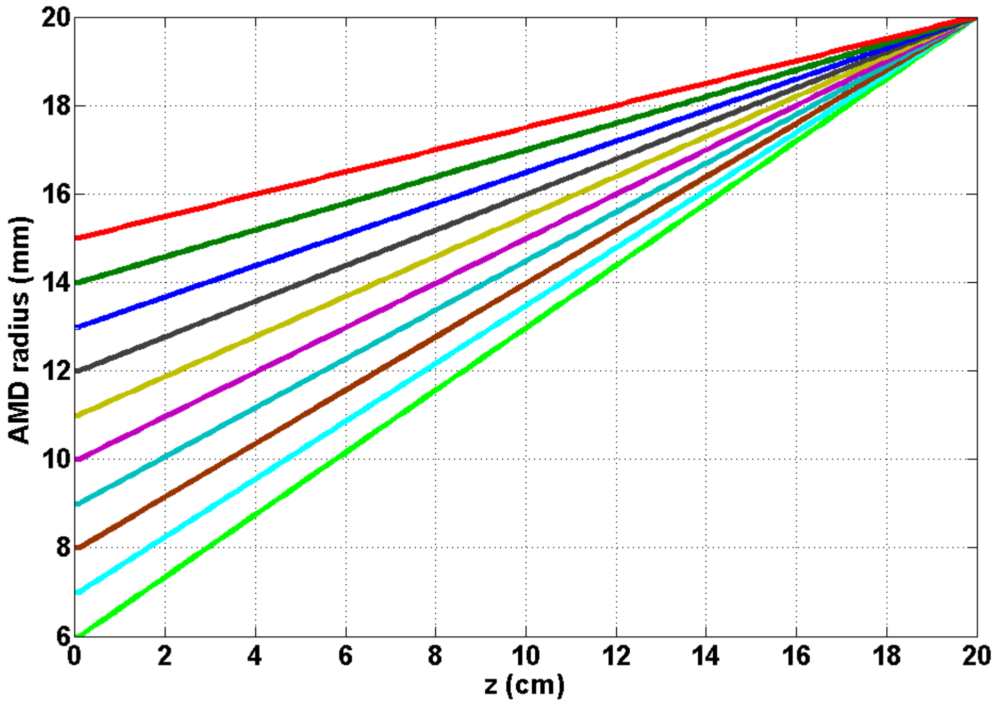

Figure 5.35 AMD radius along z axis for different values of minimum radius

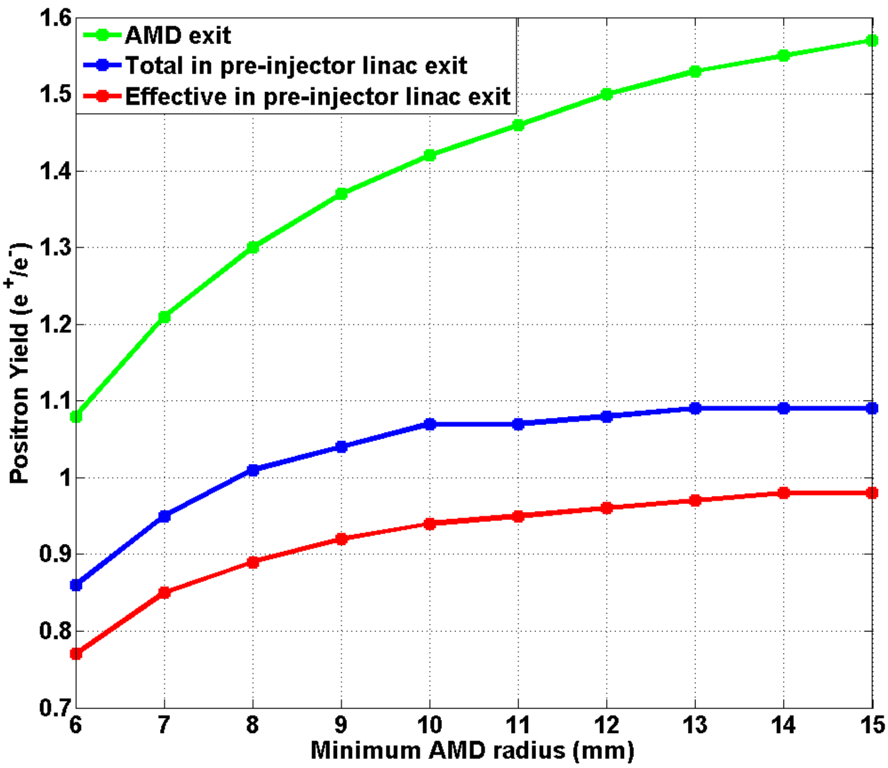

Figure 5.36 Positron yields for different aperture values of AMD

As seen in Fig.5.36, although a small AMD aperture dramatically decrease the positron yield at the exit of AMD, it does not affect so much the effective yield in a ±20 degrees and ±50 MeV energy window and total yield at the exit of the pre-injector linac. As a result, if it is desired to obtain the similar positron yield in our previous result, the minimum AMD radius should be bigger than 14 mm as seen in table 5.5. However, even if a minimum aperture of 6 mm is used, the effective yield is around 0.77 e^+/e^- meaning that about 80% of the positrons in our previous study are captured.

Table 5.5 Positron Yield for small and constant aperture AMD

AMD radius	Total Yield after AMD (e^-/e^+)	Solenoid field [T]	Total yield at 200 MeV (e^-/e^+)	Effective Yield at 200 MeV (e^-/e^+)
From 14 mm to 20 mm	1.55	0.5	1.09	0.98
20 mm (constant)	2.8	0.5	1.09	0.98

6. OPTIMASITION OF THE CLIC INJECTOR LINAC

In the CLIC positron source, the CLIC injector linac is supposed to accelerate positron beams and electron beams simultaneously from 200 MeV after the pre-injector up to the damping ring energy of 2.86 GeV. The optics design of the injector linac has been done for the positrons since the emittance of the positron beam is much larger compared to the electron beams.

First conceptual studies of the injector linac were performed for the CLIC CDR [14, 26, 27 and 28]. The main strategy of the design was to transport the beam with as little loses as possible from the pre-injector linac to the pre-damping ring and if necessary optimize the longitudinal phase space to match the acceptance of the pre-damping ring.

The main limiting factor for the beam transport is the aperture of the linac due to the large transverse emittance of the positron beam. In the previous design studies mostly triplet lattices have been used followed by a bunch compressor in the end of the pre-injector linac to rotate the phase space to maximize the yield into the damping ring longitudinal acceptance. In our new study in this thesis, several sections of FODO lattices are used along the whole linac and a rotation of the phase space is no longer required due to the optimization in the pre-injector linac. In this chapter, the design and optimization of the CLIC injector linac will be presented in detail.

6.1. Beam Dynamics of the CLIC Injector Linac

The positron distribution obtained from PARMELA of the optimized pre-injector linac has been used at the entrance of the injector linac for the simulations. Since the beam is now fully relativistic we use MAD-X [29] for the lattice design. We use the same accelerating structure as in the pre-injector linac with a length of 1.5 m, a gradient of 15 MV/m and an iris radius of 20 mm whose parameters are given in table 6.1.

Table 6.1 General parameters of the CLIC injector linac

Parameter	Value
Frequency [GHz]	2
Maximum accelerating gradient [MV/m]	15
Number of accelerating structure	118
Length of accelerating structure (30 cells) [m]	1.5
Energy gain [MeV]	22.5
Iris radius [mm]	20

It is desired to transport most of the particles through the accelerator, therefore we want the 3σ beam size not to exceed the iris aperture: $R_{iris} \geq 3 \times \sigma_{x,y}$. The normalized emittance ($\gamma\varepsilon_{x/y}$) at the exit of the pre-injector linac is 9.6×10^{-3} m.rad and the mean energy of the beam is 200 MeV. Using equation (6.1) we determine that the maximum beta function should be smaller than 1.8 m for an iris aperture (R_{iris}) of 20 mm at the beginning of the injector linac.

$$\beta_{max} \leq \frac{R_{iris}^2}{9}\frac{\gamma}{\varepsilon_{x,y(norm)}} \qquad (6.1)$$

Here, β_{max} is the largest value of the betatron function along the first accelerating structure and γ is the Lorentz factor corresponding the minimum energy of that sector and $\varepsilon_{x,y(norm)}$ is the normalized emittance. The injector linac needs therefore strong focusing at the entrance. For a FODO lattice the minimum beta-function depends on the strength of the quadrupoles and on the spacing between them. A phase advance of 90° is used for the design since for round beams we obtain the smallest maximum beta-function within the FODO cell [30]. For practical reasons, we limited the maximum field of the quadrupoles to 1.2 T and choose a quadrupole aperture R_Q of 0.1m. This choice of parameters allows us to use quite standard quadrupoles with an aperture large enough to go over a 2 GHz accelerating structure at the beginning of the injector linac.

In the design of the injector linac, as a starting point Twiss parameters are calculated for positrons coming from the exit of pre-injector linac. The beam parameters are given in table 6.2 and this parameters are used at the entrance of the injector linac (the detailed calculation can be found in appendix 6). At the entrance of the injector linac a matching section is necessary in order to inject the positron beam into the injector linac with a beta value of less than 1.8 m. To define the first section of the injector linac, the maximum beta-function and the drift space between quadrupoles in a FODO cell with a phase advance of 90° are calculated and scanned for different values of the distance between quadrupoles in Fig.6.1. A drift space of 15 cm between quadrupoles has been chosen for the first FODO section of the injector linac in case the betatron value, which is calculated by equation (6.1) at its entrance, is smaller than 1.8 m.

Table 6.2 Twiss parameters at the entrance of the injector linac.

Parameter	Value
β_x [m]	2.6090
β_y[m]	2.6457
α_x	-0.9030
α_y	-0.9299

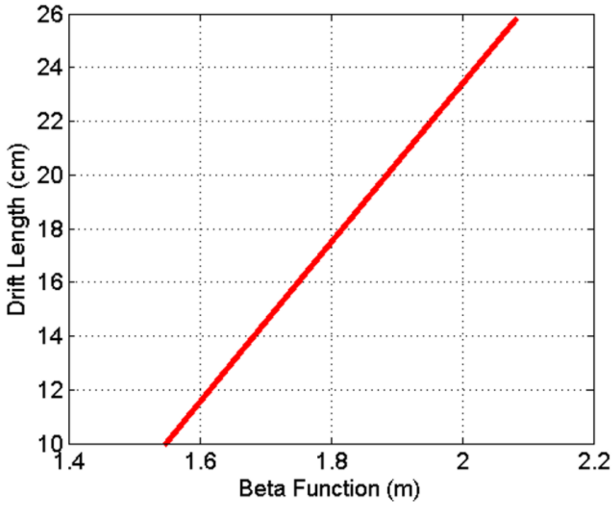

Figure 6.1 Parameter optimizations in a FODO for the entrance of the injector linac.
Betatron function values are scanned versus drift length between the quadrupoles.

Figure 6.1 shows possible betatron values in a FODO. Here, the drift length between quadrupoles in a FODO with a constant phase advance at 90° has been scanned for different quadrupole strength values (the detail information can be found for the calculation in Appendix 6).

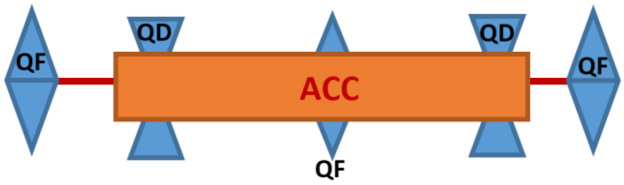

Figure 6.2 Schematic layout of accelerating structure of the first section in the CLIC injector linac.
QF: focusing quadrupole, QD: defocusing quadrupole and ACC: accelerating structure

The first section of the injector linac has been designed as seen in Fig. 6.2. Two FODO cells (2.2 m) contains one TW structure with a length of 1.5 m and the length of the quadrupole is 0.4 m in the first section of the injector linac. The quadrupole strength K is ± 9.0 m^{-2} (+ for focusing and – for defocusing) and we obtain $\beta_x = 1.716$ m, $\beta_y = 0.346$ m in the focusing quadrupoles ($\alpha_x = \alpha_y = 0$) whose parameters are summarized in table 6.3. The betatron functions of a FODO cell is shown for the first section in figure 6.3.

Table 6.3 Parameters of the first FODO section in the CLIC injector linac.

Q_{length} (m)	K (m^{-2})	β_{max} (m)	$Cell_{length}$ (m)	E_{ini} (GeV)	E_{out} (GeV)	TW_{number}
0.4	9.00	1.7160	1.10	0.2065	0.3865	8

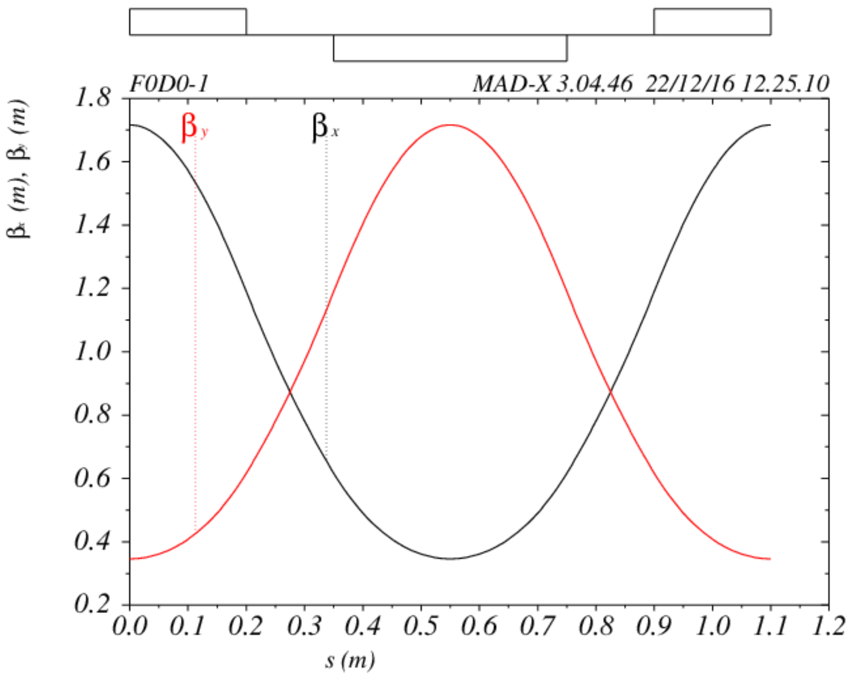

Figure 6.3 Betatron functions in a FODO cell of the first section

In the first and second sections of the injector linac, the minimum quadrupole radius should be bigger than 10 cm due to the outer radius of rf structure.

$$K_Q[m^{-2}] = 0.2998\frac{B[T]/R_Q[m]}{E_{out}^{i}[GeV]} \Rightarrow R_Q[m] \leq \frac{0.36}{K_Q E_{out}^{i}} \tag{6.2}$$

Where, K_Q is a focusing strength of quadrupole, R_Q is the quadrupole radius and E_{out}^{i} is the beam energy at the exit of the accelerating structure i on which the quadrupole is placed. In equation (6.2), the highest energy limitation is given with respect to the radius of the quadrupoles and it is specified the number of the accelerating structure in the first section. As a result, the output energy of the beam should be smaller than 400 MeV and this allows a maximum of 8 accelerating structure to use in the first section as given in table 6.3.

Table 6.4 The allowed quadrupole radius at the exit of each accelerating structure in the first section

Structure Number	Allowed R_Q (cm)	Structure Number	Allowed R_Q (cm)
1	17.977	5	12.800
2	16.326	6	11.940
3	14.953	7	11.188
4	13.793	8	10.526

Totally, eight accelerating structures have been used in the first section since the permitted quadrupole radius should be bigger than 10 cm along the accelerating structures. As seen in table 6.4, the maximum radius of the last quadrupole is 10.526 cm at the last accelerator structure. It does not allow to use more accelerating structures together with quadrupoles. Therefore, a larger beta function should be used in other structures.

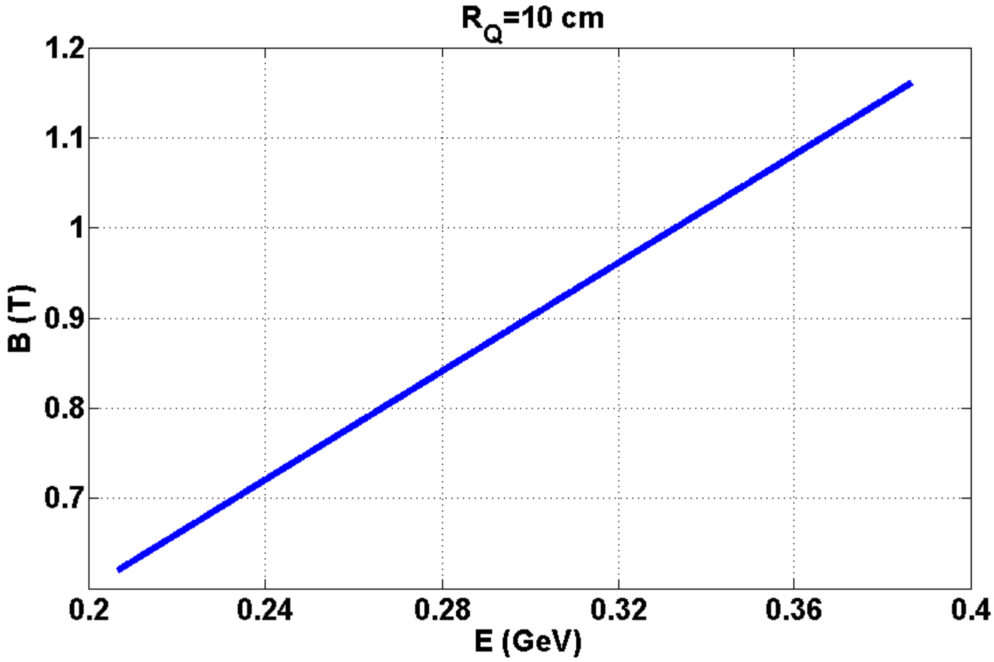

Figure 6.4 The magnetic field of quadrupoles for a constant quadrupole radius of 10 cm along the acceleration of the first section

Figure 6.4 shows the magnetic field of the quadrupoles along the first FODO section for the fixed radius at 10 cm (see equation (6.2)). The magnetic field at the quadrupoles is lower than 1.2 T limit along the first section of the injector linac. This limit is only relevant for the first FODO sector when we reaches 1.16 T maximum for the last quadrupole used at the exit of the last accelerating structure. In case this turns out to be a problem with respect to the saturation limit, the length of the quadrupole could be slightly changed.

To define the second section of the injector linac, the maximum beta values is calculated by equation 6.1. It is assumed that the normalized emittance is ($\gamma\varepsilon_{x/y}$) is constant as 9.6×10^{-3} m.rad along the beam line and γ is the Lorentz factor corresponding the minimum energy of that sector. It is calculated that the maximum beta value is 3.386 m for an initial energy of 386.5 MeV and an iris aperture of 20 mm. The phase advance of FODO is 90° and the length of the quadrupole is 0.4 m. Corresponding drift space between quadrupoles in a FODO is 64 cm at the second FODO section.

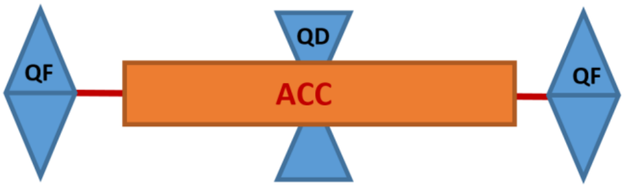

Fig. 6.5 Schematic layout of a FODO for the second section of the CLIC injector linac

The second section of the injector linac has been designed as seen in Fig. 6.5 and it shows a FODO lattice (2.08 m) containing one TW structure with a length of 1.5 m. The focusing strength is 3.95 m^{-2} and it is obtained $\beta_x = 3.386$ m, $\beta_y = 0.635$ m in the focusing quadrupoles ($\alpha_x = \alpha_y = 0$) for the second FODO section as given in table 6.5. The betatron functions of a FODO cell is shown for the second section in Fig.6.6.

Table 6.5 Parameters of the second FODO section in the CLIC injector linac.

Q_{length} (m)	K (m^{-2})	β_{max} (m)	$Cell_{length}$ (m)	E_{ini} (GeV)	E_{out} (GeV)	TW_{number}
0.4	3.95	3.386	2.08	0.3865	0.7915	18

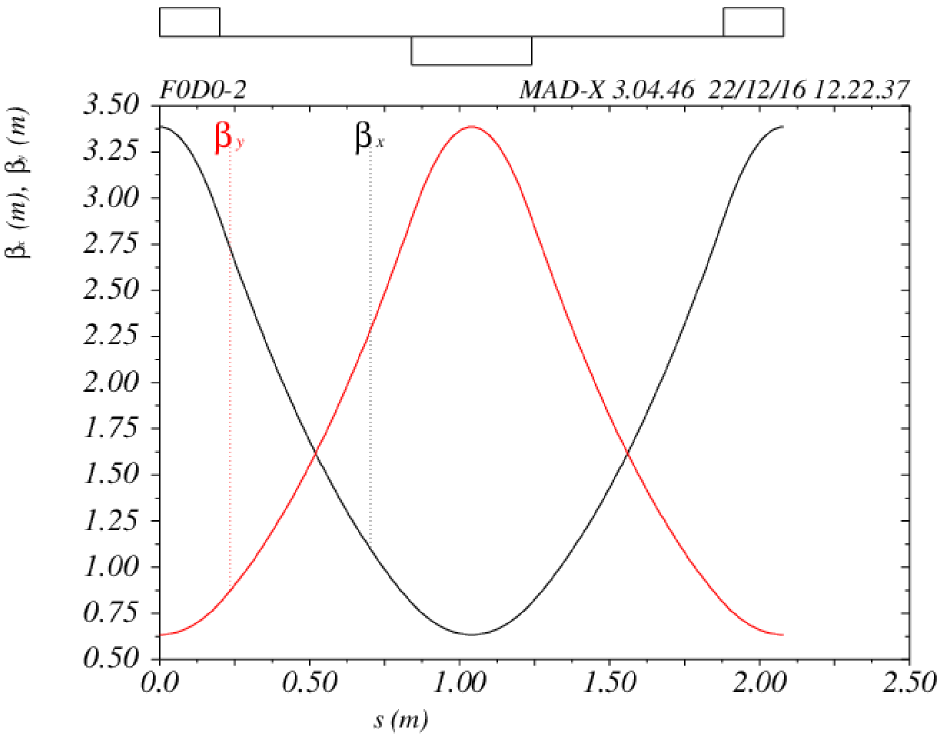

Figure 6.6 Betatron functions in a FODO cell of the second section

After making similar calculations with respect to maximum quadrupole radius for the second section, it is noticed that a shorter beam line can be used in the second section. Although, the highest limitation is 911 MeV in the output energy (see equation 6.2), the second section could be finished by using less quadrupole. Therefore, an output energy of 791.5 MeV has been chosen for the second section. Totally, 18 accelerating structures are used and considering the last accelerating structure, the maximum radius of the quadrupoles surrounding RF structures is 11.610 cm as seen in table 6.6.

Table 6.6. The allowed quadrupole radius at the exit of each accelerating structure in the second section

Structure Number	Maximum R_Q (cm)	Structure Number	Maximum R_Q (cm)	Structure Number	Maximum R_Q (cm)
1	22.643	7	16.956	13	13.552
2	21.444	8	16.274	14	13.113
3	20.366	9	15.274	15	12.702
4	19.391	10	15.064	16	13.316
5	18.505	11	14.524	17	11.952
6	17.696	12	14.021	18	11.610

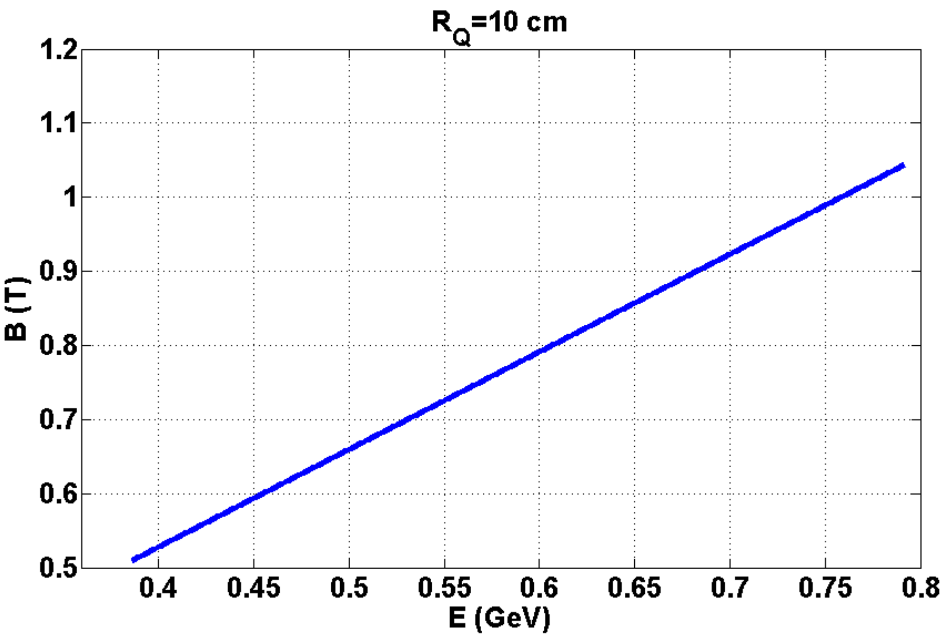

Figure 6.7 The magnetic field of quadrupoles for a constant quadrupole radius of 10 cm along the acceleration of the second section

Figure 6.7 describes the magnetic field of the quadrupoles along the second FODO section by the acceleration. It is shown that the magnetic field of all quadrupoles remains below the saturation limit of 1.2 T.

In the first and second sections there are two limitation which are the iris aperture and the quadrupole aperture. In the third section, there is only the iris aperture limitation. To define the third section of the injector linac, betatron function is scanned for different quadrupole strengths in a FODO lattice with a phase advance of 90° as seen in figure 6.8. The drift space between quadrupoles is obtained by calculating how to put two TW structures in a FODO with the appropriate betatron function. A drift space of 165 cm between quadrupoles in a FODO lattice has been chosen.

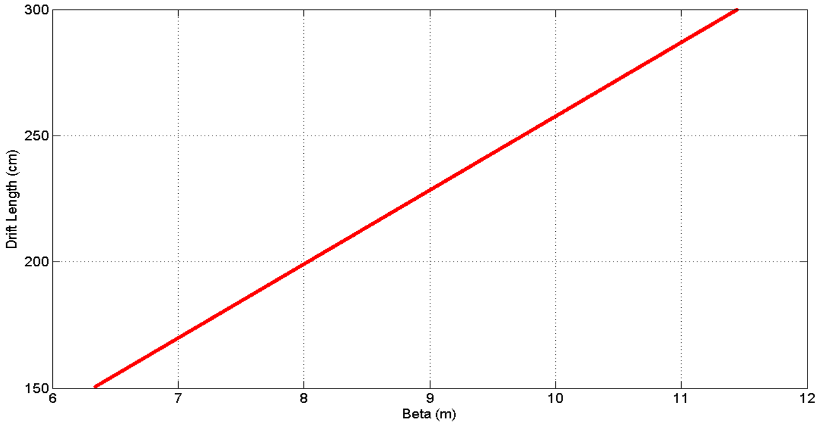

Figure 6.8 Parameter optimizations in a FODO for the third section in the injector linac.
Betatron function values are scanned versus drift length between the quadrupoles

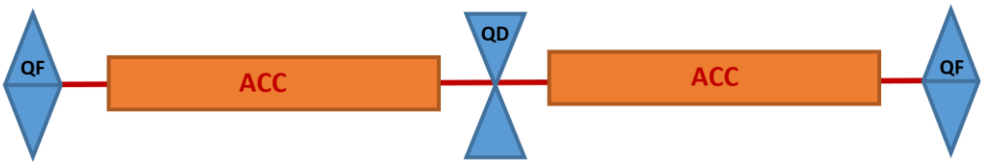

Fig. 6.9 Schematic layout of a FODO for the third section in the CLIC injector linac

In the third section of the injector linac, a FODO lattice (4.1 m) consists of two TW structure with a length of 1.5 m in Fig.6.9. Totally, 28 accelerating structures are used up to an energy of 1.4215 GeV as given in table 6.7. We obtain K_Q = 1.85 m^{-2}, β_x =

6.835 m, β_y = 1.228 m ($\alpha_x = \alpha_y = 0$) in the focusing quadrupoles. The betatron functions of a FODO cell is shown for the third section in Fig.6.10.

Table 6.7 Parameters of the third FODO section in the CLIC injector linac.

Q_{length} (m)	K (m^{-2})	β_{max} (m)	$Cell_{length}$ (m)	E_{ini} (GeV)	E_{out} (GeV)	TW_{number}
0.4	1.85	6.835	4.10	0.7915	1.4215	28

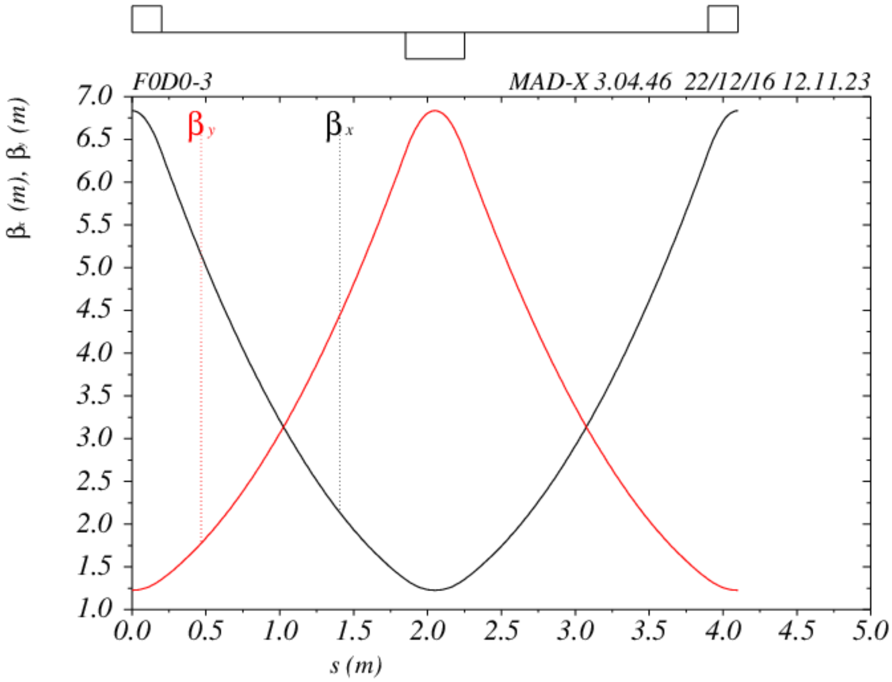

Figure 6.10 Betatron functions in a FODO cell of the third section

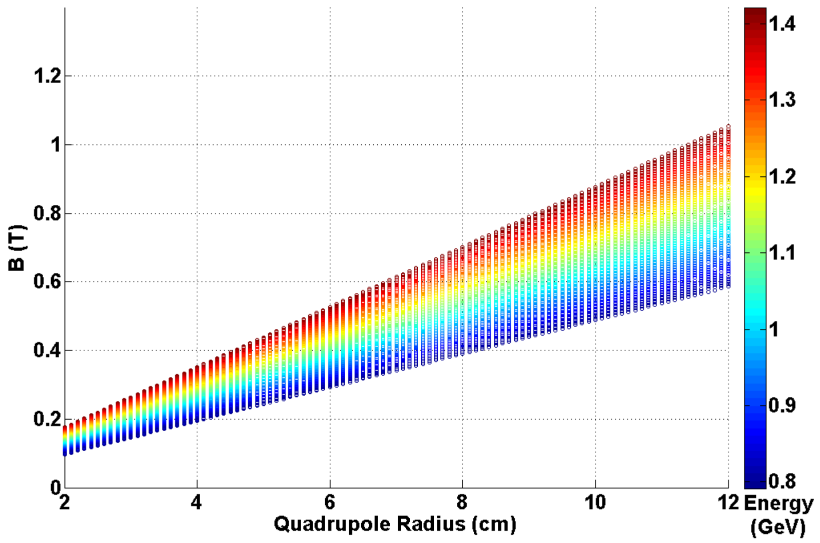

Figure 6.11 Quadrupole magnetic field for the different quadrupole radius along the acceleration of the third section

Using larger betatron function provides lower magnetic field in the quadrupoles along the third section of the injector linac. The magnetic field of quadrupoles is far away from the saturation limit and it can be seen in Fig.6.11. Similar calculation has been done for the fourth and fifth sections of the injector linac in terms of the appropriate drift spaces and the maximum beta values as seen in Fig.6.12.

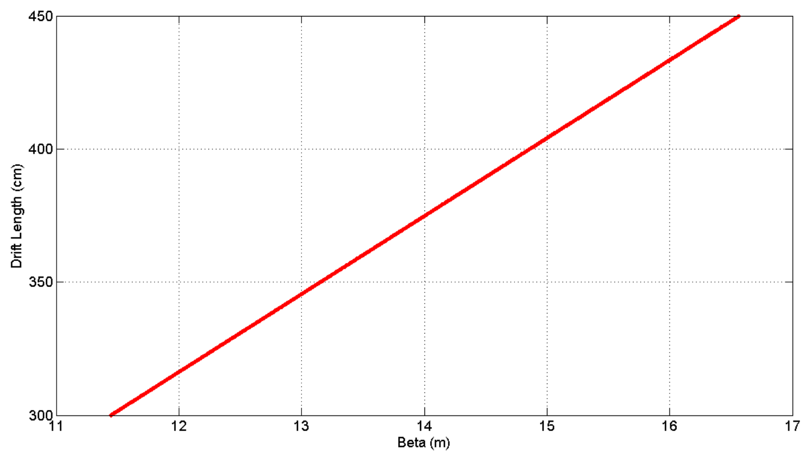

Figure 6.12 Parameter optimizations in a FODO for the fourth section of the injector linac.

Betatron function values are scanned versus drift length between the quadrupoles in a FODO with a phase advance of 90°.

Figure 6.12 shows that four TW structures could be settled with a drift space of 320 cm between quadrupoles in a FODO cell.

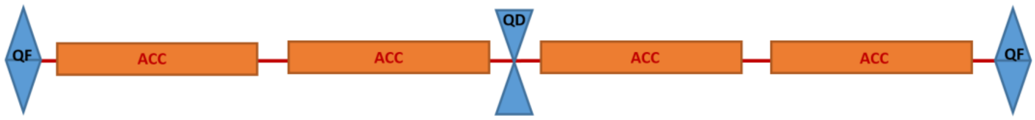

Figure 6.13 Schematic layout of a FODO for the fourth section in the CLIC injector linac

In the fourth section of the injector linac, a FODO lattice contains four TW structure with a length of 1.5 m each as seen in Fig.6.13. The highest energy of the fourth section is 2.0515 GeV and we obtain K_Q = 1.02 m^{-2}, β_x = 12.125 m, β_y = 2.140 m ($\alpha_x = \alpha_y = 0$) in the focusing quadrupoles as given in table 6.8. The betatron functions of a FODO cell is shown for the fourth section in Fig.6.14.

Table 6.8 Parameters of the fourth FODO section in the CLIC injector linac.

Q_{length} (m)	K (m^{-2})	β_{max} (m)	$Cell_{length}$ (m)	E_{ini} (GeV)	E_{out} (GeV)	TW_{number}
0.4	1.02	12.125	7.20	1.4215	2.0515	28

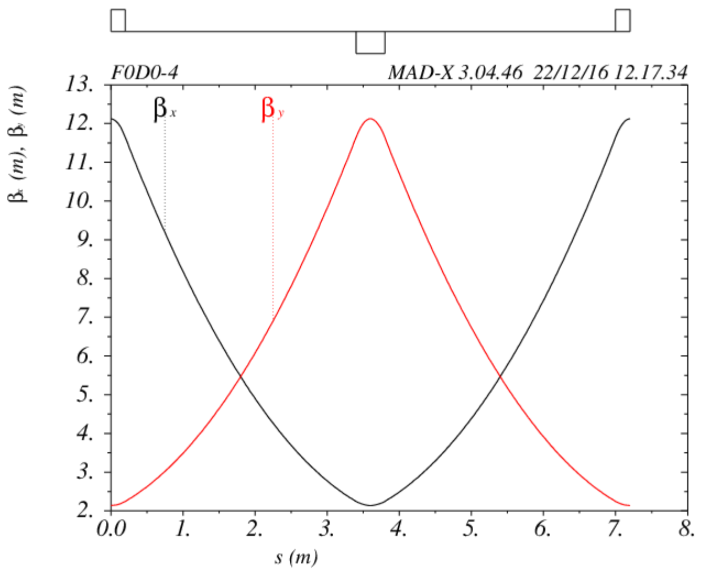

Figure 6.14 Betatron functions in a FODO cell of the fourth section

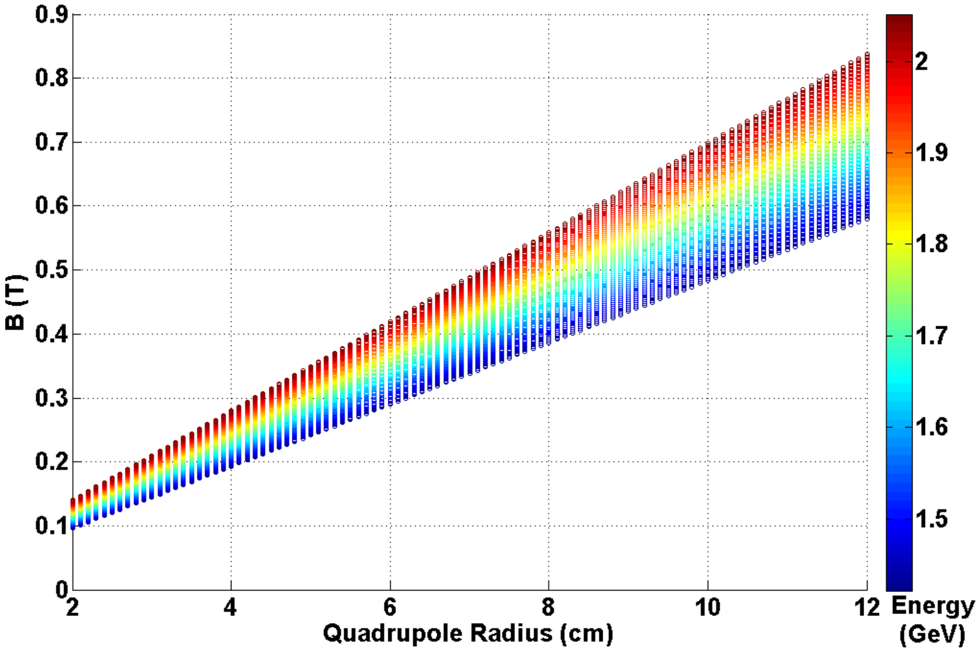

Figure 6.15 Quadrupole magnetic field for the different quadrupole radius along the acceleration of the fourth section

In figure 6.15, it is seen that the magnetic field in the quadrupoles is very low compared to the saturation limit at 1.2 T along the fourth section of the injector linac.

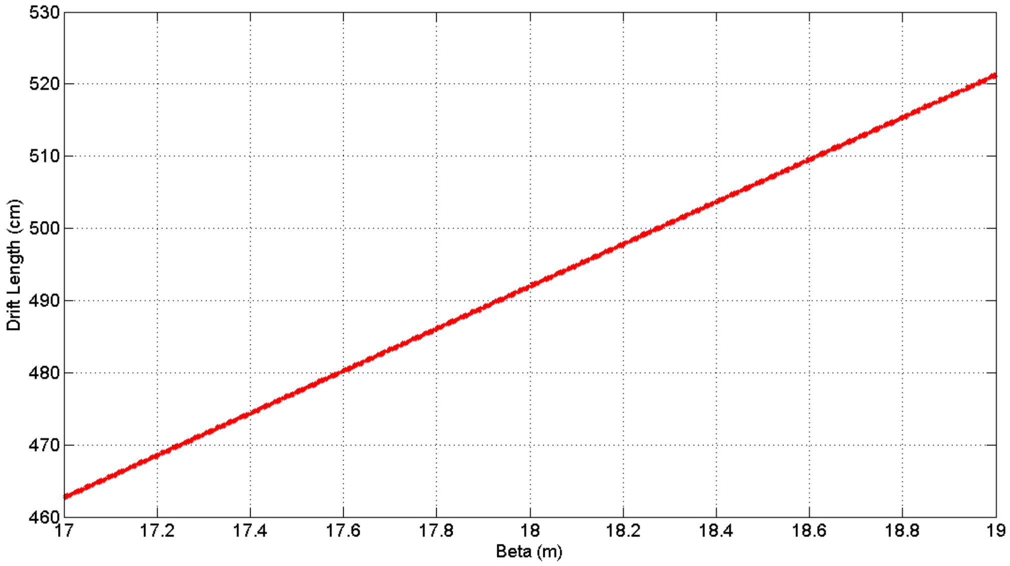

Figure 6.16 Parameter optimizations in a FODO for the fifth section of the injector linac.

Betatron function values are scanned versus drift length between the quadrupoles

To use six TW structures, the drift space between quadrupoles in a FODO has been calculated and scanned versus corresponding betatron function as seen in Fig.6.16. A drift space of 490 cm between each quadrupole has been chosen and the corresponding betatron function is obtained for the fifth section of the injector linac.

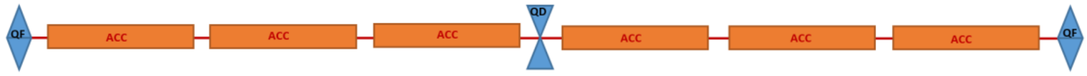

Figure 6.17 Schematic layout of a FODO for the fifth section in the CLIC injector linac

In the fifth section of the injector linac, a FODO lattice consists of six TW structures with a length of 1.5 m each as seen in Fig.6.17. An energy gain of 0.81 GeV is provided and we obtained $K_Q = 0.68$ m^{-2}, $\beta_x = 17.886$ m, $\beta_y = 3.183$ m ($\alpha_x = \alpha_y = 0$) in the focusing quadrupoles for the fifth FODO sector as summarized in table 6.9. The betatron functions of a FODO cell is shown for the fifth section in Fig.6.18.

Table 6.9 Parameters of the fifth FODO section in the CLIC injector linac.

Q_{length} (m)	K (m^{-2})	β_{max} (m)	$Cell_{length}$ (m)	E_{ini} (GeV)	E_{out} (GeV)	TW_{number}
0.4	0.68	17.886	10.6	2.0515	2.8615	36

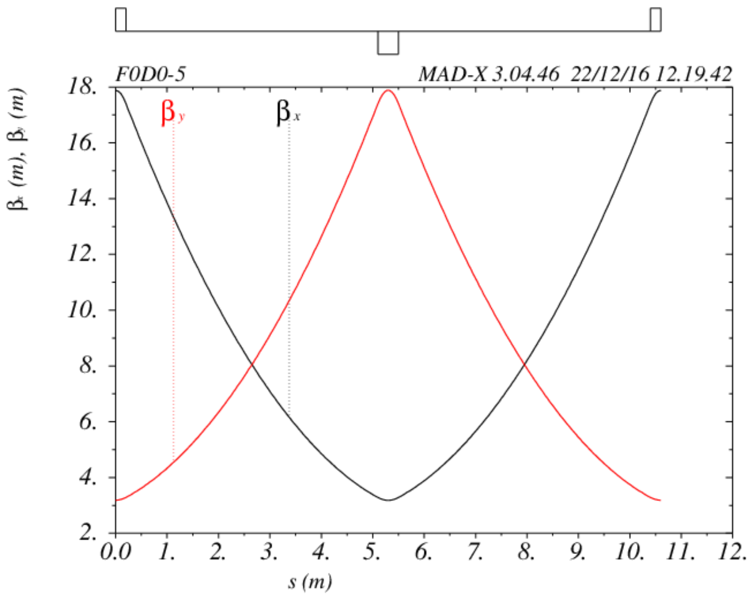

Figure 6.18 Betatron functions in a FODO cell of the fifth section

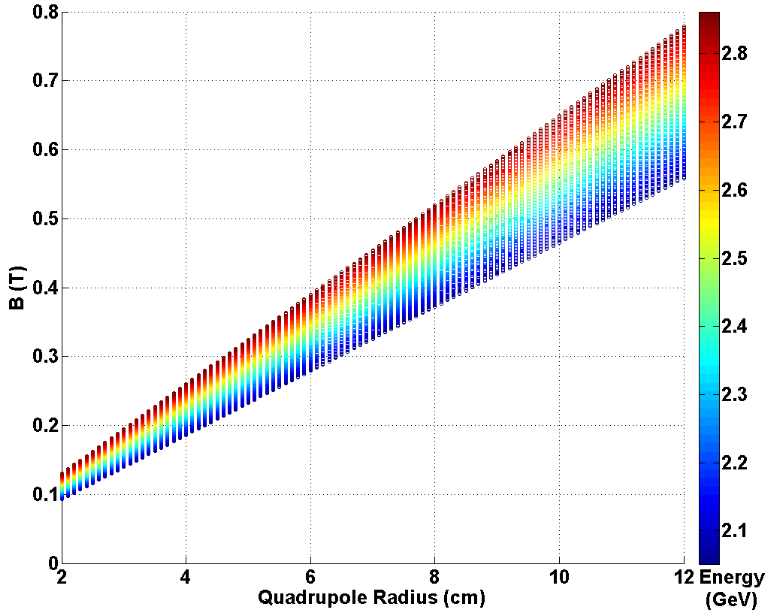

Figure 6.19 Quadrupole magnetic field for the different quadrupole radius along the acceleration of the fifth section

Figure 6.19 describes the magnetic field of the quadrupoles in the fifth FODO section of the injector linac. It is shown that the magnetic field of the quadrupoles is well within the acceptable level during the acceleration in the fifth section of the injector linac.

6.2. Optical Design of the CLIC Injector Linac

The acceleration along the beam line makes it possible to have a larger beta-function due to the reduction of the geometric emittance. The design profits from that by increasing the distance between quadrupoles. From the third section on quadrupoles can be placed in between accelerating structures allowing in principle for smaller aperture magnets. Using several sections allows to reduce the number of the quadrupoles needed without compromising on the beam transport. The parameters of all section can be found in table 6.10.

Table 6.10 Parameters of the five different sections in the FODO lattice along the CLIC injector linac.

Sections	Q_{length} (m)	K (m^{-2})	β_{max} (m)	$Cell_{length}$ (m)	E_{ini} (GeV)	E_{out} (GeV)	$Q_{numbers}$
1	0.4	9.00	1.7160	1.10	0.2065	0.3865	33
2	0.4	3.95	3.3860	2.08	0.3865	0.7915	37
3	0.4	1.85	6.8252	4.10	0.7915	1.4215	29
4	0.4	1.02	12.1250	7.20	1.4215	2.0515	15
5	0.4	0.68	17.8860	10.60	2.0515	2.8615	13

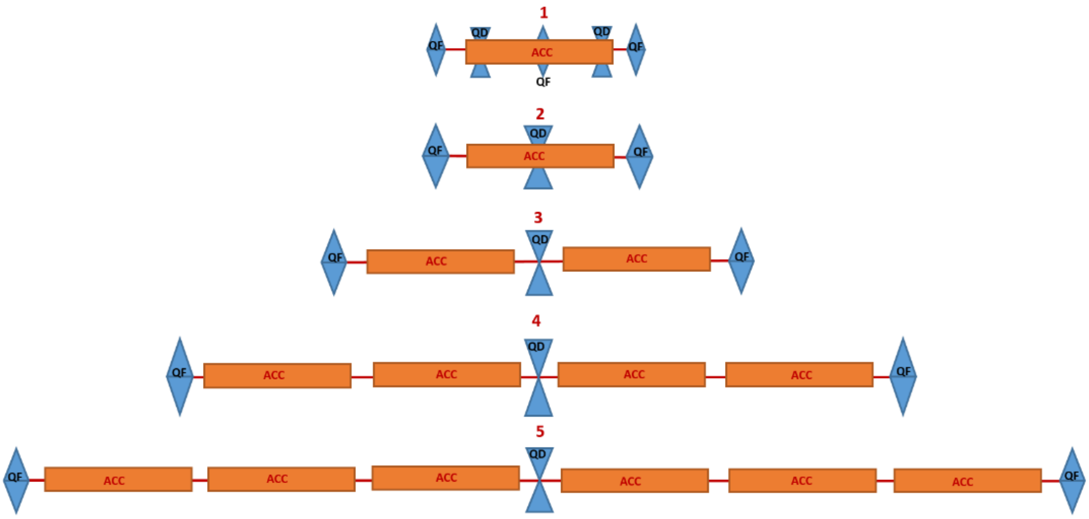

Figure 6.20 Schematic layout of the five different sections in the FODO lattice along the CLIC injector linac.
QF: focusing quadrupoles, QD: defocusing quadrupoles and ACC: accelerating structure

Five different FODO sections have been designed with increasing spacing in-between quadrupoles (see sketch in Fig.6.20). The beta-functions along the linac in the five different sections are shown in Fig.6.21. The MAD-X input file can be found for the injector linac in appendix 7.

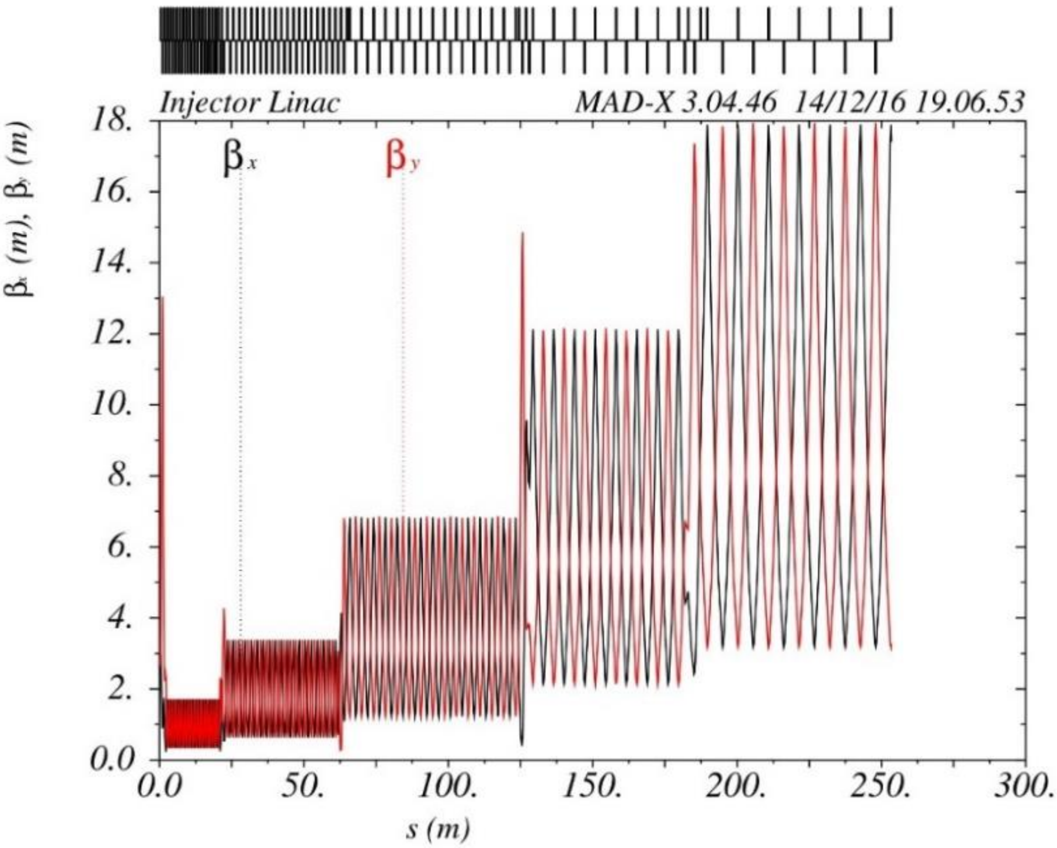

Figure 6.21 Horizontal and vertical beta functions along the CLIC injector linac

A total of 19 quadrupoles are used for matching between the different sections. The simulations for the lattice design have been done initially with MAD-X without considering acceleration to avoid the problem of having quadrupoles at the same place as accelerating structures. For the plot of the beam sizes the increase in energy has been taken into account showing that the aperture of 20 mm can house a 3σ beam and the corresponding beam envelopes in Fig.6.22. This design allows to reduce the number of quadrupoles used to 146 compared to 192 in the CDR.

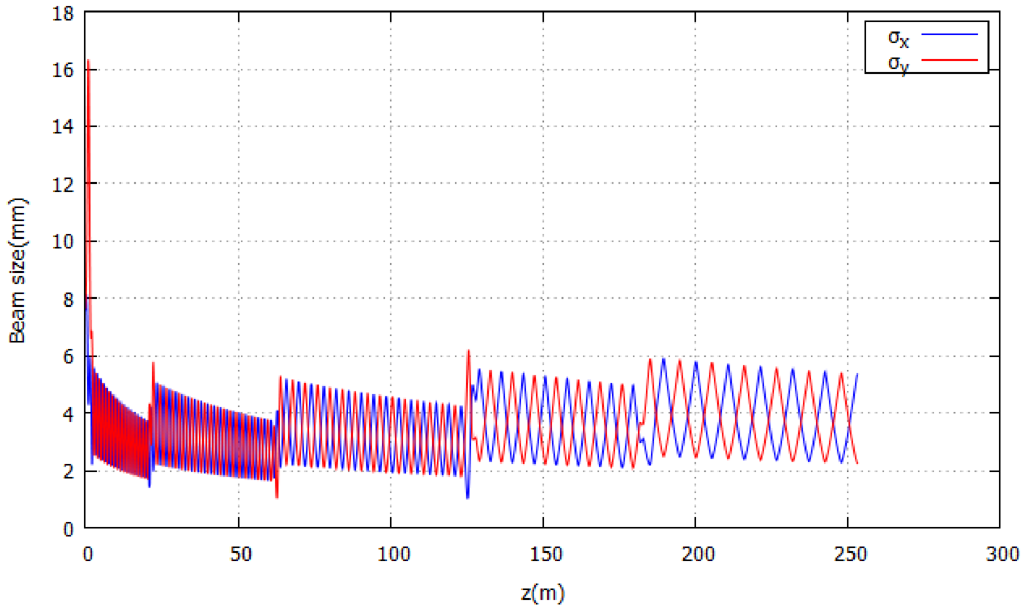

Figure 6.22 Positron beam envelopes along the CLIC injector linac.
Red is sigma-x and blue is sigma-y.

6.3. Tracking Simulation of the CLIC Injector Linac

After finishing the optical design of the CLIC injector linac, tracking simulations have been performed using the particle tracking code PLACET [31, 32]. The definition of the quadrupoles around rf structures as used in the first and second sections is not foreseen in PLACET. Therefore, we have used the following approach: a quadrupole with a length of 0.4 m has been split in 400 zero-length slices (in thin-lens approximation) with a thick rf structures, 1 mm long, in between two consecutive quadrupole kicks to achieve the appropriate acceleration. The detail information can be found in appendix 8.

After verifying the beam line without acceleration, it is shown that the beam line is working very well by thin lens approximation and the betatron functions is compatible along the injector linac compared to MAD-X result as seen in Fig.6.23.

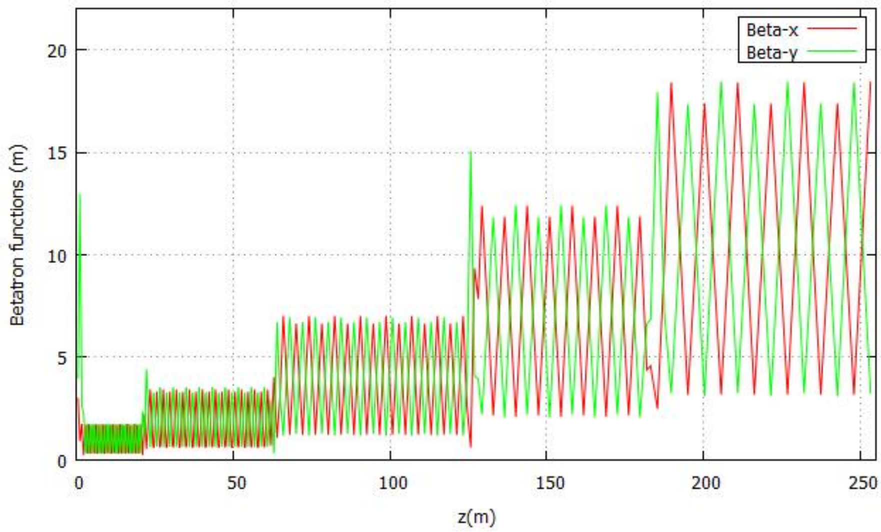

Figure 6.23 Horizontal and vertical beta functions along the injector linac without acceleration

The optical functions were checked with acceleration by PLACET for positrons coming from the pre-injector linac. PLACET calculates the parameters from the particle distribution and take into account the focusing effect of the accelerating structures. The realistic modelling of the overlapping accelerating and focusing fields resulted in a mismatch of the betatron functions compared with respect to the energy-independent MAD-X design (see figure 6.24).

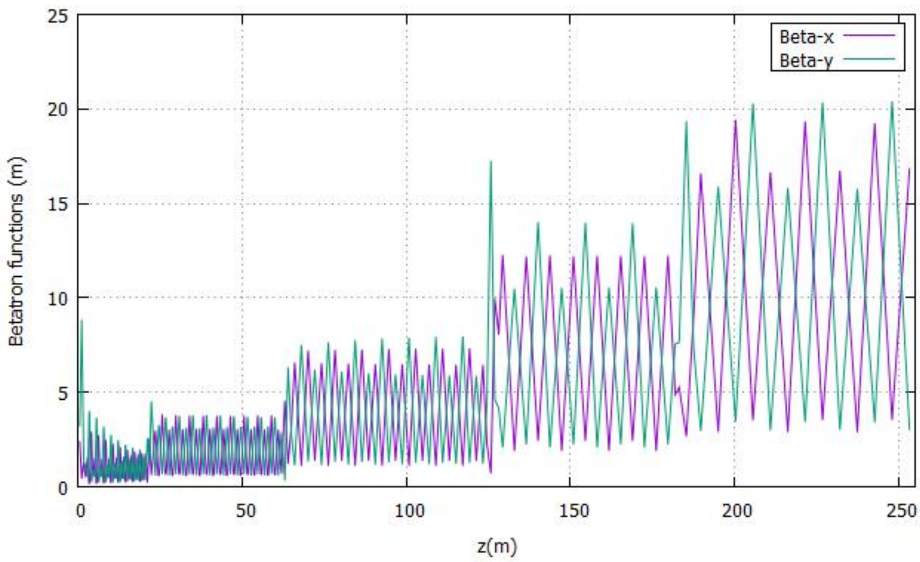

Figure 6.24 Mismatch of Horizontal and vertical beta functions along the injector linac for positrons coming from the pre-injector linac

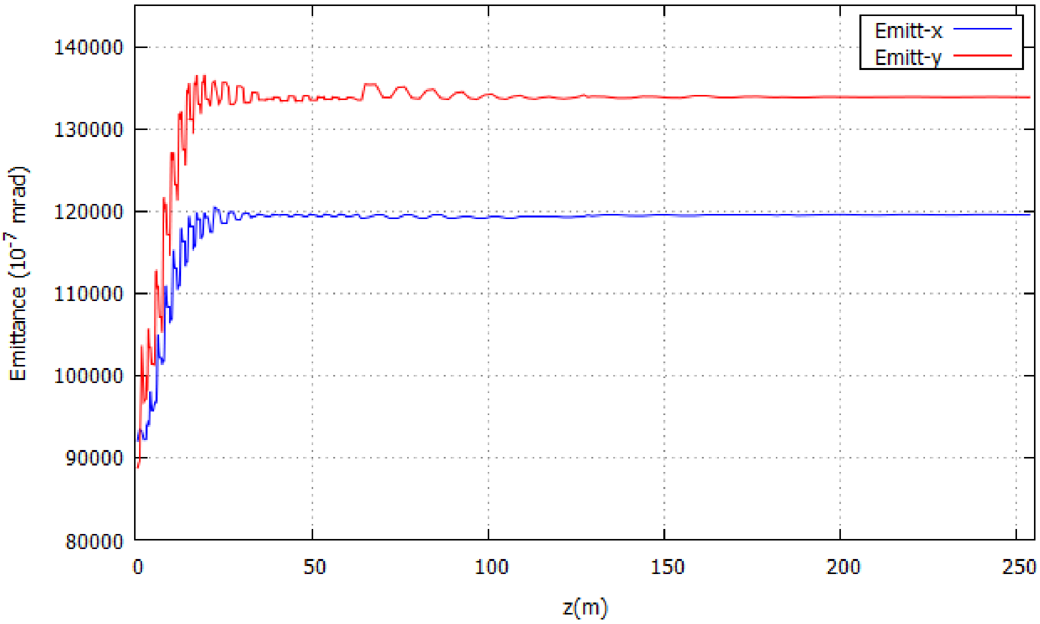

Figure 6.25 Emittance growth along the injector linac for positrons coming from the pre-injector linac

Figure 6.25 shows the emittance evaluated along the beam line. A significant emittance growth due to the very high energy spread of the positron beam, in particular at the beginning of the linac, is visible. This emittance growth depends on the beta-function therefore we get an asymmetry between the vertical and horizontal plane.

In order to investigate the influence of the large energy spread of the positron beam in more detail a simple Gaussian distribution generated in PLACET has been used with different energy spreads. It can be seen that the different values of energy spreads result in increasing emittance growth (see figures 6.26 and 6.27).

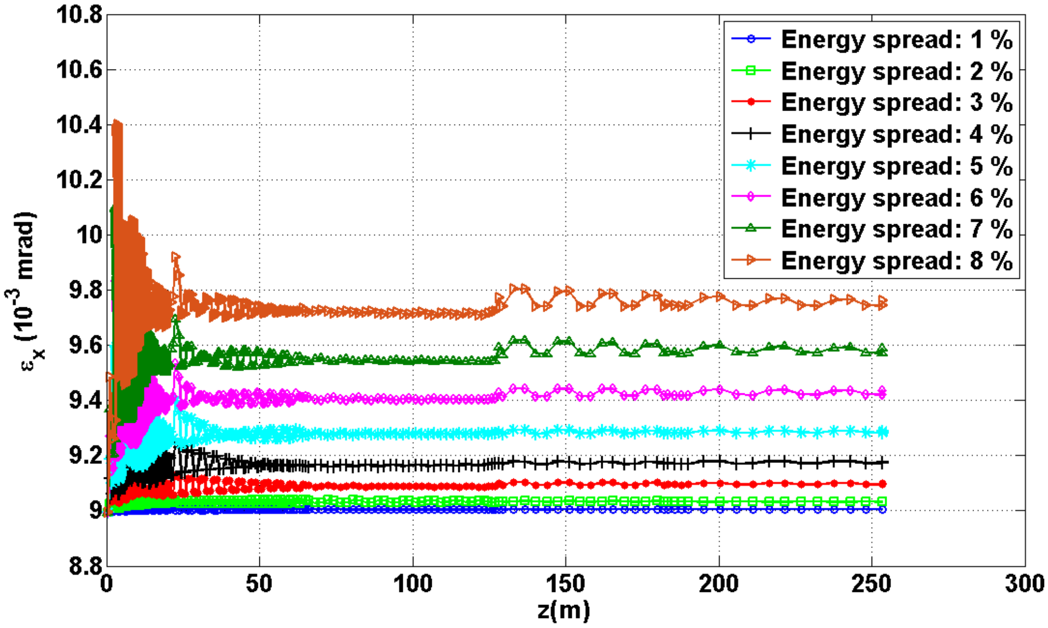

Figure 6.26 Emittance growth by different energy spread for random (Gaussian) particle distribution in the horizontal plane along the CLIC injector linac

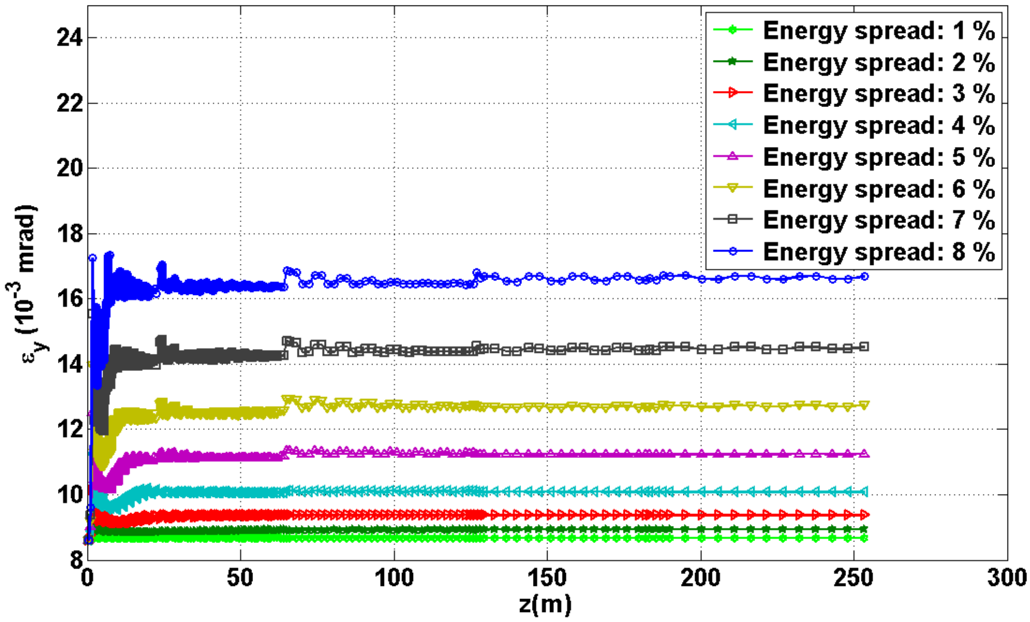

Figure 6.27 Emittance growth by different energy spread for random (Gaussian) particle distribution in the vertical plane along the CLIC injector linac

To improve the emittance growth, we have rematched the strength and position of the quadrupoles in the first matching section by using our positron distribution in

PLACET. During the matching process, we have considered the limitation of magnetic field in quadrupoles and the magnetic field is lower than 1.2 T as seen in table 6.11.

Table 6.11 Parameters of the first matching section for MAD-X and PLACET

MAD-X				PLACET			
Q_{number}	Q_{length} (m)	K (m^{-2})	g (T/m)	Q_{number}	Q_{length} (m)	K (m^{-2})	g (T/m)
1	0.4	3.61809	2.49211	1	0.4	2.95750	2.03710
2	0.4	-5.80276	3.99689	2	0.4	-5.14322	3.54261
3	0.4	6.84839	4.71712	3	0.4	6.71900	4.62800
4	0.4	-4.59264	3.16337	4	0.4	-5.77384	3.97698
Drift number	Drift length (m)			Drift number	Drift length (m)		
1	0.2			1	0.24871		
2	0.2			2	0.19257		
3	0.2			3	0.22427		
4	0.2			4	0.21804		
5	0.2			5	0.15327		
The first matching line: D1-Q1- D2-Q2-D3-Q3-D4-Q4-D5							

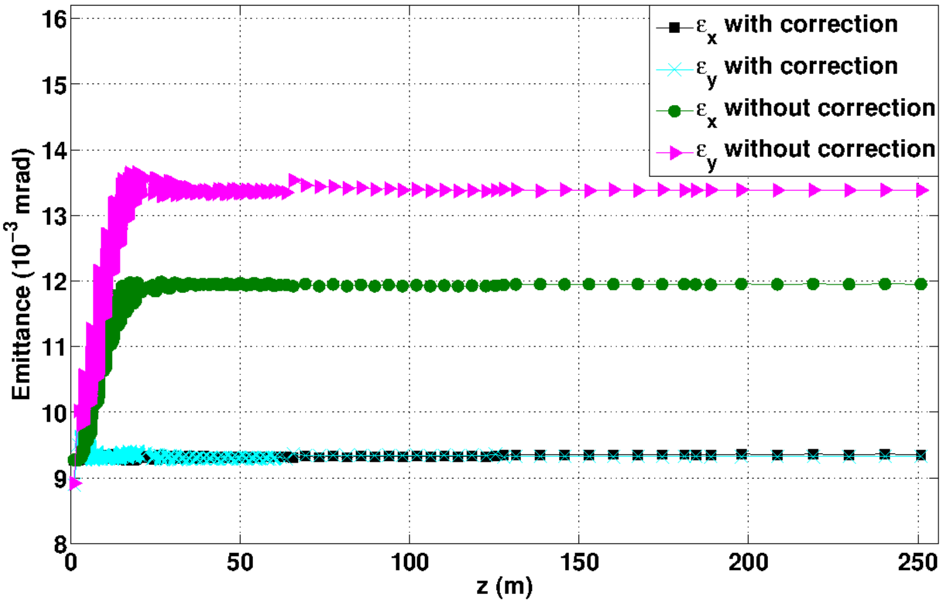

Figure 6.28 Emittance growth along the CLIC injector linac

PLACET allowed us to optimize the emittance growth by slightly varying the quadrupole strength along the linac. The emittance growth can be mitigated by this optimisation adapting mainly the quadrupole strength in the first matching section (see Fig.6.28). Corresponding betatron functions and beam envelopes can be seen in Fig.6.29 and Fig.6.30.

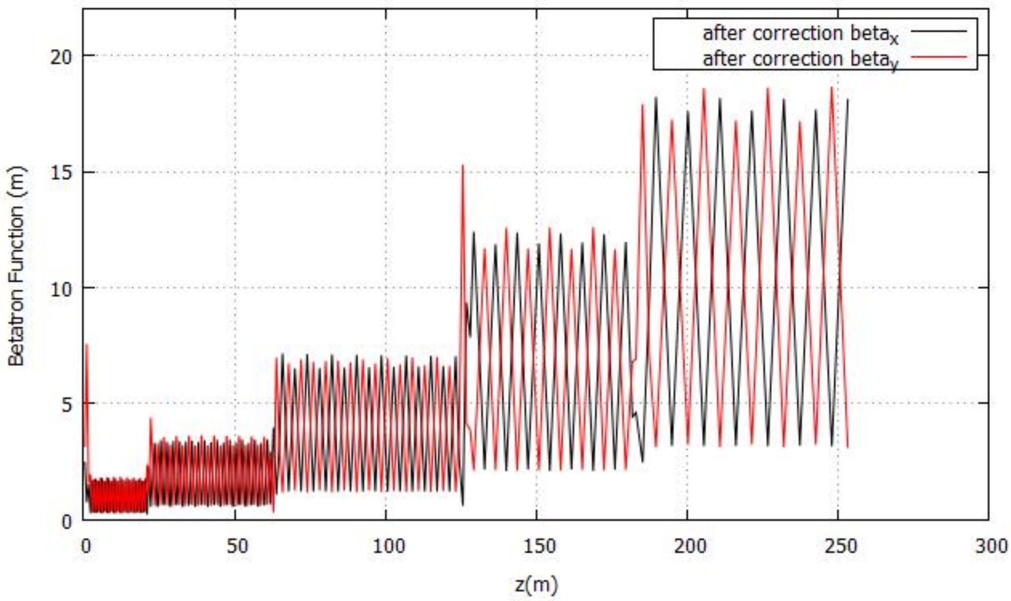

Fig. 6.29 Corrected horizontal and vertical beta functions along the CLIC injector linac

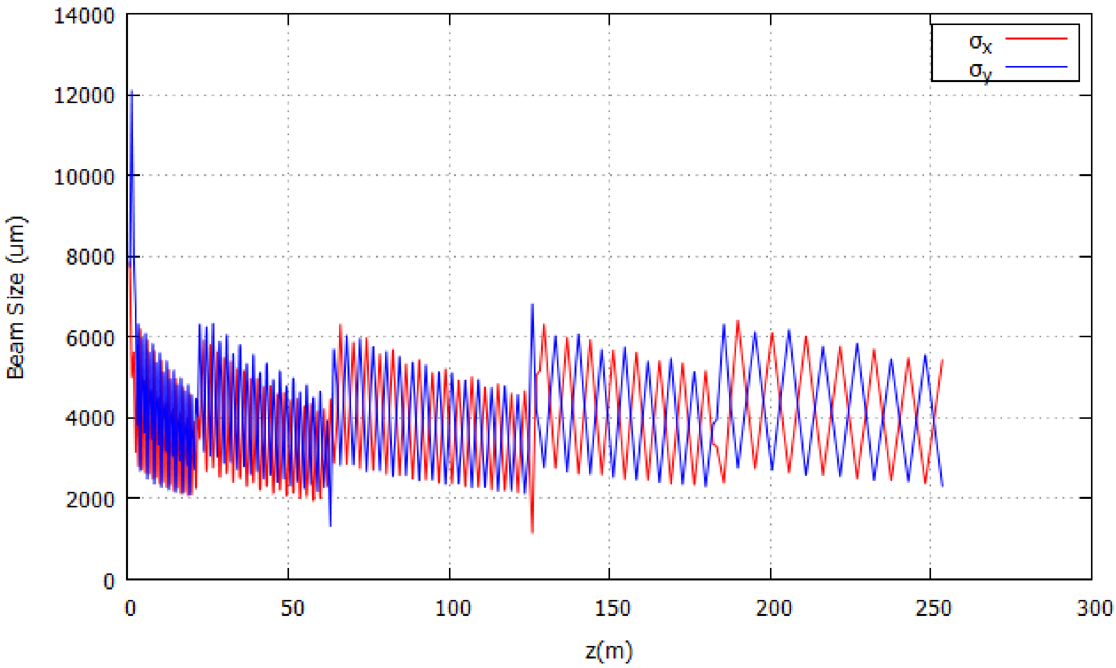

Fig. 6.30 Corrected positron beam horizontal and vertical envelopes along the CLIC injector linac

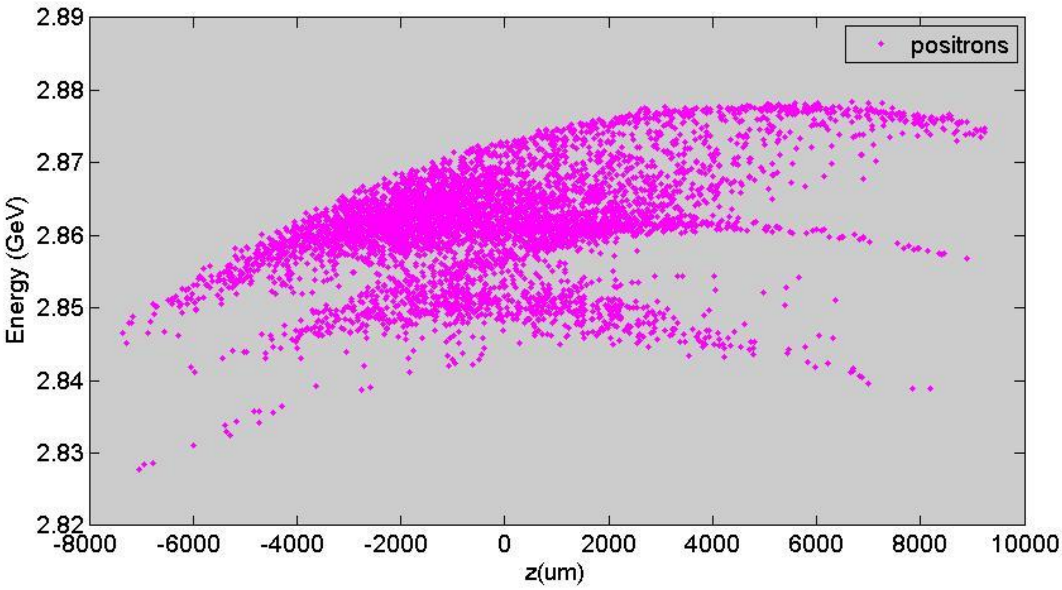

Figure 6.31 Longitudinal phase space at the exit of the CLIC injector linac.

After correction of the emittance growth, Figure 6.31 shows the phase space obtained for the positrons at the exit of the beam line. The important result is that the positron yield amounts to 0.97 e^+/e^- about a factor 2.5 higher than the 0.39 e^+/e^- which were previously estimated and published in the CDR. Another important result is that all particles are inside the acceptance window of the pre-damping ring without a need of phase space rotation. To transport basically all the beam without losses through the injector linac, it was necessary to increase the aperture of the beam pipe in the quadrupoles to 4 cm in particular in the first matching section. An aperture of 2 cm all along the beam line would have resulted in a 10 % loss of positrons.

6.4. Beam Offset and Misalignment Errors in the CLIC Injector Linac

The transverse beam offset error for positrons and the misalignment error in the quadrupoles have been investigated in the CLIC injector linac [33]. In the first step, the transverse beam offset has been varied and then the beam was tracked through a perfectly aligned beam line. In the second step, the positrons without any offset are tracked with misaligned quadrupoles along the injector linac. In both cases also, we focus on the emittance evolution along the injector linac.

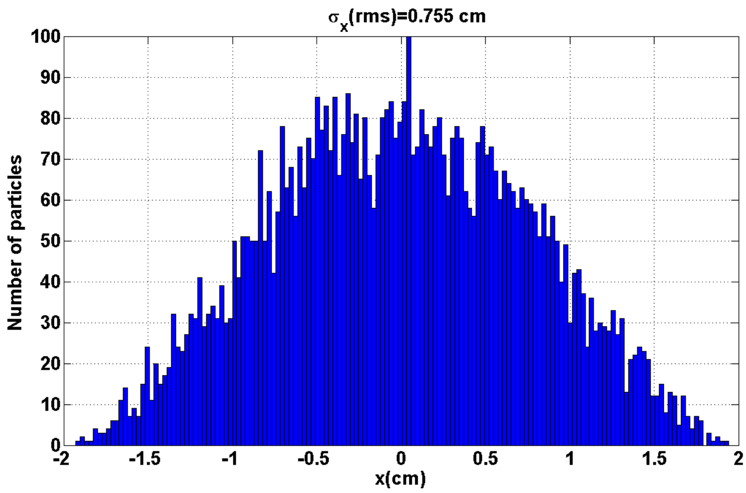

Figure 6.32 Positron distribution in x axis at the entrance of the injector linac.

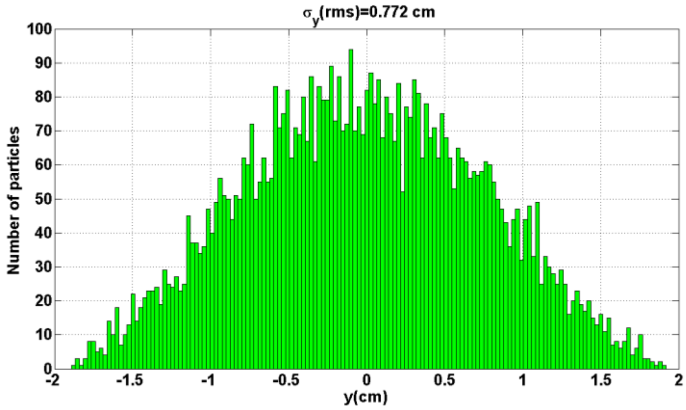

Figure 6.33 Positron distribution in y axis at the entrance of the injector linac.

Before applying the beam offset errors, the transverse positron distribution is checked at the entrance of the injector linac. It is shown that the positron beam size (rms) is bigger than 700 µm at the entrance of the injector linac as seen in Fig.6.32 and Fig.6.33. It is expected that a small offset error could not affect so much the positron beam along the beam line. Therefore, beam offset error are applied for 100 µm, 200 µm and 300 µm in the transverse plane for positrons at the entrance of the injector linac respectively. It is seen that the beam offsets do not affect the emittance growth much for positrons at x and y axis due to the large rms beam size as seen in Fig.6.34 and Fig.6.35.

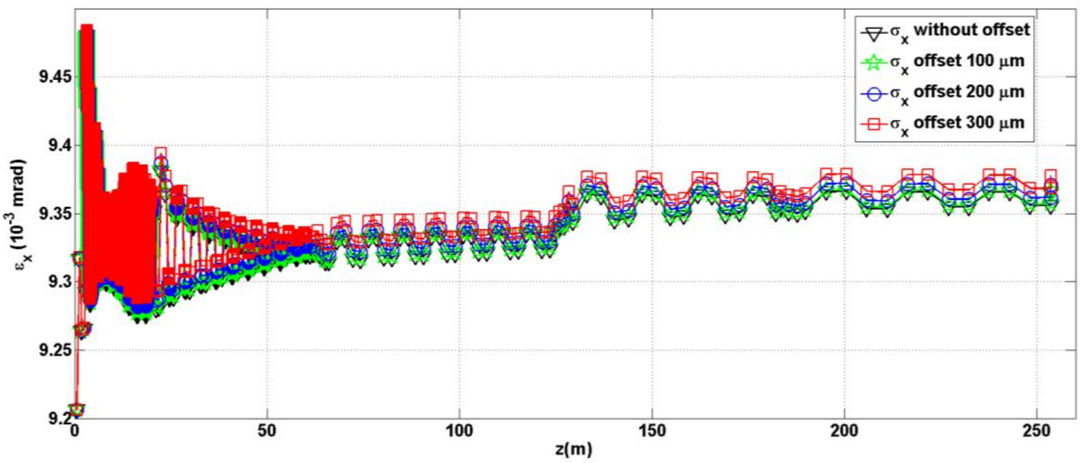

Figure 6.34 The emittance growth for different beam offsets at x axis along the injector linac.

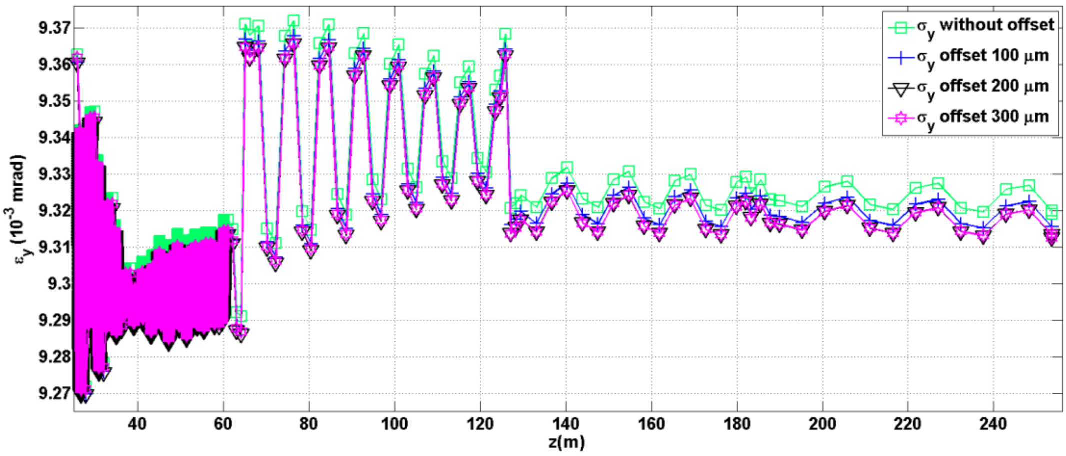

Figure 6.35 The emittance growth for different beam offsets at y axis along the injector linac.

In the second step, misalignment errors of 100 μm, 200 μm and 300 μm are given for each quadrupole randomly and the emittance evolution is checked at the horizontal and vertical planes along the beam line as seen in Fig.6.36 and 6.37.

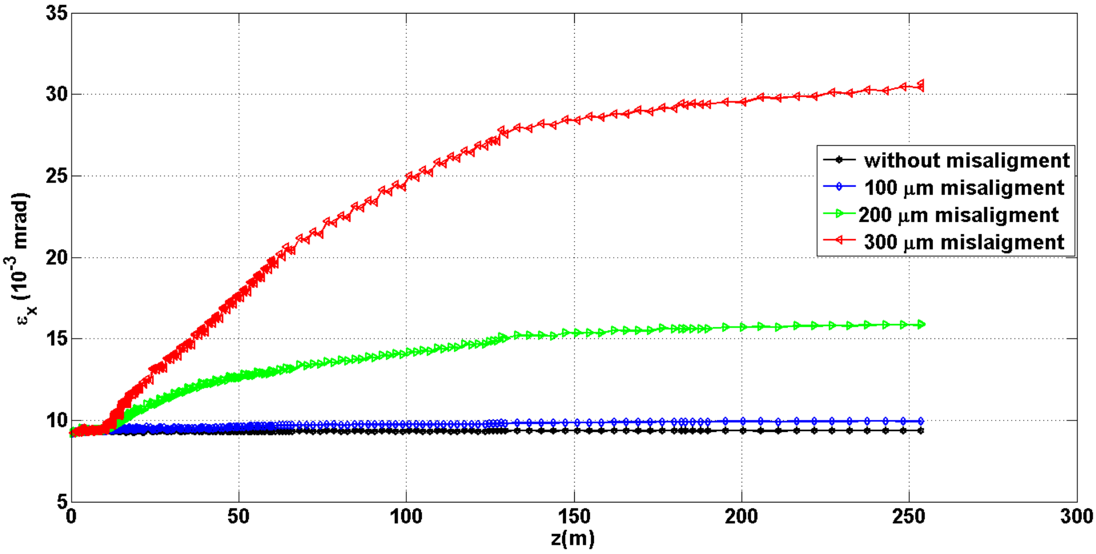

Figure 6.36 The emittance evolutions for different alignment values in quadrupoles along the beam line at the horizontal plane.

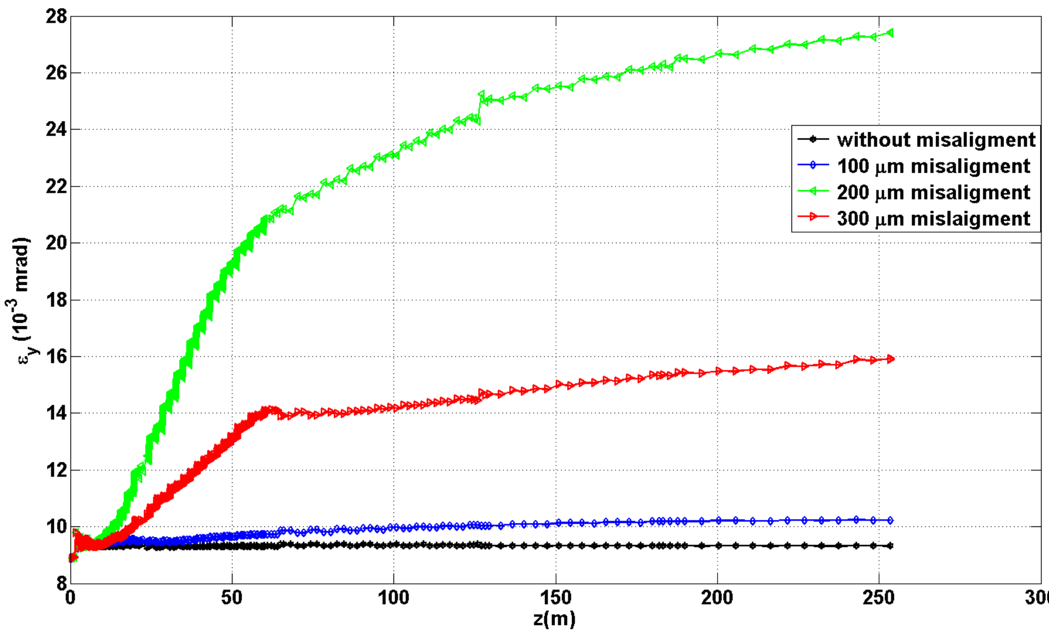

Figure 6.37 The emittance evolutions for different alignment values in quadrupoles along the beam line at the vertical plane.

To correct the emittance growth from the quadrupole misalignments, a one to one correction algorithm can be used assuming each quadrupole has a dedicated corrector magnet and BPM. The here shown simulations assume a BPM resolution of 100 µm. This correction has been applied for misalignment errors of 100 µm, 200 µm and 300 µm in the quadrupoles (see Fig.6.38, Fig.6.39 and Fig.6.40).

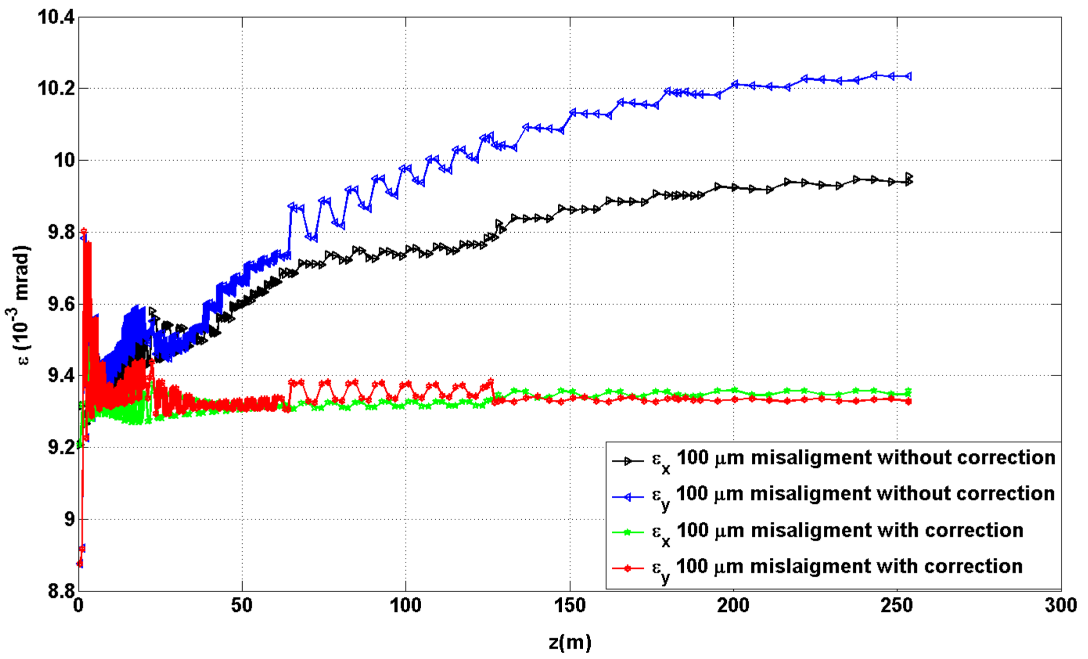

Figure 6.38 Horizontal and vertical emittance growth for positrons by a misalignment of 100 μm in each quadrupole and corrections.

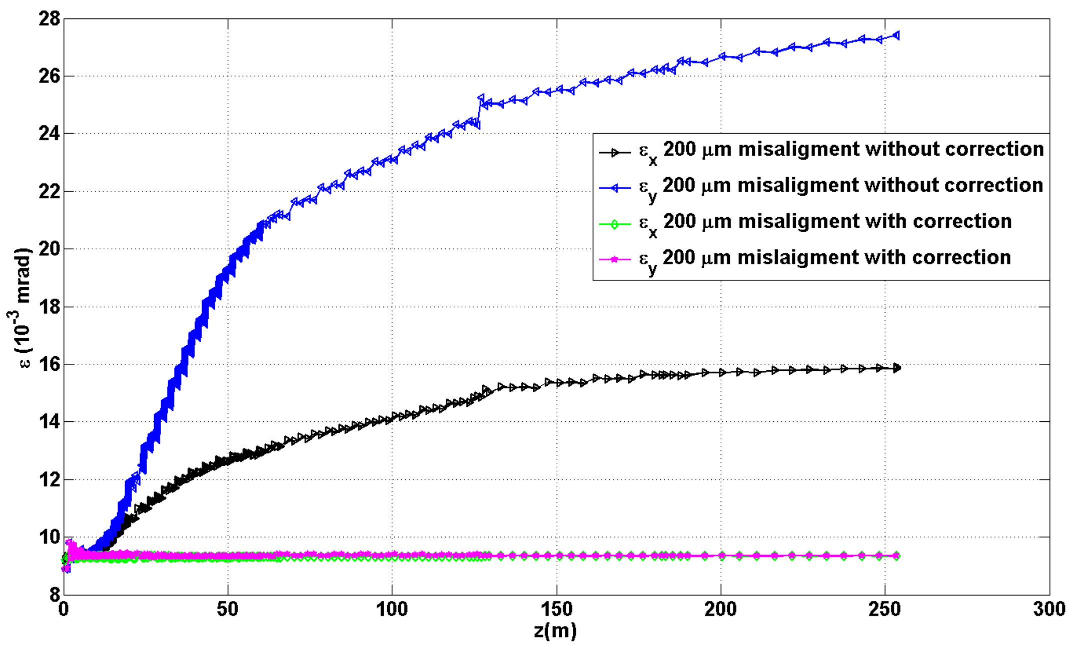

Figure 6.39 Horizontal and vertical emittance growth for positrons by a misalignment of 200 μm in each quadrupole and corrections.

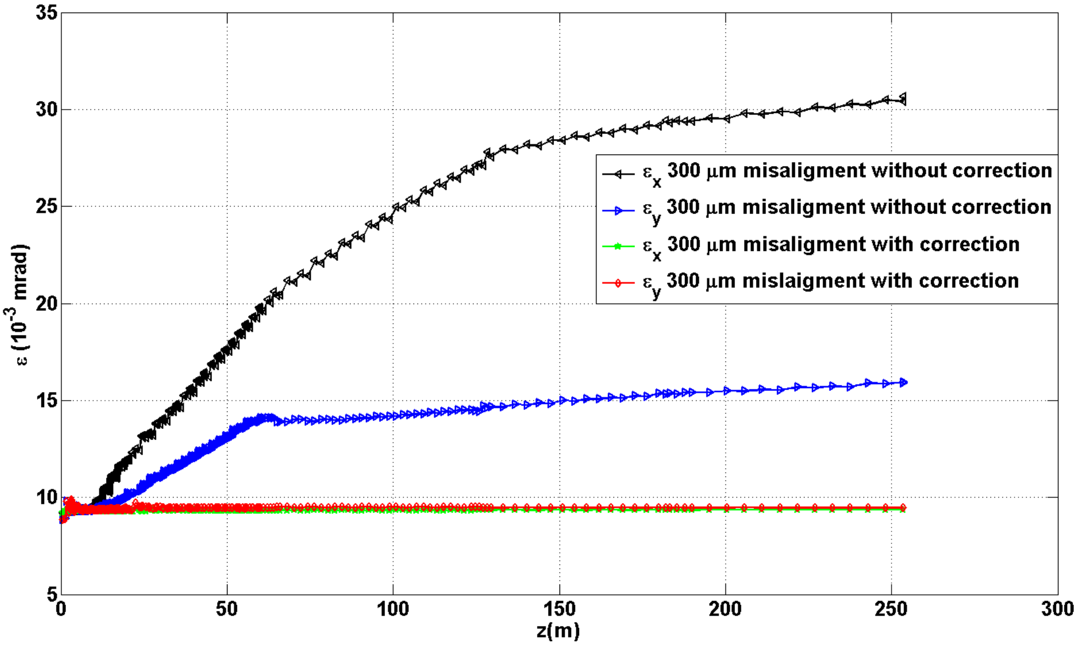

Figure 6.40 Horizontal and vertical emittance growth for positrons by a misalignment of 300 µm in each quadrupole and corrections.

To mitigate the emittance growth dipole (corrector) magnet with zero length is used after each quadrupole in the beam line. Placet can calculate the necessary kick of the corrector magnets and mitigate the emittance growths at x and y axis as seen in Fig.6.38, Fig.6.39 and Fig.6.40. As a result, the beam offset and quadrupole misalignment studies show that the resulting emittance growth can be mitigated by simple a one to one correction algorithm [33].

7. FURTHER POSSIBLE IMPROVEMENT

The updated schematic layout of the CLIC injector complex has been already described and presented considering the results of this studies in the previous chapters. In this chapter, it is focused on an alternative option of the schematic layout for the CLIC injector complex. In the injector complex, the booster linac accelerates the positron beam and the electron beam simultaneously from 2.86 GeV up to 9 GeV. The 5 GeV driver electron linac has been used to generate positrons on the target in the updated baseline of the injector complex. In the alternative scenario, the 5 GeV driver electron linac could be removed and to generate the positrons on the target the booster linac has been proposed as seen in Fig.7.1. Because, the booster linac has an energy gain of around 6 GeV and it could be used together with the main electron and positron beams by a time difference. Removing the 5 GeV driver electron linac would provide a significant cost saving. But in the alternative option, three bunch trains should be considered in the booster linac and in the rf system would need to be upgraded to accommodate longer rf pulses and higher beam loading. In addition, the beam loading compensation for all three beam will be very challenging. Further studies would be needed to seriously consider this option.

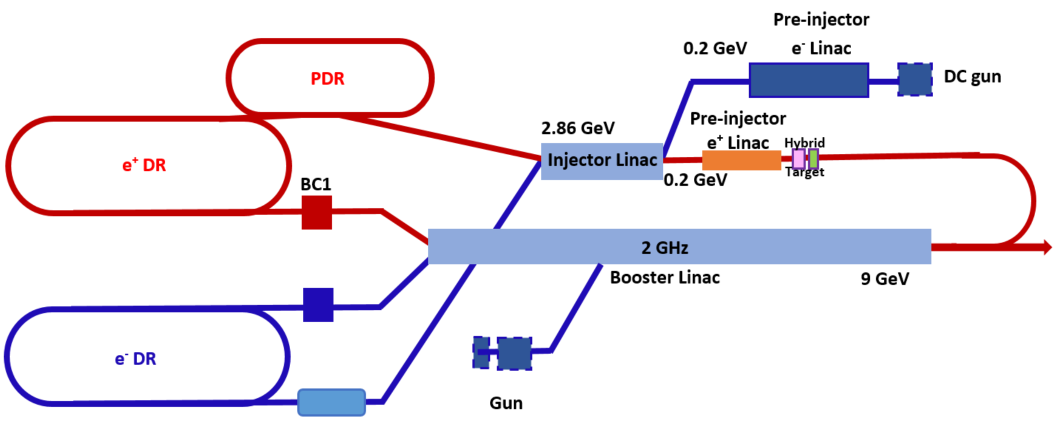

Figure 7.1 Schematic layout of alternative injector complex for CLIC

In the further possible improvement, another issue is the energy of the electrons that impinge on the target. In the CLIC CDR, positrons were generated by impinging a 5 GeV electron beam and the hybrid target was optimized for the positron yield at the exit of the target. In this thesis, the new optimization results show that there are some possibilities to increase the positron yield within the acceptance window of the pre-damping ring as mentioned in the previous chapters. As a result, we have increased the positron yield within the acceptance window by a factor of 2.5 compared to the CDR. This yield is sufficient to generate necessary beam current for positrons in the first stage of the CLIC at 380 GeV. The results show that two options can be considered to take advantage form the increased positron yield. The first is to use the electron driver linac with lower energy 3 GeV or 4 GeV to produce the positrons. The second is to decrease the charge in the electron driver linac at 5 GeV which allows as well to reduce to a single target station compared to the CDR. The electrons having lower energy could generate the positrons providing sufficient bunch charge. As a disadvantage, the lower energy positrons will have a larger divergence and a lower positron yield at the exit of the target. It remains to be studied which option provides higher cost savings in order to decide which way to go.

Another important issue for the design of the positron source is the beam loading problem for the pre-injector linac. The beam-loading lower the effective acceleration gradient, which depends on the beam current. In the high current beam especially for positrons, the effect of the beam-loading must be studied.

8. CONCLUSION

The accelerating and decelerating positron capturing modes have been studied for the CLIC positron source in detail. The decelerating mode has been optimized to capture more positrons at the exit of the pre-injector linac. The optimum gradient and phase have been determined for the first structure in the decelerating mode. This new optimization results in a factor 2.5 increase of the positron yield delivered into the acceptance of the pre-damping ring. This allows to reduce the beam current of the electron driver linac impinging onto the target accordingly, resulting in significant cost savings and a larger margin for the peak energy deposition into the target. In consequence a single target can be used as well for the first stage of CLIC at 380 GeV. In the original study for the CDR it was assumed two targets in parallel would be needed to insure the higher beam current at this stage. The effective yield after the pre-injector linac amounts to 0.98 e^+/e and after the injector linac we have 0.97 e^+/e within the acceptance of the pre-damping ring.

As a consequence of this thesis, the baseline of the CLIC injector complex has been updated for the first stage of CLIC at 380 GeV. It is shown that a bunch compressor is no longer required since the pre-injector linac has been well optimized. Also, it is seen that planned parallel hybrid target and pre-injector linac is not needed in the CLIC injector complex because the primary current onto the target could be reduced. In addition; decreasing the charge in the electron linac at 5 GeV will also provide significant cost saving in operating the electron driver linac in terms of installed rf power and overall power consumption.

Further improvements are still possible. During the simulations it became clear that increasing the aperture of the AMD and the accelerating structure would directly increase the yield as well increasing the strength of the solenoidal field around the pre-injector linac. However it remains to be seen if such changes are technically viable.

REFERENCES

[1] ATLAS Collaboration, Aad G. et al., Phys. Lett. B716, 1, 2012. DOI: http://dx.doi.org/10.1016/j.physletb.2012.08.020, date accessed: 05.20.2017.

[2] CMS Collaboration, S. Chatrchyan et al., Phys. Lett. B716, 30, 2012. DOI: http://dx.doi.org/10.1016/j.physletb.2012.08.021, date accessed: 05.20.2017.

[3] CERN, http://home.cern/about, date accessed: 05.20.2017.

[4] SLAC Linear Collider (SLC), http://www-sldnt.slac.stanford.edu/alr/slc.htm, date accessed: 05.20.2017.

[5] CLIC CDR, "A Multi-TeV Linear Collider base on CLIC Technology: CLIC Conceptual Design Report", edited by M. Aichler, P. Burrows, M. Draper, T. Garvey, P. Lebrun, K. Peach, N. Phinney, H. Schmickler, D. Schulte, N. Toge, CERN-2012 007, (CERN, Geneva, 2012), pp.99-107, 2012. http://clic-study.web.cern.ch/content/conceptual-design-report, date accessed: 05.20.2017.

[6] ILC Collaboration, the International Linear Collider – Technical Design Report, International Linear Collider, ILC-REPORT-2013-040, 2013. https://www.linearcollider.org/ILC/Publications/Technical-Design-Report, date accessed: 05.20.2017.

[7] CLIC Collaboration, 'Updated baseline for a staged compact linear collider, edited by P. N. Burrows, P. Lebrun, L. Linsen, D. Schulte, E. Sicking, S. Stapnes, M. A. Thomson, CERN-2016-004, CERN, Geneva, 2016. https://arxiv.org/abs/1608.07537, date accessed: 05.20.2017.

[8] CLIC Detector and Physics Collaboration, Abramowicz, H. et al., Higgs Physics at the CLIC Electron-Positron Linear Collider, CLICdp-Pub-2016-001, Geneva, Switzerland, arXiv:1608.07538 [hep-ex] , 2016. https://arxiv.org/abs/1608.07538, date accessed: 05.20.2017.

[9] Bayar, C., Ciftci, A. K., Doebert, S., and Latina, A., "Design and Optimization of the Positron Production Chain for CLIC from target to the Damping Ring", Nuclear Inst. and Methods in Physics Research, A. Reference: NIMA 59959, doi: http://dx.doi.org/10.1016/j.nima.2017.07.010, 7 July 2017.

[10] Bharadwaj V.K., Batygin Y. K., et al., 'Analysis of Beam-Induced Damage to the SLC Positron Production Target', Proc. PAC 2001, Chicago, IL, (WPAH019), June 2001.

[11] Rinolfi, L., Chehab, R., Dadoun, O., Kamitani, T., Strakhovenko, V. and Variola, A., 'Brilliant positron sources for CLIC and other collider projects', Nuclear Instruments and Methods in Physics Research B 309, 50–55, 2013.

[12] Dadoun, O., Chaikovska, I., Chehab, R., Poirier, F., Rinolfi, L., Strakhovenko, V., Variola, A. and Vivola, A., 'Study of a hybrid positron source using channelling for CLIC', CLIC-Note-808, CERN, 2009.

[13] Dadoun, O., Chaikovska, I., Leqercq, P., Poirier, F., Variola, A., 'The Baseline Positron Production and Capture Scheme for CLIC', Proceedings of IPAC'10, Kyoto, Japan, 2010.

[14] Vivoli A., Chaikovska, I., Chehab, R., Dadoun, O., Lepercq, P., Poirier, F., Rinolfi, L., Strakhovenko, V., Variola, A., "The CLIC Positron Capture and Acceleration in the Injector Linac", CLIC-Note-819, CERN, Geneva, 2010.

[15] Poirier, F., Rinolfi, L., Vivoli, A., Dadoun O., Lepercq P., Variola, A., "Dynamics on the Positron Capture and Accelerating Section of CLIC", CLIC-Note-877, CERN, Geneva, 2011.

[16] Aune, B. and R. Miller, H., "New Method for Positron Production at SLAC", SLAC -PUB 2393, Stanford University, Stanford, California 94305, 1979.

[17] ASTRA, A Space Charge Tracking Algorithm, http://www.desy.de/~mpyflo/, date accessed: 20.05.2017.

[18] Young, L. M. and Billen, J., the Particle Tracking Code PARMELA. Particle Accelerator Conference (PAC 03), Portland, Oregon, 12-16 May 2003.

[19] Young, L. "PARMELA Reference Manual", LA-UR-96-1835, Los Alamos national Laboratory, 2005.

[20] CAS (CERN Accelerator School). Fifth General Accelerator Physics Course, University of Jyvaskyla, Finland, CERN 94-01, 26 January 1994 Vol. I, Proceedings editor: S. Turner, CERN 1994. https://cds.cern.ch/record/235242?ln=en. Date accessed: 05.13.2018.

[21] Bayar, C., Doebert, S., Ciftci, A. K., "Beam Dynamics Simulation and Optimization of the CLIC Positron Source and Capture Linac", AIP Conference Proceedings 1722, 070001; doi: 10.1063/1.4944155, 2016.

[22] Doebert, S., discussion, CERN office: 18/2-008, Geneva, 2017.

[23] Billen, J. and Young L., Poisson Superfish User's Guide, LA-UR-96-1834 Revised January 13, Los Alamos, 2006.

[24] CST, https://www.cst.com/products/cstmws, date accessed: 05.20.2017.

[25] Poirier, F. “Positron Capture Section Studies for CLIC”, Presentation of POSIPOL2011, IHEP, Beijing, China, 2011.

[26] Ferrari, A., Rinolfi, L., Tecker F., Design Study of the CLIC Main Beam Injector Linac, CLIC Note-626, CERN, Geneva, 2005.

[27] Ferrari, A., Rinolfi, L., Tecker F., Particle Tracking in the CLIC Main Beam Injector Linac,CLIC-Note-665, CERN, Geneva, 2006.

[28] Ferrari, A., Latina, A. and Rinolfi, L., ‘Injector and Booster Linacs with the 2007 Beam Parameters’, CLIC-Note-737, CERN, Geneva, 2008.

[29] MAD-X, http://madx.web.cern.ch, date accessed: 05.20.2017.

[30] Wiedemann, H., “Particle Accelerator Physics”, Third Edition, Springer, chapter 7, USA, 2007.

[31] PLACET, Program for Linear Accelerator Correction and Efficiency Tests, https://clicsw.web.cern.ch/clicsw/, date accessed: 05.20.2017.

[32] Schulte, D., ‘PLACET: a program to simulate the drive beams’, Proceedings of EPAC 2000, Vienna, Austria, 2000.

[33] Bayar, C., Doebert, S., Latina, A. and Ciftci, A. K. 2018. ‘Tracking Simulations and Optimization of the CLIC Injector Linac’, AIP Conference Proceedings 1935, 070004; doi: 10.1063/1.5025985, 2018.

APPENDIX

Appendix 1: The Definition of the Beam Parameters in PARMELA

Appendix 2: Generation of AMD Field in PARMELA

Appendix 3: Superfish Input File for the CLIC Pre-Injector Linac

Appendix 4: Design of RF Accelerating Structure in Superfish

Appendix 5: Transformation of the Field Map from CST to Superfish Format

Appendix 6: Transverse Beam Dynamics in Linear Accelerator

Appendix 7: MAD-X Input File for the CLIC Injector Linac

Appendix 8: PLACET Particle Tracking Code

Appendix 1: Definition of the Beam Parameters in PARMELA

Phase And Radial Motion in Electron Linear Accelerators called PARMELA is an electron-linac particle-dynamic code [18, 19]. PARMELA has been written a multi-particle code originally for electron linacs in order to make the beam dynamics calculation but it can be also used for other particles like positrons and ions etc. in linac and/or transport systems [18]. PARMELA is used in the tracking simulations of the CLIC pre-injector linac and AMD for positrons.

Provided positron distribution at the exit of the target consists of $x, y, P_x, P_y,\ P_z$. This parameters are converted into PARMELA format by equations in this section. To define accelerator and beam parameters, some cards are necessary in the PARMELA input file. The first line of the input file should be started with RUN card. This keyword uses to define some global parameters as frequency, initial position and energy of the reference particle. The format of the RUN line is:

RUN RunNumber, PrintFlag, f_0, Z_0, W_0, LinacType, mc^2

The rf frequency of the linac, f_0 (MHz), is presented in this line. Also, Z_0 (cm) defines the longitudinal position of the reference particle and it is zero in the first element of the linac. If the cathode is used in the first element of the linac, it should be calculated and used a negative distance for special conditions. The initial energy, W_0 (MeV), is the kinetic energy of the reference particle. On the RUN line W_0 is defined as the average energy of the particles in the initial distribution. The mean energy of the particles, calculated by the initial particle distribution, can be used for it when using the beam distribution externally read in a text file. The ‘linacType’ is used to specify the type of linac cavities. Its default value is zero and if Fourier coefficients is used on the CELL line which is another card to define accelerator structures, its value is not important. The default mass, mc^2, is 0.5110034 MeV for electrons and positrons [19].

In the definition of the beam, PARMELA provides the many different beam distribution in the various types of input cards. The input 40 type is used in order to be read externally as a text file including the initial positron distribution for the CLIC pre-injector linac. The format of the INPUT 40 line is:

INPUT 40, NumberOfLines

Where ‘NumberOfLines’ is the number of lines of particle coordinate in the initial beam distribution. Each line in the file should be contained $x, x', y, y', \Delta\phi, \Delta W$. The transverse coordinates x and y should be in cm. The divergence coordinates x' and y' are defined in miliradians by equation 1.

$$x' = \frac{P_x}{P} \; , y' = \frac{P_y}{P} \tag{1}$$

The total momentum P is defined by equation 2.

$$P = \sqrt{{P_x}^2 + {P_y}^2 + {P_z}^2} \tag{2}$$

Here P_x, P_y and P_z are the components of the momentum in x, y and z coordinates respectively. In the last two columns of the initial distribution, the phase $\Delta\phi$ in degrees and the energy ΔW in MeV are:

$$\Delta\phi = \phi_i - \phi_{ref} \; , \Delta W = W_i - W_{ref} \tag{3}$$

In the equation 3, the quantities ϕ_{ref} and W_{ref} are the phase and energy of the reference particle defined its position on the RUN line. The phase $\Delta\phi$ and the energy ΔW are determined with respect to the phase and energy of the reference particle. The phase and energy of each particle are defined by ϕ_i and W_i in the lines. The energy,W_i is calculated by equation 4 for each particle in index i on line.

$$W_i = \sqrt{(mc^2)^2 + {P_i}^2} \tag{4}$$

The first term of equation inside square root quantity comes from the rest energy (mass) of a positron and P_i is total momentum for each particle on line in equation 4. After preparing the initial beam distribution as a text file with the extension TXT, the name of the file should be added in the variable ‘Part_In_Dst’ inside the file specified by LANL.INI [19]. The kinetic energy of particles are calculated from momentum components using in the tracking simulation.

Appendix 2: Generation of AMD Field in PARMELA

The COIL line is used to generate solenoidal magnetic field. The format of the COIL line is:

COIL Z_C, R_C, I_C, Z_{min}, Z_{max}

In the COIL line, the range of background field is determined by the lowest Z_{min} and highest Z_{max} coordinates. The special magnetic field can be supported by a series of COIL lines and the first COIL line must include values for Z_{min} and Z_{max} [19].

```
RUN 1 2 2000.1341 0 52.594
COIL    -2   5     845000 0 20
COIL    -1   5     -70000
COIL     0   5     -70000
COIL     1   5     -70000
COIL     2   5     -30000
COIL     3   5     -20000
COIL     4   5      35000
COIL     5  10      35000
COIL    10  15      35000
COIL    15  15      35000
COIL    20  15      25000
COIL    25  15      20000
DRIFT 20 2 1
CHARGE -1 1
ZOUT
OUTPUT 5
INPUT 40 46442
START 0 1 1500 0 10
END
```

Figure 1 PARMELA input file for the tracking simulation of AMD

For the tracking simulation of AMD, the necessary parameters are presented in Fig. 1. In the DRIFT line, the length of the drift and the radial aperture are defined by L and R_a respectively in cm. The format of the DRIFT line is:

DRIFT L, R_a, OutputFlag

The 'OutputFlag' key is used to extract output data at the end of the element. In the design, a radial aperture of 2 cm is chosen along the AMD to be compatible with the iris aperture of the RF structure in the linac.

As a following card in the input file, ‘CHARGE’ line identifies the charge and particle type. The format is:

CHARGE *Charge*, *ParticleType*

The charge line provides different particle type and ‘*Charge*’ specifies the particle charge. Its default values is settled as +1 for electrons, in the input file it is used to -1 and *ParticleType*=1 for positrons corresponding the rest-mass energy, 0.5110034 MeV, on RUN line.

In PARMELA input file, A ‘ZOUT’ line is used to print data for the magnetic field of AMD. In ZOUT line, some parameters should be added optionally to write rf field if accelerator structures are used. In the following line of PARMELA input file, the OUTPUT 5 line is used to display results of the calculation by ‘Pargraf’ via a file with extension .PGF. Also, the results are printed in two text files, TAPE.T2 and TAPE.T3, by using OUTPUT 1 instead of OUTPUT 5 in the input file.

The ‘START’ line is used to start the beam dynamics calculation. The format of the ‘START’ line is:

START Φ_0, $\Delta\Phi$, *NumberOfSteps*, *SpaceChargeSteps*, *OutputSteps*

Where Φ_0 is the initial phase for the calculation, $\Delta\Phi$ is the step size in degrees and ‘*NumberOfSteps*’ is the step number at time throughout the calculation. ‘*SpaceChargeSteps’* line activates the space charge calculation, if *SpaceChargeSteps*=0, the code does not count in the calculation. *OutputSteps* specifies output step generated by PARMELA.

Appendix 3: Superfish Input File for the CLIC Pre-Injector Linac

Superfish Input file: 2 GHz; 2pi/3 mode

```
==========================================================
RF cavity, 2GHz,
&reg kprob=1, dx=0.0400,
MAT=1
freq=2000.134100,icylin=1.0000,irtype=0,
xdri=0.0,ydri=2.0
kmethod=1,beta=1,zctr=4.9980&
&po x=0.0000,y=0.0000&
&po x=20.0,y=0.0000&
&po x=20.0,y=2.0000&
&po x=19.4,y=2.000&
&po x=19.4,y=4.15,nt=5,radius=1.106700&
&po x=19.4,y=4.9&
&po x=18.9,y=5.4132,nt=4,radius=0.5000&
&po x=16.1,y=5.4132&
&po x=15.6,y=4.9,nt=4,radius=0.5000&
&po x=15.6,y=4.15&
&po x=15.4136,y=2.0,nt=5,radius=1.10670&
&po x=15.0,y=2.000&
&po x=14.4,y=2.000&
&po x=14.4,y=4.15,nt=5,radius=1.1067000&
&po x=14.4,y=4.9&
&po x=13.9,y=5.4132,nt=4,radius=0.5000&
&po x=11.1,y=5.4132&
&po x=10.6,y=4.9,nt=4,radius=0.5000&
&po x=10.6,y=4.15&
&po x=10.4136,y=2.0,nt=5,radius=1.10670&
&po x=10.0,y=2.000&
&po x=9.4,y=2.000&
&po x=9.4,y=4.15,nt=5,radius=1.1067000&
&po x=9.4,y=4.9&
&po x=8.9,y=5.4132,nt=4,radius=0.5000&
&po x=6.1,y=5.4132&
&po x=5.6,y=4.9,nt=4,radius=0.5000&
&po x=5.6,y=4.15&
&po x=5.4136,y=2.0,nt=5,radius=1.10670&
&po x=5.0,y=2.000&
&po x=4.4,y=2.000&
&po x=4.4,y=4.15,nt=5,radius=1.1067000&
&po x=4.4,y=4.9&
&po x=3.9,y=5.4132,nt=4,radius=0.5000&
&po x=1.1,y=5.4132&
&po x=0.6,y=4.9,nt=4,radius=0.5000&
&po x=0.6,y=4.15&
&po x=0.4136,y=2.0,nt=5,radius=1.10670&
&po x=0.0000,y=2.000&
&po x=0.0000,y=0.0000&
```

Appendix 4: Design of RF Accelerating Structure in Superfish

In the design of RF structure, the first step is defined the geometry of the structure by Superfish. In the design of the RF structure, four cells cavity is chosen with a $2\pi/3$ mode, an iris aperture of 2 cm and a cell length of 5 cm at 2 GHz. To find the modes in the RF structure, the frequency scan should be done by Superfish.

For the frequency scan, two lines, $nsetp$ and $delfr$ should be added in the Superfish input file. The program uses the normalized quantity for the notation $D\ (k^2)$. Where D is the Dirichlet function, k is the wave number: k = ω/c= 2πf/c, f is the resonance frequency of the rf structure and c is the velocity of the light in a vacuum. There are two condition for the resonance of cavity, it emerges that $D\ (k^2)\ =\ 0$ and $dD(k^2)/d(k^2)\ =\ -1$. The mode frequencies of rf structure corresponding this conditions, can be seen in Fig. 1. The detail information for frequency scan can be found in directory LANL\Docs\SFPHYS5 (pg.613-614) after the installation of Superfish.

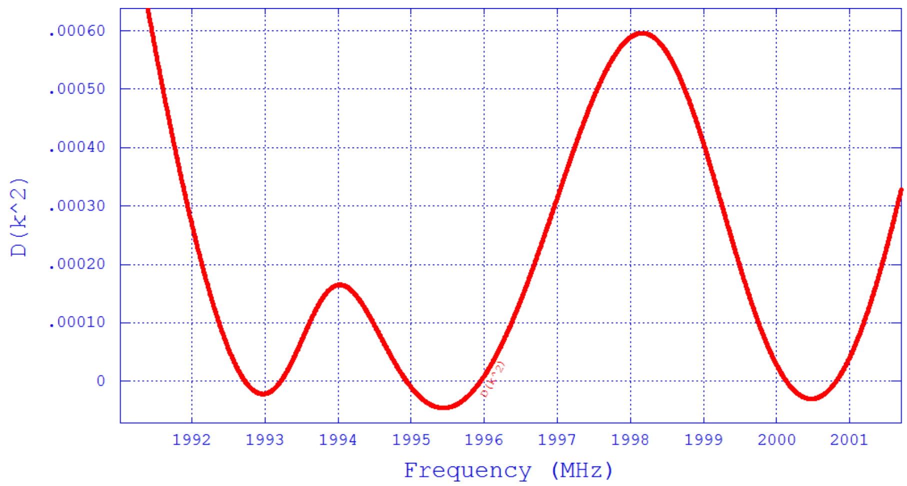

Figure 1 The frequency scan and modes of RF structure in Superfish

As seen in Fig. 1, in our design there are three different modes, 1992.7274 MHz, 1994.9369 MHz, 2000.1341 MHz, for the resonance frequency of the CLIC pre-injector linac.

After running the Superfish input file, it creates a binary solution file (.T35). The field map can be exported by using the SF7 Interpolator program. It creates a field map by the extension file name of T7 for PARMELA as seen in Fig. 2. Subsequently, the TW structures are created in PARMELA by the field map of the structure.

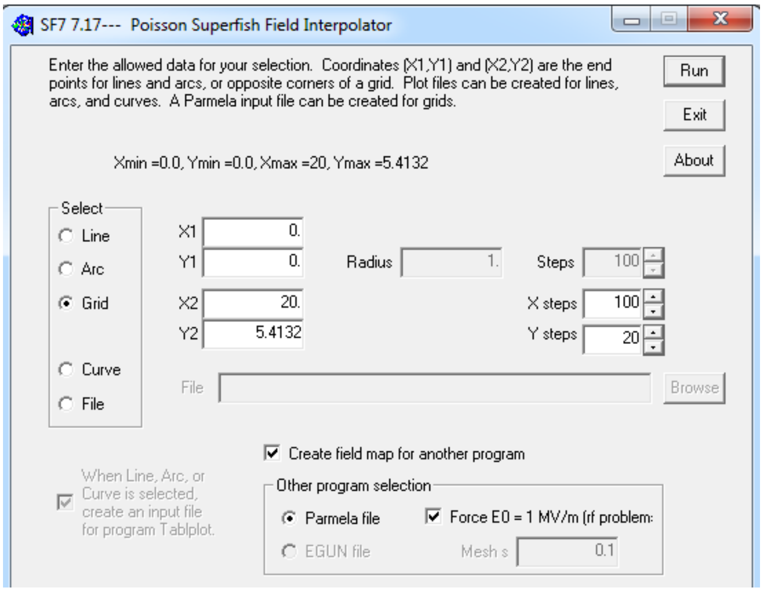

Figure 2 The layout of field interpolator in Superfish

Appendix 5: Transformation of the Field Map from CST to Superfish Format

First, the Superfish file format should be described with respect to field components for a better understanding. Superfish field file consists of 4 column $E_z, E_r, E, H_\emptyset$ for 2-D maps and here: E_z, E_r are the longitudinal and radial components of the electric field, E is the magnitude of the electric field and $H_\emptyset$ is the radial component of the magnetic field. The electric fields are in MV/m and the magnetic fields are in A/m. Superfish scans the radius of RF structure from its lowest to highest values in cylindrical coordinate. The initial value must be zero, $R_{min} = 0$, and the bore radius corresponds to the highest value, R_{max}. In the t7 file used by PARMELA, the number of the increments $\delta z = (Z_{max} - Z_{min})/N_z$ and $\delta r = (R_{max} - R_{min})/N_r$ must be same in both directions z and r. The structure of the Superfish field map is shown in table 1.

Table 1 The structure of the Superfish field map [19]

Line	Data	Description
1	Z_{min}, Z_{max}, N_z	Limits of z in cm and the number of z increments.
2	f	Resonant frequency in MHz from the Superfish solution.
3	R_{min}, R_{max}, N_r	Limits of r in cm and the number of r increments.
4	E_z, E_r, E, H_ϕ	Electric and magnetic fields at (z, r) = (Z_{min}, R_{min}).
5	E_z, E_r, E, H_ϕ	Electric and magnetic fields at (z, r) = ($Z_{min} + \delta z$, R_{min}).
6	E_z, E_r, E, H_ϕ	Electric and magnetic fields at (z, r) = ($Z_{min} + 2\delta z$, R_{min}).
:	:	:
$N_z + 4$	E_z, E_r, E, H_ϕ	Electric and magnetic fields at (z, r) = (Z_{max}, R_{min}).
$N_z + 5$	E_z, E_r, E, H_ϕ	Electric and magnetic fields at (z, r) = (Z_{min}, $R_{min} + \delta r$).
$N_z + 6$	E_z, E_r, E, H_ϕ	Electric and magnetic fields at (z, r) = ($Z_{min} + \delta z$, $R_{min} + \delta r$).
:	:	:
$(N_z + 1)(N_r + 1) + 2$	E_z, E_r, E, H_ϕ	Electric and magnetic fields at (z, r) = (Z_{max}, $R_{max} - \delta r$).
$(N_z + 1)(N_r + 1) + 3$	E_z, E_r, E, H_ϕ	Electric and magnetic fields at (z, r) = (Z_{max}, R_{max}).

CST field maps are typically ASCII (text) files with tables composed by 9 columns. Field maps consist of two files:

1) x y z real (E_x) real (E_y) real (E_z) image (E_x) image (E_y) image (E_z)

2) x y z real (H_x) real (H_y) real (H_z) image (H_x) image (H_y) image (H_z)

Where:

-X, Y and Z are the coordinates of the grid points, in meters (cm or mm etc.). -The components of the electric field E_x, E_y, E_z are expressed in Volt/m. -The components of the magnetic field H_x, H_y H_z are expressed in A/m.

The CST field map should be extracted in y-z or x-z planes in a rectangular face for the conversion because the Superfish file is in 2D cylindrical coordinate. For this conversion, a cute in the structure is applied in the sub-volume option of CST considering a constant x-value.

The format of the CST filed maps shows for y-z planes in table 2. In the geometry of structure (3D), the electric and magnetic fields are viewed in y-z plane at the sub-volume option and then the field maps are exported by CST. Two files include the real and imagine components of the electric and magnetic fields together axes x, y, z. The number of the increments is calculated from $\delta z = (z_{max} - z_{min})/N_z$ and $\delta r = (y_{max} - y_{min})/N_r$. The increment numbers must be same to convert the map from CST to Superfish t7 file.

In the field conversion, y axis is accepted as bore coordinate of structure and the field is scanned along z-axis in the structure. As the coordinate origin is optional, it is settled in the centre of the structure. CST field map is created in y-z planes all points 40×100 due to all points 20×100 in Superfish field map. The first step is to choose positive values at y-axes because R_{min} must be zero in Superfish field map. The second step is to change line orders at the y and z axis. While Superfish scans values at z-axis for a constant radius value in the cylindrical coordinate, CST scans values at y-axis for a constant value in z-axis. Therefore, the line orders are changed in the field map. The time axis is opposite in PARMELA compared to CST. However, the field structure of the 4 cell cavity behaves as a standing wave (SW) structure and there is not time dependency in the electric field. In other words, the imaginer components of the electric field are zero in SW structure. The field modelling of TW structure will be created in PARMELA input file by using field .T7 file. Therefore, just the magnetic field is reversely used in the conversion as seen in equation (4). The converted field components from CST to Superfish are:

$$E_z = Real(E_z)/10^6 \tag{1}$$

$$E_r = Real(E_y)/10^6 \tag{2}$$

$$E = \sqrt{Real(E_z)^2 + Real(E_y)^2}/10^6 \tag{3}$$

$$H_\emptyset = -\sqrt{Real(H_y)^2 + Image(H_y)^2} \tag{4}$$

In 2D field map of CST, the real component of the electric field at y-axis corresponds to the radius coordinate in Superfish. In the equations 1, 2 and 3, the units of electric fields has been changed from CST in V/m to Superfish in MV/m. (Real: the real component of field and Image: imaginer component of field).

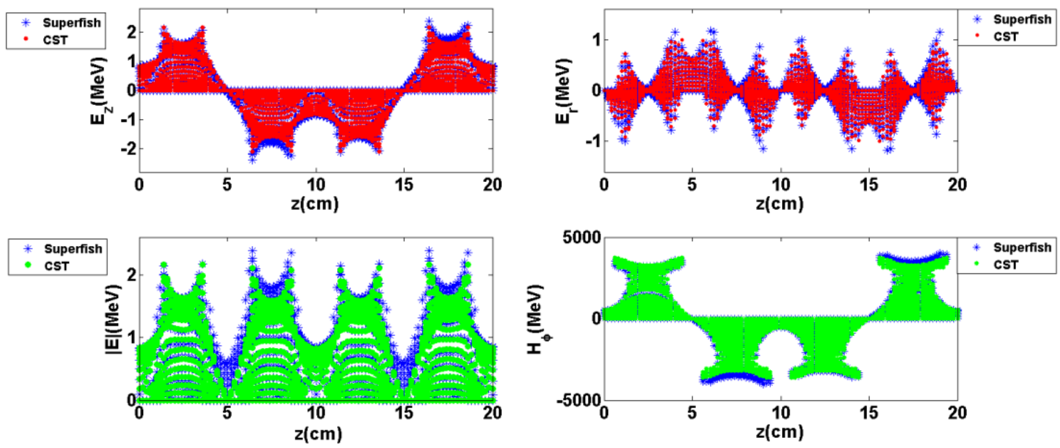

Figure 1 Illustrate of the field components for $2\pi/3$ mode rf cavity in CST and Superfish in the format of .T7 file

Where the upper left plot is for the longitudinal electric field, the upper right plot is for the radial component of the electric field, the bottom left plot is for the magnitude of the electric field and the bottom right plot is for the radial component of the magnetic field

Table 2 The structure of the CST field map in y-z planes all points 40×100.
R: real component and I: imaginer component

Line	The components of the fields	Axes (x= constant)
1	$R(E_x)$ $R(E_y)$ $R(E_z)$ $I(E_x)$ $I(E_y)$ $I(E_z)$ $R(H_x)$ $R(H_y)$ $R(H_z)$ $I(H_x)$ $I(H_y)$ $I(H_z)$	$(y, z) = (y = y_{min}, z = z_{min})$
2	$R(E_x)$ $R(E_y)$ $R(E_z)$ $I(E_x)$ $I(E_y)$ $I(E_z)$ $R(H_x)$ $R(H_y)$ $R(H_z)$ $I(H_x)$ $I(H_y)$ $I(H_z)$	$(y, z) = (y = y_{min} + \delta y, z = z_{min})$
:	:	:
N_y-1	$R(E_x)$ $R(E_y)$ $R(E_z)$ $I(E_x)$ $I(E_y)$ $I(E_z)$ $R(H_x)$ $R(H_y)$ $R(H_z)$ $I(H_x)$ $I(H_y)$ $I(H_z)$	$(y, z) = (y = y_{max}-\delta y , z = z_{min})$
N_y	$R(E_x)$ $R(E_y)$ $R(E_z)$ $I(E_x)$ $I(E_y)$ $I(E_z)$ $R(H_x)$ $R(H_y)$ $R(H_z)$ $I(H_x)$ $I(H_y)$ $I(H_z)$	$(y, z) = (y = y_{max} , z = z_{min})$
N_y+ 1	$R(E_x)$ $R(E_y)$ $R(E_z)$ $I(E_x)$ $I(E_y)$ $I(E_z)$ $R(H_x)$ $R(H_y)$ $R(H_z)$ $I(H_x)$ $I(H_y)$ $I(H_z)$	$(y, z) = (y = y_{min}, z = z_{min}+\delta z)$
:	:	:
$2N_y$	$R(E_x)$ $R(E_y)$ $R(E_z)$ $I(E_x)$ $I(E_y)$ $I(E_z)$ $R(H_x)$ $R(H_y)$ $R(H_z)$ $I(H_x)$ $I(H_y)$ $I(H_z)$	$(y, z) = (y = y_{max} , z = z_{min}+\delta z)$
:	:	:
$N_y (N_z -1)+1$	$R(E_x)$ $R(E_y)$ $R(E_z)$ $I(E_x)$ $I(E_y)$ $I(E_z)$ $R(H_x)$ $R(H_y)$ $R(H_z)$ $I(H_x)$ $I(H_y)$ $I(H_z)$	$(y, z) = (y = y_{min}, z = z_{max})$
:	:	:
N_zN_y	$R(E_x)$ $R(E_y)$ $R(E_z)$ $I(E_x)$ $I(E_y)$ $I(E_z)$ $R(H_x)$ $R(H_y)$ $R(H_z)$ $I(H_x)$ $I(H_y)$ $I(H_z)$	$(y, z) = (y = y_{max} , z = z_{max})$

The converted field map consisting of 4 column E_z, E_r, E, H_ϕ is compatible with Superfish file as seen in Fig. 1. There are two methods to create the electric field of TW structure in PARMELA. The first is to use two T7 files including sinus and co-sinus solutions and the second is to generate the Fourier coefficients by Superfish field map. In the simulation of the CLIC pre-injector linac, the second method is used to create a field map of TW consisting of 30 cells with a length of 1.5 meters.

Appendix 6: Transverse Beam Dynamics in Linear Accelerator

1. Definition of Beam Parameters

The beam is defined generally by 6 coordinates $x, y, z, x', y' and\ E\ (energy)$. The rms beam size is defined for the transverse coordinates by equations 1-2:

$$\sigma_{x(rms)} = \sqrt{\frac{1}{N}\sum_i^N (x_i - < x >)^2} \quad (1)$$

$$\sigma_{y(rms)} = \sqrt{\frac{1}{N}\sum_i^N (y_i - < y >)^2} \quad (2)$$

The rms momentum spread is defined by equations 3-4:

$$x'_{rms} = \sqrt{\frac{1}{N}\sum_i^N (x'_i - < x' >)^2} \quad (3)$$

$$y'_{rms} = \sqrt{\frac{1}{N}\sum_i^N (y'_i - < y' >)^2} \quad (4)$$

The rms emittance can be calculated for positrons by equations 5-6:

$$\varepsilon_{x(rms)} = \sqrt{< x^2 >< (x')^2 > - < xx' >^2} \quad (5)$$

$$\varepsilon_{y(rms)} = \sqrt{< y^2 >< (y')^2 > - < yy' >^2} \quad (6)$$

In the entrance of the injector linac Twiss parameters $\beta, and\ \alpha$ are calculated for positrons by equations 7-10.

$$\beta_x = \frac{\sigma^2_{x(rms)}}{\varepsilon_{x(rms)}} \quad (7)$$

$$\beta_y = \frac{\sigma^2_{y(rms)}}{\varepsilon_{y(rms)}} \quad (8)$$

$$\alpha_x = \frac{-(xx\prime)_{rms}}{\varepsilon_{x(rms)}} \quad (9)$$

$$\alpha_y = \frac{-(yy\prime)_{rms}}{\varepsilon_{y(rms)}} \quad (10)$$

2. Quadrupole and Drift

The quadrupole are used to apply the focusing or defocusing effect to the beam in the accelerators. The behavior of the particles are determined by the transfer matrix of the elements. The transfer matrix for the full quadrupole is given by the equations 11 in the focusing plane ($K > 0$).

$$M_{foc} = \begin{pmatrix} cos\varphi & \frac{1}{\sqrt{|K|}} sin\varphi \\ -\sqrt{|K|} sin\varphi & cos\varphi \end{pmatrix} \quad (11)$$

Similarly, in the defocusing place with $K = -|K|$ the transfer matrix can be determined by the equation 12.

$$M_{defoc} = \begin{pmatrix} cosh\varphi & \frac{1}{\sqrt{|K|}} sinh\varphi \\ \sqrt{|K|} sinh\varphi & cosh\varphi \end{pmatrix} \quad (12)$$

Where, K is the quadrupole strength, $\varphi = \sqrt{|K|}l$ for a full quadrupole and l is the length of the quadrupole [20, 30].

The drift space is used between the magnetic elements. The transfer matrix of the drift space is defined by equation 13.

$$M_{Drift} = \begin{pmatrix} 1 & s \\ 0 & 1 \end{pmatrix} \quad (13)$$

In the drift space, there is not any focusing effect because of $K = 0$. Here the drift length is shown as s.

3. FODO Cell

A FODO cell consists of a focusing (F), a defocusing (D) quadrupoles and drift spaces (0) in between. Figure 1 shows a schematic layout of a FODO cell.

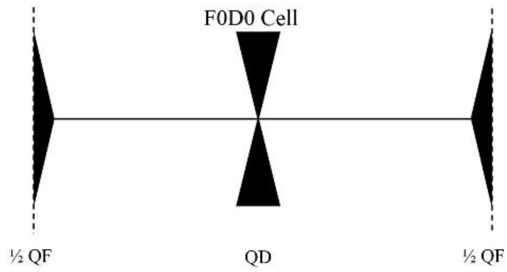

Figure 1 Schematic layout of a FODO cell

The FODO cell is used to create a periodic function. The transfer matrix is through a FODO cell:

$$M_{F0D0} = \begin{pmatrix} M_{11} & M_{12} \\ M_{21} & M_{22} \end{pmatrix} = M_{\frac{1}{2}QF}.M_{Drift}.M_{QD}.M_{Drift}.M_{\frac{1}{2}QF} \quad (14)$$

The phase advance of a FODO cell, μ can be calculated by the equation 15.

$$\cos\mu = \frac{1}{2} trace(M_{F0D0}) \quad (15)$$

The trace of the transfer matrix, M, is the sum of M_{11} and M_{22} elements of the matrix. The maximum value of betatron function in a FODO cell is given in equation 16 [30].

$$\beta_{max} = M_{12}\sin\mu \quad (16)$$

To calculate the minimum value of the betatron function in a FODO cell, the transfer matrices of the quadrupoles should be relocated in opposite ways.

Appendix 7: MAD-X input file for the CLIC injector linac

```
TITLE, 'Injector Linac';
BEAM, PARTICLE=POSITRON, ENERGY=0.20;
//zero matching section
D01: drift, l=0.2;
QF01: quadrupole, l = 0.4, K1 = 3.61809;
D02: drift, l=0.2;
QD01: quadrupole, l = 0.4, K1 =  -5.80276;
D03: drift, l=0.2;
QF02: quadrupole, l = 0.4, K1 = 6.84839;
D04: drift, l=0.2;
QD02: quadrupole, l = 0.4, K1 =  -4.59264;
D05: drift, l=0.2;
//First FODO section//
QF1: quadrupole, l = 0.4, K1 = 9.0;
D1: drift, l=0.15;
QD1: quadrupole, l = 0.4, K1 = -9.0;
//First matching section//
D11: drift, l=0.230;
QD11: quadrupole, l = 0.4, K1 = -6.47212;
D21: drift, l=0.2;
QF21: quadrupole, l = 0.4, K1 = 7.77028;
D31: drift, l=0.201;
QD21: quadrupole, l = 0.4, K1 = -4.79972;
D41: drift, l=0.837;
//Second FODO section//
QF2: quadrupole, l = 0.4, K1 = 3.95;
D2: drift, l=0.64;
QD2: quadrupole, l = 0.4, K1 = -3.95;
//Second matching section//
D12: drift, l=0.60;
QD12: quadrupole, l = 0.4, K1 = -4.99801;
D22: drift, l=0.60;
QF22: quadrupole, l = 0.4, K1 = 3.66190;
D32: drift, l=0.60;
QD22: quadrupole, l = 0.4, K1 = -3.43385;
D42: drift, l=0.60;
QF32: quadrupole, l = 0.4, K1 = 0.194488;
D52: drift, l=0.60;
//Third FODO section//
QF3: quadrupole, l = 0.4, K1 = 1.85;
D3: drift, l=1.65;
QD3: quadrupole, l = 0.4, K1 = -1.85;
//third matching section//
D13: drift, l=0.8;
QF23: quadrupole, l = 0.4, K1 = 1.05698;
```

```
D23: drift, l=0.8;
QD13: quadrupole, l = 0.4, K1 = -2.34772;
D33: drift, l=0.8;
QF33: quadrupole, l = 0.4, K1 = 2.07763;
D43: drift, l=0.8;
QF43: quadrupole, l = 0.4, K1 = -0.903131;
D53: drift, l=0.8;
//fourth FODO section//
QF4: quadrupole, l = 0.4, K1 = 1.02;
D4: drift, l=3.2;
QD4: quadrupole, l = 0.4, K1 = -1.02;
//fourth matching section//
D14: drift, l=1.8;
QF24: quadrupole, l = 0.4, K1 = -0.71961;
D24: drift, l=0.8;
QD14: quadrupole, l = 0.4, K1 = 0.710954;
D34: drift, l=1.8;
QF34: quadrupole, l = 0.4, K1 = -0.941809;
D44: drift, l=1.8;
QF44: quadrupole, l = 0.4, K1 = 0.204561;
D54: drift, l=1.8;
//five FODO section//
QF5: quadrupole, l = 0.4, K1 = 0.68;
D5: drift, l=4.9;
QD5: quadrupole, l = 0.4, K1 = -0.68;
//LINE//
MATCHINGZERO: LINE=(D01,QF01,D02,QD01,D03,QF02,D04,QD02,D05);
FODO1: LINE=16*(D1, QD1, D1, QF1);
MATCHING1: LINE=( D11, QD11, D21, QF21,D31,QD21,D41);
FODO2: LINE=18*( D2, QD2, D2, QF2);
MATCHING2: LINE=( D12, QD12, D22, QF22,D32,QD22,D42,QF32, D52);
FODO3: LINE=14*( D3, QD3, D3, QF3);
MATCHING3: LINE=( D13, QF23, D23, QD13, D33, QF33, D43, QF43, D53);
FODO4: LINE=7*(D4, QD4, D4, QF4);
MATCHING4: LINE=( D14, QF24, D24, QD14, D34, QF34, D44, QF44, D54);
FODO5: LINE=6*( D5, QD5, D5, QF5);
FODO: LINE=(MATCHINGZERO,QF1,
FODO1,MATCHING1,QF2,FODO2,MATCHING2,QF3,FODO3,MATCHING3,QF4, FODO4,MATCHING4,QF5,FODO5);
USE, PERIOD=FODO,RANGE=#S/#E;
TWISS, SAVE,BETX=2.6090, BETY=2.6457,ALFX=-0.9030,ALFY=-0.9299;
PLOT, HAXIS=S,VAXIS1= BETX,BETY, COLOUR=100,interpolate=true;
TWISS, FILE='twiss.txt', SAVE, BETX=2.6090, BETY=2.6457,ALFX=-0.9030,ALFY=-0.9299;
stop;
```

Appendix 8: PLACET Particle Tracking Code

Definition of Beam Parameters and Elements in PLACET

The positron distribution coming from the exit of the pre-injector linac is used for the PLACET tracking simulation in the CLIC injector linac. The format of the output file in the PARMELA is in table 1.

Table 1 The format of the output file in the PARMELA [19]

Column	Parameter	Description
1	x	x coordinate in cm.
2	x′	x divergence coordinate in milli-radians.
3	y	y coordinate in cm.
4	y′	y divergence coordinate in milli-radians.
5	ϕ	Phase coordinate in degrees
6	W	Energy in MeV

PLACET needs the longitudinal coordinate at z axes for the beam format and the equation 1 shows a relation between phase and z-axis in PARMELA.

$$z = \frac{c \times \phi}{360 \times f} \tag{1}$$

The phase coordinate is described by ϕ in degree, c is the velocity of the light in a vacuum and f is the frequency of the linac. The longitudinal coordinate at z axes can be calculated for PLACET by this relation.

Application of the Thin Lens Approximation in PLACET

The definition of the quadrupoles around RF structures at the first and second sections of the CLIC injector linac is not foreseen in PLACET. Therefore, we have used the thin lens approximation to define the quadrupoles around accelerating structures.

In PLACET; the quadrupole strength, S is defined with equation 2.

$$S\left[\frac{GeV}{m}\right] = E[GeV] \times l_Q[m] \times k[m^{-2}] \qquad (2)$$

Where E is the initial energy at the entrance of the quadrupole, l_Q is the quadrupole length and k is strength parameter used in MAD-X for quadrupoles. In the beginning, the quadrupoles have been divided 40 slices to use together with accelerating structures as seen Fig. 1.

```
Quadrupole -length 0.0  -name Q1_1   -strength    -0.018852
Cavity -length 0.01 -gradient 0.015 -phase 0
Quadrupole -length 0.0  -name Q1_2   -strength    -0.018852
.
.
.
Quadrupole -length 0.0  -name Q1_38   -strength    -0.018852
Cavity -length 0.01 -gradient 0.015 -phase 0
Quadrupole -length 0.0  -name Q1_39   -strength    -0.018852
Cavity -length 0.01 -gradient 0.015 -phase 0
Quadrupole -length 0.0  -name Q1_40   -strength    -0.018852
```

Figure 1 The definition of a quadrupole around RF structures

As seen Fig. 1, a quadrupole with zero-length slices is used with thick RF structures, 1 cm long.

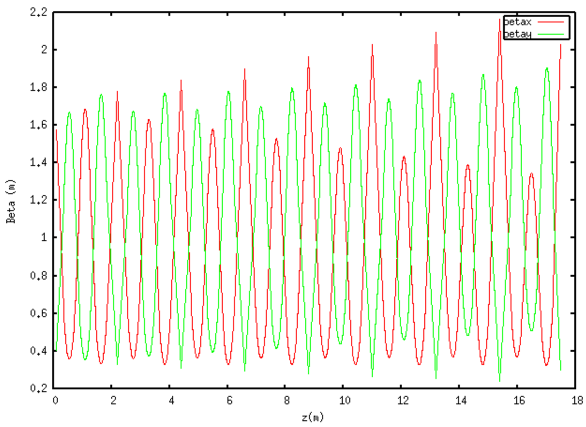

Figure 2 The betatron functions for the quadrupoles consist of 40 slices in the first section

Using thick RF structure, 1 cm long, gives a deformation in the betatron function as seen in Fig. 2. In the thin length approximation, the focal length should be much bigger than quadrupole length ($f \gg l_Q$). A quadrupole with a length of 0.4 m is used and the focal length is 0.27 m. As a result, we have used the following approach: A quadrupole with a length of 0.4 m has been split in 400 zero-length slices (in thin-lens) approximation with thick RF structures, 1mm long, between two consecutive quadrupole kicks to impart the appropriate acceleration (see Fig. 3).

```
Quadrupole -length 0.0  -name Q1_1   -strength    -0.0018852
Cavity -length 0.001 -gradient 0.015 -phase 0
Quadrupole -length 0.0  -name Q1_2   -strength    -0.0018852
Cavity -length 0.001 -gradient 0.015 -phase 0
.
.
.
Quadrupole -length 0.0  -name Q1_398   -strength    -0.0018852
Cavity -length 0.001 -gradient 0.015 -phase 0
Quadrupole -length 0.0  -name Q1_399   -strength    -0.0018852
Cavity -length 0.001 -gradient 0.015 -phase 0
Quadrupole -length 0.0  -name Q1_400   -strength    -0.0018852
```

Figure 3 The definition of a quadrupole around RF structures in the thin lens approximation

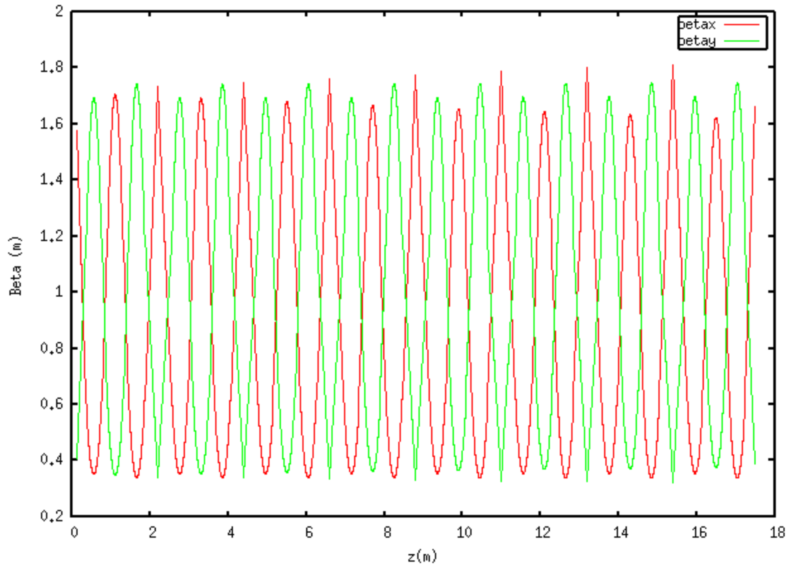

Figure 4: The betatron functions in the first section of the injector linac by using thin lens approximation

As seen in Fig. 4, the betatron functions provides expectedly periodicity along the first section. It is shown that the approach in thin-lens is working very well.

THESIS APPROVAL

The thesis study titled **"Design and Optimization of the CLIC Positron Source from the Target to Damping Ring"** written by Cafer BAYAR has been accepted as a **DOCTORAL THESIS** in the Physics Department of the Ankara University, Institute of Science and Technology on 26/04/2018 by the following jury.

Supervisor : Prof. Dr. Abbas Kenan ÇİFTÇİ
Izmir University of Economics Department of Physics

Co-Supervisor: Dr. Steffen DOEBERT
CERN (The European Organization for Nuclear Research)
BE-RF-MK

Members of the Jury:

Chairman of the jury: Prof. Dr. Saleh SULTANSOY
TOBB University of Economics and Technology Department of Material Science and Nanotechnology

Member : Prof. Dr. Abbas Kenan ÇİFTÇİ
Izmir University of Economics Department of Physics

Member : Prof. Dr. Orhan ÇAKIR
Ankara University Department of Physics

Member : Assoc. Prof. Dr. Metin YILMAZ
Gazi University Department of Physics

Member : Dr. Aysuhan OZANSOY
Ankara University Department of Physics

I approve the result stated above.